# DESIGN AND CONTROL OF A PNEUMATICALLY DRIVEN MRI-COMPATIBLE TELE-OPERATED HAPTIC INTERFACE

A Thesis
Presented to
The Academic Faculty

by

Melih Turkseven

In Partial Fulfillment
of the Requirements for the Degree
Doctor of Philosophy in the
School of Mechanical Engineering

Georgia Institute of Technology
May 2016

# DESIGN AND CONTROL OF A PNEUMATICALLY DRIVEN MRI-COMPATIBLE TELE-OPERATED HAPTIC INTERFACE

Approved by:


Jun Ueda, Committee Chair
School of Mechanical Engineering
*Georgia Institute of Technology*

Jun Ueda, Advisor
School of Mechanical Engineering
*Georgia Institute of Technology*

Michael Leamy
School of Mechanical Engineering
*Georgia Institute of Technology*

Ayanna Howard
School of Electrical Engineering
*Georgia Institute of Technology*

Nader Sadegh
School of Mechanical Engineering
*Georgia Institute of Technology*

Fumin Zhang
School of Electrical Engineering
*Georgia Institute of Technology*



Date Approved: 19 February 2016

*To my beloved, Ezgi.*

# ACKNOWLEDGEMENTS

I am pleased to thank those who have helped to make this research possible.

To my advisor, Dr. Jun Ueda, thank you for inspiring me with your passion for research and for teaching. It has been one of the greatest privileges of my life to have been your student. Thank you for all the time and energy you spent teaching me and shaping me professionally.

My sincere thanks to my reading committee, Dr. Nader Sadegh, Dr. Michael Leamy, Dr. Ayanna Howard, and Dr. Fumin Zhang. I truly appreciate all the helpful suggestions you have given, both with regard to this research, and for my career in general.

This research could not have succeeded without the encouragement, suggestions, and tips from many Georgia Tech colleagues. In particular I would like to acknowledge my fellow colleagues at Bio-Robotics and Human Modeling Lab, Dr. Wayne Book and Dr. Peter Hesketh. Thank you for being excellent resources for me.

Many thanks to the dedicated Woodruff School staff for all you do. I am indebted to Louis Boulanger, John Graham, and the Invention Studio team for all their contributions to the experimental apparati described in this thesis.

Finally, I would like to extend my appreciation to the Center of Compact and Efficient Fluid Power (CCEFP). The determined support I received from the center and its culturally rich environment contributed to my professional career significantly.

# TABLE OF CONTENTS

# LIST OF TABLES

# LIST OF FIGURES

# SUMMARY

This thesis presents a pneumatically driven haptic interface for rehabilitation in MRI, and methods for understanding, modeling and control of tele-operated pneumatic actuators. Pneumatic actuators have excellent MRI-compatibility as opposed to conventional electro-mechanic systems. They are also desirable for their inherent compliance and easy-maintenance. However, the actuator and the system drivers cannot be co-located due to the MRI-compatibility requirements. The actuators are driven via long transmission lines, which affect the system dynamics significantly, and the use of commercial pressure sensors are prohibited in MRI rooms. This thesis addresses these challenges in the tele-operation of the pneumatic actuators and introduces novel approaches to mitigate the adverse effects of long transmission in pneumatic drive. An optical force sensor was designed and prototyped to enable force feedback from the actuator in the MR-scanner. Subsequent analysis on the sensing quality of the designed sensor improved its hysteresis characteristics. Based on the enabled force feedback, a non-linear observer that achieves asymptotical stability was designed. The developed observer was validated experimentally. Finally, a control algorithm that accounts for the pressure dynamics in the transmission lines was introduced. The performance of the controller and its contribution in the force control accuracy were tested on systems with various line lengths. The methods and tools developed in this research are expected to expand the range of applications of tele-operated pneumatic actuators, particularly on rehabilitation in MRI.

# CHAPTER I

# INTRODUCTION

## 1.1 Motivation

Functional magnetic resonance (fMRI) has become a flagship non-invasive method for monitoring brain activity with a high spatial resolution. Unlike other imaging techniques such as PET, EEG or CET; fMRI can be utilized for obtaining local brain activity with a good signal-to-noise ratio (SNR) [61]. The opportunities fMRI brings have recently been started to be exploited to rehabilitation and medical treatment. Such new application areas involve analyzing the effects of physical therapy on stroke patients. fMRI has been used in several studies to understand training-induced neuroplasticity on a damaged brain that suffered stroke, and the physical procedures that lead to recovery in the motor functions [9],[11].

Although fMRI is a promising tool for monitoring human brain, the use of fMRI limits the range of rehabilitation and research applications due to the tight space within MRI machines and the intense magnetic field in the MRI environment. The practitioner that applies the therapy needs to stand by each patient during the whole session being exposed to the magnetic environment. The rehabilitation of a stroke patient usually consists of repetitive sessions of several weeks, each session being hours long. Therefore, manual therapy in MRI is not practical for prolonged studies. Robotic systems have been introduced to automate the therapies, removing the performance variability on a manual operation and providing quantitative feedback on the patient for more objective evaluations [37]. However, conventional robots that involve electronic actuation and sensors interfere with the magnetic environment; hence, cannot function in MRI rooms. An MRI compatible robot that has a low

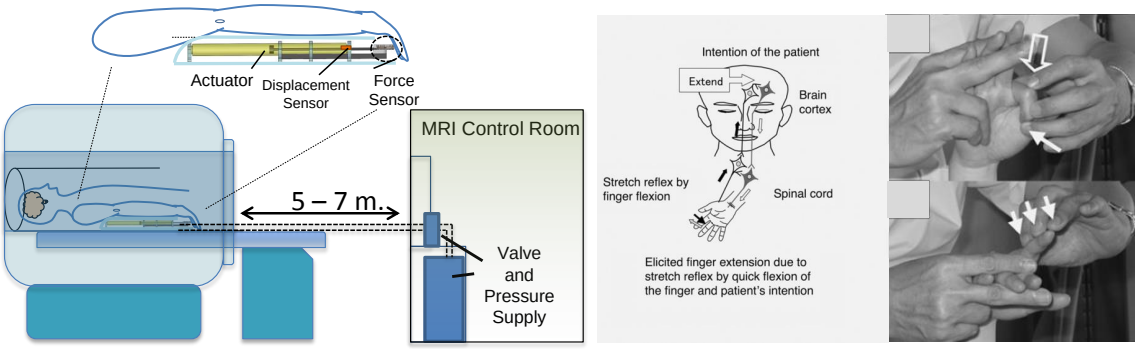


Figure 1: The concept of MRI-guided rehabilitation: schematics showing a typical setup (left), manual therapy on finger rehabilitation (right)

magnetic susceptibility should be designed for medical operations in MRI. Rehabilitation procedures involve physical interaction with the patient; therefore, the robot needs to provide a desired impedance that is set by the requirements of the therapy. The operation may require an agile response and a good range of motion comparable to that of a human.

Among MRI-safe actuation methods, pneumatic systems have usually been preferred for they can be designed for ultimate MRI compatibility. Pneumatic actuators do not involve electromagnetic signals that would distort MRI scans as in the case of other methods utilized in the literature such as piezoelectronics and ultrasonic motors. In addition, they present an inherent compliance that provides safety, and a relatively wider range of motion [92]. However, the actuators and servo valves cannot collocate since general valves use solenoids with ferromagnetic materials. As a result, long transmission lines between the actuators and the valves should be used. Pressure attenuation and time-delay introduced by those lines make it difficult to control the actuator by using conventional system models. Due to the same compatibility requirements, the use of conventional sensors for pressure and force feedback is restricted. Medical robots designed to be operated in Magnetic Resonance Imaging (MRI) rooms are restricted to be made of non-ferrous materials to prevent magnetic interference [79], [59].

Typically, tele-operated pneumatic robots are utilized for low-speed position control operations e.g. surgical tasks such as needle placement for biopsy [71],[8],[54]. Hydraulic systems are considered to be more effective in low-bandwidth applications. The pneumatic actuators present a slightly higher bandwidth, but their control is more challenging due to the compressibility of the air. A system that accounts for the effects of the transmission line could improve the bandwidth of the actuation and realize a physical therapy preserving a desired impedance.

## 1.2 Overview

This research aims to develop tools and methods that will enable the impedance control of a pneumatic system with long transmission lines. The designed system needs to be capable of force and position measurements to be used for both the control of the device and evaluating the performance of the patient [31],[32],[33]. Figure 1 presents the conceptual idea of how the system should operate. The force sensing will be accomplished by developing an MRI compatible optical force sensor. Position sensing is relatively easy as MRI compatible optical encoders are commercially available. The problem of obtaining pressure states in the actuator chambers was solved by designing an asymptotically-stable observer that uses force and position feedback. An advanced system model that accounts for the dynamics of the transmission lines were implemented to improve the bandwidth of the system.

This thesis established the pressure observer and the advanced system model and experimentally validated their contribution on characterizing the system more accurately. The proof of asymptotical stability in the pressure observation was obtained. In addition, an optical force sensor made of plastic was designed and its MRI compatibility was validated. The design of the sensor was analyzed for an improved precision and sensitivity, and the analysis was confirmed through experiments. The development of the pressure observer, the system model and the MRI-compatible force sensor

provided the key components to compensate for the lack of pressure sensors and the effects of the transmission lines on the pressure dynamics.

Based on the established tools and methods, a model-based controller was designed to accomplish force control on a tele-operated pneumatic system. The force control experiments were conducted on test setups that represent tele-operation. An MRI-compatible prototype will be developed to realize the control objectives in an MRI environment. Control experiments in an MRI room will demonstrate the usefulness of pneumatic systems for rehabilitation purposes. It is expected that this new system will lead to new, customized pneumatic robots that are designed for particular types of rehabilitation procedures. The results of this research could be useful in the design and control of various pneumatic tele-operation systems with applications to many areas of robotics, such as medical robots or transportation systems [51].

## 1.3 MRI Compatibility Criteria

The high magnetic field and RF pulses inside MRI room interfere with electrically driven sensors and robots. Either the robotic device is affected by the MRI machine or the device causes distortion in the output image of the MRI machine. Detailed explanations on the requirements for MRI-compatibility have been shown in various sources [[59],[79],[7]. The material of the device should be magnetically inert. A non-compatible device itself can be attracted by the MRI machine which may induce a dangerous action called missile effect. Also a magnetic piece distorts the output images since magnetic field inside the MRI machine loses its homogeneity. Non-conductive materials are advantageous about compatibility. Magnetic field can induce Eddy current on the conductive body of the device. That may heat the device which may become dangerous especially if that device is in contact with patients. The severity of the restrictions for MRI-compatibility depends on how close the device is to the area being imaged. In this paper, following definitions for different compatibility

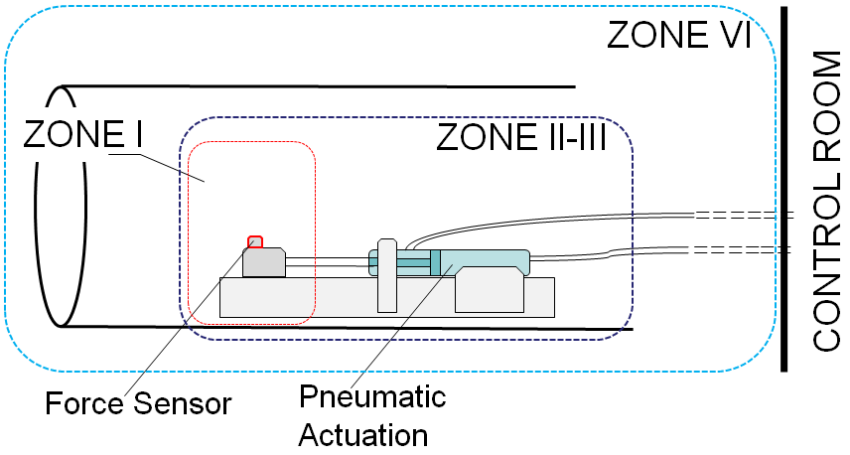


Figure 2: Schematic for the MRI-safety zones with respect to the robot's location

levels are accepted [7].

- **Zone 1** device: Operates in the area being imaged. Usually in contact with the patient, a device working in this region should be highly compatible to MRI environment.
- **Zone 2** device: Remains inside the MRI chamber but not in the area being imaged.
- **Zone 3** device: Remains inside the MRI chamber but not in use during imaging.
- **Zone 4** device: Can be used inside MRI room as long as it is kept a distance of more than 1 m to the magnet.

These zones are illustrated in Figure 2.

## 1.4 Pneumatically Driven Systems for Robotic Rehabilitation in MRI

In the last two decades, the popularity of pneumatically driven systems has grown in the field of robotics for their mechanical advantages. Pneumatic actuation has a higher power density compared to conventional electric-motors [53], and provides a

clean operation with low maintenance costs. Lately, the application areas of pneumatic actuation has expanded to tele-operation, in order to utilize some of its inherent practical advantages. For example, pneumatic cylinders have been a popular choice for magnetic-resonance-imaging (MRI) compatible robots [8], [89], [40], [93], as the air is inert to magnetic field. MRI-compatible systems with pneumatic actuation typically require long transmission lines (5-7 meters) to keep the magnetic system components away from the imaging area. Ability to distribute system components via transmission lines makes the pneumatic actuation desirable for humanoids as well [78]. Tele-operation via long tubes has also been practiced for transportation systems where a mobile robot is designed to operate in challenging environments, being powered from a distance [51].

Pneumatic actuation has been shown to be very effective in these tele-operation applications; however, the presence of long transmission lines limits the control of those devices. This research aims to propose key components and methods that would mitigate the adverse effects of long transmission lines on the pressure dynamics. The contributions of this work would impact the presence of pneumatically driven systems for robotic rehabilitation in MRI.

## 1.5 MRI Compatible Force Sensors

Resonance Imaging (MRI) is a widely used technique in diagnostics because of its ability to monitor human soft tissue 3-D in real time. MRI-compatible devices, including medical instruments [29] and robots [15, 68], are expected to extend the capability of MRI to provide advanced intervention and tele-surgery. MRI compatible force sensors, in particular, have an impact on MRI's versatility as they enable haptic force feedback to be used in experiments regarding the brain's motor function or provide surgeons with force feedback during tele-operated surgeries.

Several models of MRI-compatible force sensors are catalogued by Gassert et

al. [18]. Puangmali et al developed a 3-axis force sensor for minimally invasive surgeries [54]. Chapuis et al. developed a force/torque sensor [5], Khanicheh et al. designed a hand driven haptic interface which employs ERF fluids [36], Xuan Tan et al. introduced a triaxial force sensor using displacement amplification mechanisms citeTan2010. However, these design ideas are not meant for extension to 6-axis sensing applications. Tada et al. introduced different models for 2-3 axis sensing [76], [77] and developed a 6-axis force sensor [75] yet these designs impose many inputs to be handled and multiple cables for fewer number of axis force sensing. Also, significantly high hysteresis seems to be a common, inevitable problem for plastic MRI-compatible sensors.

# CHAPTER II

# LITERATURE SURVEY

This chapter summarizes the contributions from various communities that set the context for and provide principles relevant to the work conducted in subsequent chapters. Since the lack of direct pressure measurement in MRI rooms, part of the developed work is related to pressure estimation in pneumatic systems. This survey involves various sources on the pressure observation methods. A review on the control of teleoperated pneumatic systems is also prepared. In addition, representatives from the MRI-compatible sensor and displacement amplfiying compliant mechanisms areas are included.

## 2.1 Pressure Estimation in Pneumatic Systems

Conventional pneumatic system models unfortunately cannot fully characterize complex but practical issues such as compressible flow through transmission lines, heat transfer, frictional losses or leakage in the equipment. Although there are standard pneumatic system models that have been used for model-based pressure observers, new applications often require unconventional hardware that consequently reduces the accuracy of pressure estimation. One of the most influential factors is the presence of long transmission lines between the pressure source and the actuator, often found in pneumatically operated medical robots, including those that have been studied in the authors' laboratory [40], [81]. Pneumatic actuators and servo valves cannot collocate since general valves use solenoids with ferromagnetic materials. As a result, long transmission lines between the actuators and the servo valves should be used. A similar situation can be found in transportation systems [51]. Pressure attenuation and time-delay introduced by a long transmission line makes it difficult to

apply conventional models for pressure estimation and control. Relatively complex models have been proposed to characterize certain aspects of the line dynamics [85], [42], [56], [38], [13]. However, such methods may include extensive empirical parameters exclusive to the components being used, and they are not designed to capture all possible practical factors that affect the actuator pressures. For example, MRI compatible actuators involve glass cylinders with carbon pistons for MR safety. In addition to low magnetic susceptibility, glass cylinders can achieve low friction, yet the gas leakage through their ports are not negligible [2]. Furthermore, pneumatic actuators may involve extra caution for piston protection, e.g. cushioning, that introduce an unestimated resistance to the fluid flow at the cylinder connection ports [3], [16].

Techniques for observing pressure states have been discussed in the literature. Pandian et al. presented two observation methods in which one of the chamber pressures was treated as disturbance and measured; while the other one being estimated, assuming that the mass flow rates were exactly known [48]. Bigras and Khayati focused on an application where actuator connection ports introduced significant resistance on input flow [3]. They differentiated chamber pressures from the rest of the system and observed them through pressure measurements made on the transmission lines. Pressure observation via sole measurement of the motion of the actuator was discussed by Wu et al [87]. They concluded that pressure state variables were not locally weakly observable, leaving no conclusion on global observability. Gulati and Barth took advantage of the closed-loop nature of the standard system model and developed a globally stable, nonlinear pressure observer that does not require the dynamic model of a piston [24]. They also incorporated force feedback into their original observer for improved convergence [23]. The force feedback was introduced to compensate for certain dynamic terms in the pneumatic system dynamics, which in turn required a high precision in the calculation of actuator force. Driver and Shen

developed a pressure observer for a force-controlled pneumatic cylinder. They utilized force feedback and a hypothesized constant average pressure value to calculate estimated pressures. Their method relied on the accuracy of the valve model as well as their hypothesis [12]. Conventional model-based observers are proven to be effective only when simplified assumptions made for the system are met. Unfortunately, there is no existing pressure observer applicable to a system with unconventional hardware, especially long transmission lines that are considered in this paper.

## 2.2 Displacement Amplifying Compliant Mechanisms for Force Sensing

Due to the intense magnetic field in the MRI room conventional designs that involve metals or employ electricity reduce the quality of the MRI images. Several force sensors with limited MRI compatibility have been developed compromising the range of applications [20, 36, 80]. Optical force sensors with compliant, plastic structures have been proposed for ultimate MRI compatibility. In such sensors, an applied force results in a particular deformation on a compliant body and the deformation is sensed by an optical aperture. The compliant body of a sensor could be shaped so as to match the type of sensing task [19, 54, 5, 73, 72, 75]. To have desired deformation characteristics and meet various application-dependent requirements such as sensitivity and multi-directionality, the idea of displacement amplifying compliant mechanisms (DACM) has been applied to the optical force sensors [77]. Polymers are often the material of choice for the mechanism in such designs for higher MRI compatibility and flexibility. MRI compatibilities of various materials are compared and superiority of polymers have been demonstrated by MRI images in Schenck's work [59]. Flexibility is a measure of allowable elastic deformation on a material defined as the ratio of its yield strength to its elastic modulus by Howell [27]. Polymers have the highest flexibility compared to other materials such as metals and ceramics. However, the non-linear stress-strain relationship and a high possibility of inaccuracy due to

hysteresis are major problems with polymers that should be considered in designing a mechanism.

Several methods for improving plastic DACMs have been introduced in the last two decades [49, 50, 10, 58, 64, 91]. A great deal of work is based on what is called "topology optimization" in which an approximate topology of an efficient mechanism is obtained from a ground structure. The performance of a topology is defined by a custom function and an extremum of the function is calculated in consideration with several constraints defined by the designer.

Despite the fact that topology optimization methods are widely applied for amplification mechanism design, more specific analysis methods are available to incorporate size and shape optimization once the topology of the structure is determined [30, 45, 25, 43, 44, 88]. An analytical method based on the calculation of deflections by discretizing the body has been explained in Howell's book [27]. The body of the structure is modeled as a chain of beams and the deflection in each beam is predicted by utilizing Castigliano's theorem.

Most of the works related to DACM analysis are aimed to optimize the mechanisms of actuation. However, the primary desired qualities change when it comes to compliant bodies for sensing tasks. Sensitivity and precision of a deformable body become more important than the amplification of the mechanism. Ananthasuresh and Krishnan developed a general method for estimating the sensitivity of a given topology and compared several existing designs [39]. They introduced a variable which they called "unloaded output sensitivity" to define the sensing performance of a force sensor. Then they synthesized a new mechanism using that new variable as the target to be maximized in the size and shape optimization step.

Wang and Hu developed a force/weight sensor that employs a quartz-crystal resonator (QCR) for the transduction and a compliant body [84]. A measure of sensitivity is derived analytically in their work. They maximize an objective function which

is the ratio of sensitivity to measurement range.

## 2.3 Control of Pneumatic Actuators with Long Transmission Lines

Pneumatic transmission lines, especially if the line length is far bigger than its diameter, have a significant influence on the pressure dynamics of the system. Compressibility of the flowing media, air, introduces a pure time delay and an attenuation in the mass flow. Also, a pressure gradient emerges along the lines due to the tube friction. Resultantly, the dynamic difference between the pressures at the terminals of a long connecting tube either requires an additional pressure sensor at the end of the line, or an estimation method that can characterize the line dynamics. Given the complexity of compressible flow dynamics, modeling pneumatic lines has been neglected in the field of robotics for simplicity and faster computation. Very simplistic approaches have been adopted to address the additional dynamics brought by pneumatic tubes. A relatively standardized method is to characterize the line as a dead volume and simply combine it to the actuator [24]. This generic approach provides a stable model for non-linear controllers [82], yet it cannot reflect the pressure inhomogeneity through the lines. Relatively more advanced methods are required to achieve a good accuracy in both the actuator pressure estimation and the mass flow rate through the lines.

Studies on transmission line dynamics started with theories on mass transportation and a number of experimental investigations dating back to the 1930s. More extensive works that focused on transmission line modeling preceded through the rest of the 20th century, as summarized by Stecki and Davis [70]. The governing equations for air flow through a duct were derived by Schuder and Binder in 1956 [60]. A number of analytical solutions for limited cases with specific steady boundary conditions and numerical solutions for more general applications have been derived

since then [17],[65],[21],[86]. Detailed descriptions of most prominently applied numerical methods can be found in Beater's book [2]: Modal Approximation (frequency domain approach), Finite-element models (in time domain), modeling the line as a passive element, and modeling with lumped parameters (characterization of the line as a RLC circuit). Elmadbouly and Nour modeled the line and made a sensitivity analysis with respect to line dimensions [13].

The simplicity of standard modeling can be traded with very high accuracy by the use of finite-element like, numerical models. In general, the ultimate accuracy can be achieved by industrial simulation packages that involve heat transfer calculations and frequency-dependant friction in addition to fluid compressibility. However, such methodologies are computationally too expensive for real-time control applications [38]. Simpler methods based on averaging flow parameters within finite number of volume partitions were introduced for faster computation [2], [86], [85], [21]. Krichel and Sadowny adapted several hydraulic line modeling techniques to pneumatic systems, and suggested a time domain model to capture transient behavior of pressure and flow rate through the tubes [38]. They divided the line into iso-thermal, spatial segments and numerically solved the dynamic equations for each segment. Although these approaches are practical and accurate at the same time, they are not suitable for existing non-linear controllers for their high-order, multi-step calculation algorithms.

In addition to accuracy, the compatibility of a given model to widely applied, non-linear controllers is very crucial. Yang et al approximated the pressure dynamics of the tubes using a low order transfer function with empirically obtained parameters [90], yet they didn't consider the line dynamics on their controller design. Li et. al. discretized the line and obtained a time-domain model, adding heat transfer effects as well [42]. They demonstrated the use of their model with an open-loop position control, and compared its performance against a closed-loop control with valve pressure feedback. Apart from them, Hurmuzlu et al. obtained an explicit formula for

the mass flow rate at the end of the line and implemented it in a sliding mode based controller. The controller was shown to be effective for line lengths up to 2 meters [56], [55]. Besides the limited range of transmission line length compared to those in the aforementioned applications, their model required the knowledge of actuator pressures. That study illustrated the benefits of more accurate system modeling; yet, more comprehensive modeling methods were needed for systems with longer transmission lines.

# CHAPTER III

# ANALYSIS ON TRANSMISSION LINES

This chapter presents preliminary investigations on the compressible flow characteristics through long and slender tubes that are typically involved in MRI-compatible pneumatic systems. Thermodynamics of a compressible gas flow in a duct has been studied over half-a-century, and the governing relations of mass transfer to/from a closed volume has been described in various sources, as outlined in chapter II. In the robotic applications, however, those relations are simplified with certain assumptions on the properties of the flow that are heavily dependent on the application. The observations described in this chapter were made to form a basis for the assumptions followed in this study.

An important property of the flow that defines the pressure dynamics is the heat transfer along the lines. Steady-state flow experiments were set to analyze the accuracy of isothermal flow assumption, which has generally been associated with low frequency operations. Then, the validity of an analytical solution that has been developed for short-range transmission lines ($\leq 2m$) was examined. The experimental setup used for this study involved 7.25 m long transmission, which is typical for MRI related applications. Finally, samples of frequency response of a tele-operated actuator with 7.25 m long transmission were obtained. Apart from the transmission lines, those observations illustrated the role of structural factors; such as the inlets of the actuator and possible internal leak across the piston, on the pressure dynamics.

## 3.1 Temperature Along the Line

Temperature variations through the pipe is neglected in engineering articles for the sake of model simplicity [24]. A constant room temperature, $293^oK$, is generally

Table 1: Rotameter Readings on Steady Flow Tests

| Transmission Line Length (m) | Flowmeter reading at position A (ACFM) | Corrected flowrate at A (SCFM) | Flowmeter reading at position B (ACFM) | Corrected flowrate at B (SCFM) | Mismatch (%) |
|---|---|---|---|---|---|
| 8 | 1.763 | 3.377844678 | 3.385 | 3.626785714 | 6.8639577 |
| 6 | 2 | 3.738929237 | 3.675 | 4.014047599 | 6.8538889 |
| 3 | 2.9 | 4.994391412 | 4.375 | 5.064685742 | 1.3879307 |

assumed for the pneumatic applications. The validity of that assumption for the tele-operated system in our study was checked prior to any further calculations.

The significance of temperature variation through a pipe flow, were initially evaluated with rotameter measurements made at two distant locations on the pipes with different pipe-length. A schematics of the experimental setup is given in Figure3.a. Rotameters can only measure the volumetric flow rate in the nominal condition of the flowing media and the rotameter readings need to be converted with respect to a given reference state. The method of obtaining the real mass flow rate from the actual measurement is outlined in Appendix B. Those measurements are converted to standard-condition values assuming that there is no change in the temperature and the accuracy of the conversion was checked. The measurements, before and after the conversion, as well as the mismatch between two corresponding mass flowrate values are shown in Table 1. The value of the mismatch indicates whether the isothermal flow assumption is erroneous or not.

It should be noted that, the presented measurements include the uncertainty related to the rotameter itself. The increase in the percentage of mismatch as the line length gets higher can be associated with the reducing flow rate with longer transmission. Still, the combined mismatch between the steady-state mass flow rates at two distant locations on the line is small, indicating the suitability of the isothermal assumption.

A more elaborate evaluation can be made by following the theoretical relations that define the temperature variation along the line. The steady-state pipe flow is generally represented by an adiabatic flow with friction [2]. The velocity of the media at the exit of the pipe is calculated from the measured volumetric flowrates and the corresponding temperature variation in an adiabatic flow at that velocity is obtained for each test. That calculated exit-velocity of the media, divided by the speed of sound at room temperature, makes for the mach number at the exit of the pipe:

$$u_{final} = \frac{Q_{final}}{A} \tag{1}$$

$$Ma = \frac{u_{final}}{c} \tag{2}$$

where $Q_{final}$ is the real volumetric flow rate at the exit of the line. For an adiabatic flow with friction, a local temperature of the media at a certain $Ma$ is related to its stagnation temperature as follows:

$$T_o = T_{final}(1 + \frac{k-1}{2} Ma^2) \tag{3}$$

where $k$ is the ratio of specific heats, $T_o$ is the stagnation temperature of the flowing media, and $A$ is the line cross-section area. $k$ is 1.4 for air. In our case, the stagnation temperature is the room temperature; since, the reservoir tank is held at room condition. Theoretical temperatures for each test were obtained along with the measured exit-velocity and $Ma$ that are presented in Table 2. As the $Ma$ at the exit drops, the theoretical change in final temperature gets smaller as expected. Therefore, our assumption becomes more and more realistic as the pipe length gets higher.

As seen in Table 2, the theoretical temperature variation from the stagnation temperature value gets less significant with the increased length of the line. The temperature variation is higher for high flow rates. A longer line reduces the flow capacity of the system, allowing for more heat exchange that would keep the air temperature fixed.

Table 2: Analysis of the Error in the Fixed Temperature Assumption

| Transmission Line Length (m) | Final Velocity (m/s) | Mach at the exit | Theoretical Temperature ($^oK$) | Theoretical Tempera-ture(%) |
|---|---|---|---|---|
| 8 | 112.8469199 | 0.328999767 | 286.7914893 | 2.118945635 |
| 6 | 130.675406 | 0.38097786 | 284.734492 | 2.820992498 |
| 3 | 167.5320833 | 0.48843173 | 279.6567084 | 4.554024422 |
| 1 | 215.6718232 | 0.628780826 | 271.5293425 | 7.327869437 |

## 3.2 Notes on Prior Studies

The tubes that transmit the mass flow between the valve and the actuator affect the pressure dynamics of the pneumatic system in two major ways [2], [38]: A pressure gradient is formed through the tube, introducing a magnitude change and a phase between the pressures at the inlet and exit of the line. This pressure difference curtails the flow through the valve, complicating the calculation of the mass flow rate. Also, since the air propagates along the tube as an acoustic wave, there is a significant pure time delay in delivery of mass to the actuator [56]. Although the effects of the transmission lines summarized above have been analyzed on a number of works [86], [85]; only a few of them suggests practical methods that can be applied for online control of pneumatic systems. Yang et al. approximated the line dynamics with a first-order transfer function and a time delay, explaining the difficulty in an analytical solution of the partial derivative equations that govern the mass flow rate through a tube [90]. Their approximation characterized the step response of a transmission line. An analytical solution to the governing partial derivative equations has been suggested by Richer and Hurmuzlu, in an effort to build a non-linear model for the line dynamics [56]. They assumed a constant velocity for the flow through the tube and simplified the governing equations to a classical one dimensional wave equation. In their method, the mass flow rate calculated using the aforementioned valve model was modified with an attenuation term which represents the resistance that a transmission

line puts on the system. In addition, a pure time delay was introduced between the mass flow rates at the inlet and exit of the tubes. They achieved very successful mass flow rate estimations for tube lengths up to 2 meters, using the resulting mass flow rate equation:

$$\dot{m}_c = \dot{m}_v(t - \frac{L}{c})exp^{-\frac{R_t RT}{2P}\frac{L}{c}} \tag{4}$$

where $\dot{m}_c$ and $\dot{m}_v$ describe the chamber and valve flow rates respectively and the exponent describes the attenuation in the mass flow due to the transmission lines. $L$ is the length of the line, $c$ stands for the speed of sound in air. Note that the mass flow rate across the valve is delayed by $\frac{L}{c}$. $P$ is the pressure at the exit of the line and $R_t$ is the tube resistance related to the Reynolds number $Re$ of the flow as follows:

$$R_t = \begin{cases} \frac{32\mu}{D^2} & \text{if } Re \leq 2300 \\ 0.158\frac{\mu}{D^2}Re^{0}.75 & \text{if } Re \geq 2300 \end{cases} \tag{5}$$

where $\mu$ is the dynamic viscosity of air and $D$ is the diameter of the line. The valve flow rate is a function of the pressure across its orifice and a discharge coefficient that corresponds to the potential flow limit of that orifice:

$$\dot{m}_v = c_f F_{(P_u, P_d)} \tag{6}$$

$c_f$ is referred as the discharge coefficient. $c_f$ achieves a theoretical maximum of 1, when the flow through the valve orifice is sonic [2]. $P_u$ and $P_d$ represent the pressures across the valve orifice.

We conducted a series of static flow experiment to see the applicability of this method on our system where the targeted transmission line length is 7.25 meter. The flow valve was excited to its full-range. Plastic tubes with a 4 mm of inside diameter and various lengths were connected to a reservoir tank and the mass flow rates from the tank to ambient air through the tubes are measured via a rotameter King Inc. 0-8 SCFM. The measured mass flow rates provided the Reynolds number in each flow,

Table 3: Measured Flow Rates and Corresponding attenuation Factors

| Length (m) | Mass Flow Rate ($kg/sec$) | Tube Resistance ($kgm^3/sec$ ) | Attenuation Factor | Resultant $c_f$ |
|---|---|---|---|---|
| 1 | $3.2x10^3$ | 775.64 | 0.5744 | 0.597 |
| 3 | $2.5x10^3$ | 610.48 | 0.1769 | 1.253 |
| 6 | $1.9x10^3$ | 489.67 | 0.0467 | 3.542 |
| 8 | $1.7x10^3$ | 434.15 | 0.0238 | 5.476 |

allowing us to calculate the tube resistances and hence the attenuation factors. The resulting attenuation factors and corresponding discharge coefficients for the valve orifices to achieve the measured mass flow rates are presented in Table 3.

The measured mass flow rates on Table 3 have a declining trend as the length of the tube is raised. That confirms the relation between the attenuation in the mass flow rate and the length of the transmission lines. However, the aforementioned method results in an unrealistic discharge coefficient for each tube length, except the 1 meter. Discharge coefficient represents the contraction in the effective flow area through an orifice and theoretically it needs to be lower than unity. The deviation from the theoretical boundary is higher for the longer tubes. Although, the effect of the tubes related to its length is apparent; the existing attenuation formula needs to be adjusted for a larger operation range.

## 3.3 Observations on the Dynamics of Fixed-Volume Chambers with Long Transmission Lines

The following experimental work has been made with a fixed-volume chamber, shown in Figure3.b and 3.c. Rather than the steady flow into the ambient, the aim was to investigate the transient flow into a finite-sized chamber. Pressure development in different locations along the line and the bandwidth of the system that includes a significantly long transmission were evaluated. The volume of the fixed-sized chamber

was selected to be nearly as half of the volume of the line. The dynamics of a non-tele-operated system was also observed for comparison. Figures 4 and 5 present the pressure variation in a system with no transmission lines. The valve and chamber pressures do not present a significant dynamic difference within the range of our study: up to 10 Hz. This very well complies with the works in the literature, as the directly-driven actuators have been shown to be capable of force tracking at 20 Hz reference [55],[74].

The bandwidth of the system reduces when a 7.25 m long transmission line was added between the valve and the chamber. The experiments presented by Figs. 4 and 5 were repeated on the tele-operated chamber. The resultant pressure variations are shown in Figs. 6 and 7.

MRI-compatible pneumatic actuators typically involve a graphite piston within a glass cylinder to comply with the magnetic susceptibility limitations. That graphite-glass combination has been preferred in many other applications, for it provides a low-friction assembly. However, one drawback of such assemblies is the non-negligible air leakage across the piston. In this dissertation, the actuators utilized in the experiments were chosen from the Airpel non-friction cylinder family that involves graphite pistons and glass cylinders, in order to implement a realistic test setup. To check whether the internal leakage across the piston in such actuators, the rear chamber of an Airpel actuator (E2.0DU) was connected to the valve without a long transmission line in between. The front chamber of the actuator was closed. The pressure variation at the valve outlet and the in the front chamber of the actuator were measured. The pressure in the rear chamber was calculated based on the measured force at the tip of the piston. Figure 8 presents the pressure variation in an inflated actuator, when the valve opening was suddenly opened to the ambient.

### 3.3.1 Discussion

The added volume of the connection tubes introduce a dynamic difference between the pressures at the inlet and the exit of the line, as seen in Figure 6. This additional dynamics results in a limited bandwidth in the pressure variation. Therefore, the valve pressures cannot be considered to accurately represent the chamber pressures under the presence of long transmission lines. Another observation is that the inlet ports of the chamber and the actuator did not present an important obstacle on the flow when there is a transmission line in the system. On the no-line setup, the chamber pressure and the valve pressure, which is also the inlet pressure for the chamber, had a transient difference. Due to the geometrical variations at the inlet holes, the chamber ports can become a factor in the pressure dynamics [2]. However; on the tele-operated setup, the rate of flow was reduced enough to prevent invoking such a difference. The rate of internal leakage was also a minor complication, as seen in Figure 7.

### 3.3.2 A Preliminary Model

Based on the initial experimental data presented in this chapter, a system model that accounts for line dynamics is developed. The transmission line is assumed as an intermediate chamber connected between the reservoir and the actuator in series as shown in Figure 9.

The flow through the valve, $\dot{m}_v$, is calculated as explained in the valve equation (6), where the pressure in the line, $P_{line}$ is either the upstream or downstream pressure depending on the direction of the flow. The inertia of the air is neglected (i.e. the flow is assumed as steady) and the flow rate to the actuator, $\dot{m}_f$, is realized through the relation between the friction and the pressure drop along the line that is represented by the pressure difference between the line and the chamber:

$$\Delta P = P_{line} - P_{chamber} \tag{7}$$

On a steady flow, the following relation between the the pressure drop along the line and friction is hold [46]:

$$\Delta P = R_t u L_t \tag{8}$$

where $R_t$ is the aforementioned flow resistance in the line [56], $u$ is the velocity of the flow and $L$ is the length of the transmission line. The relation between the velocity of the flow and the mass flow rate is given as follows:

$$\dot{m}_f = \rho u A \tag{9}$$

By substituting the flow rate into the definition of the pressure drop in (8), the following relation between the flow rate and the pressure drop is obtained:

$$\dot{m}_f = \Delta P \times a \quad \text{where} \quad a = \frac{\rho A}{L R_t} \tag{10}$$

In order to calculate the coefficient, $a$, both $R_t$ and $\rho$ have to be known. If those parameters are estimated without involving the pressures in the line and chamber, the model does not compromise the stability of the observer which is one of the criteria we are looking for in a model. Therefore, those parameters are calculated using the pressure measurements at the valve ports, $P_v$. $\rho$ can be calculated via ideal gas law:

$$\rho = \frac{P_v}{RT} \tag{11}$$

The calculation of $R_t$ requires the to know the Reynolds Number of the flow, hence, the mass flow rate through the line. That flow rate is again estimated by substituting the measured valve pressure to the valve equations. That preliminary estimation on the mass flow is utilized to calculate a Reynolds Number that yields the flow resistance [56]. Therefore, the calculation of $a$ is only based on the measured quantity $P_v$. The pressures in the line and actuator chamber is then obtained assuming them as isothermal:

$$\dot{m}_v - \dot{m}_f = \dot{P}_{line} V_{line} \tag{12}$$

$$\dot{m}_f = \dot{P}_{chamber} V_{chamber} + P_{chamber} \dot{V}_{chamber} \tag{13}$$

Adding a serially connected volume between the reservoir and the actuator alternates the relation between the mass flow rate and actuator pressure. The difference is illustrated in Figure 9 where the simulated variation of the mass flow rate with respect to the ratio of downstream to upstream pressure is presented. Negative flow rate represents an outflow from the actuator. Only the mass flow entering/exiting the actuator is considered. The pressure ratio is selected as $\frac{P_{actuator}}{P_{reservoir}}$ when the actuator chamber is being charged, and $\frac{P_{atm}}{P_{actuator}}$ when discharged. The preliminary model is less aggressive when the pressure ratio is low compared to the conventional model due to the intermediate volume connected to the actuator in the new method.

### 3.3.3 Preliminary Analysis

The accuracy of the established model was checked on a the experimental setup shown in Figure 3.b. The system is assumed to be isothermal.

The pressure in the chamber was measured and compared to the pressure estimation of the conventional and proposed preliminary models. Figure 10 illustrates the measured and estimated pressures for three different full-scale valve excitation profiles: Step input, 2 Hz, and 5 Hz sinusoidals.

The developed preliminary model achieved a significantly improved pressure estimation compared to the conventional model. The difference between them increases as the frequency of the valve excitation is increased. The new model preserved its accuracy even at 5 Hz which is significantly high for a tele-operated pneumatic system. This preliminary analysis confirms the modeling approach of segmenting the system as serially connected chambers and the assumptions introduced with it. However, the estimation of the developed model presented high-frequency deviations from the actual pressure. This could be attributed to the discontinuity in the definition of the line resistance and the increasing depth in the pressure gradient along the line as the

line gets longer.

## 3.4 Summary

This section presents preliminary models and observations made on the flow dynamics through the transmission lines. The experiments described in this chapter were oriented to form a basis for the simplifications and assumptions that are utilized in the advanced methods presented in the following chapters. The isothermal flow assumption was checked by steady-state, constant line flow experiments. The results indicated that the assumption of a fixed temperature along the transmission line is not inaccurate. The transmission lines reduce the flow capacity of a valve and introduce a dynamic difference between the valve and chamber pressures. That difference is significant even at 2 Hz valve excitation frequency. The actuator ports, on the other hand, presented no significant limitations on the flow. Also, the internal air leakage across the actuator piston presented a limited influence on the pressure drop. A primitive line model that was prepared based on the these observations achieved a more accurate pressure estimation than the classic pneumatic system modeling techniques. The preliminary model presented in this chapter provided the basis of a more advanced estimation method that is explained in chapter VI.

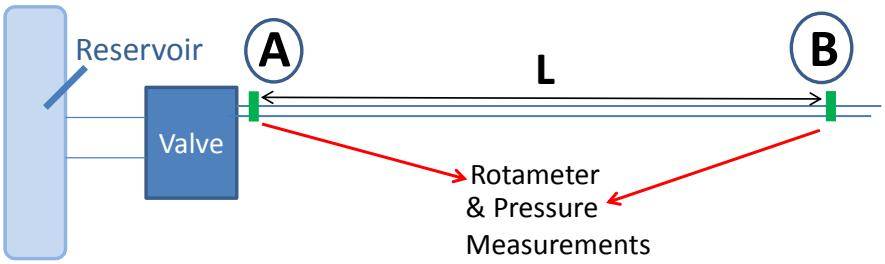


(a)

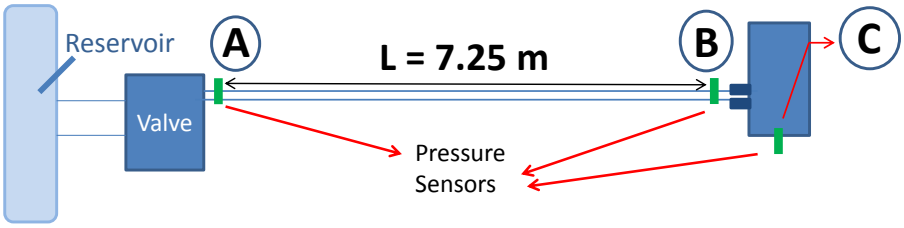


(b)

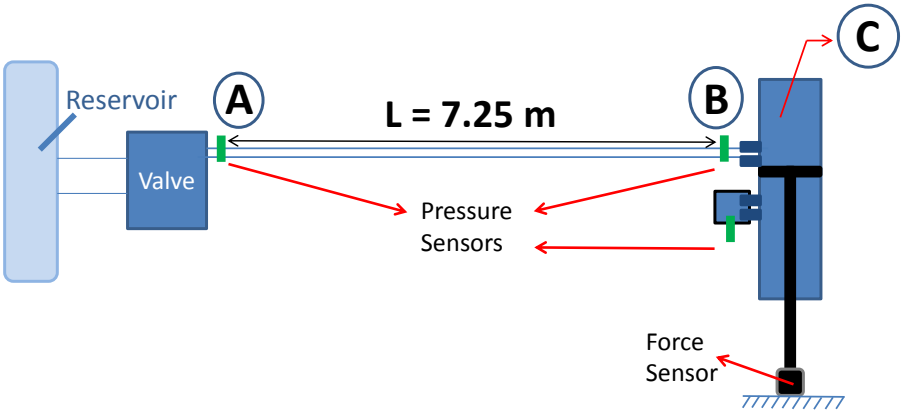


(c)

Figure 3: The measurement setups for preliminary analysis on the line flow. a) Steady-state flow experiments with rotameter measurements at two locations on the line b) Fixed-sized chamber experiments with a 7.25 m long transmission line b) Fixed-sized actuator chamber flow tests with a 7.25 m long transmission line

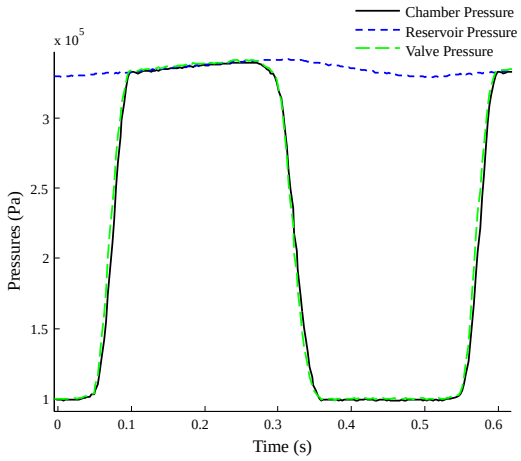


(a)

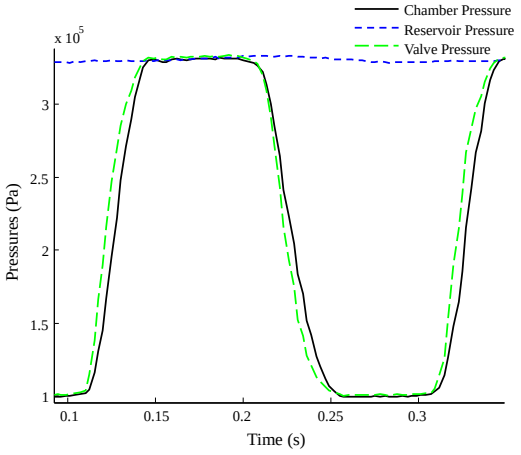


(b)

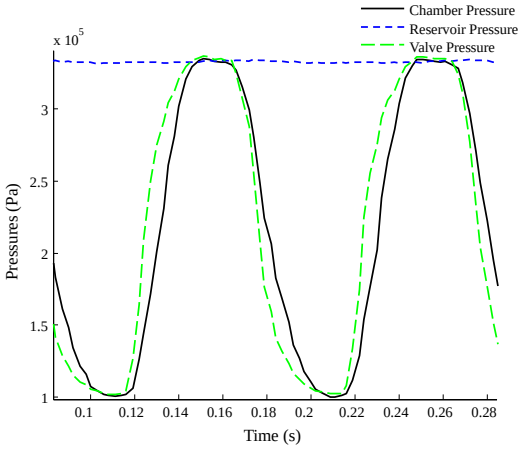


(c)

Figure 4: Measurements on a setup with no transmission line with a) 2 Hz valve excitation b) 5 Hz valve excitation b) 10 Hz valve excitation

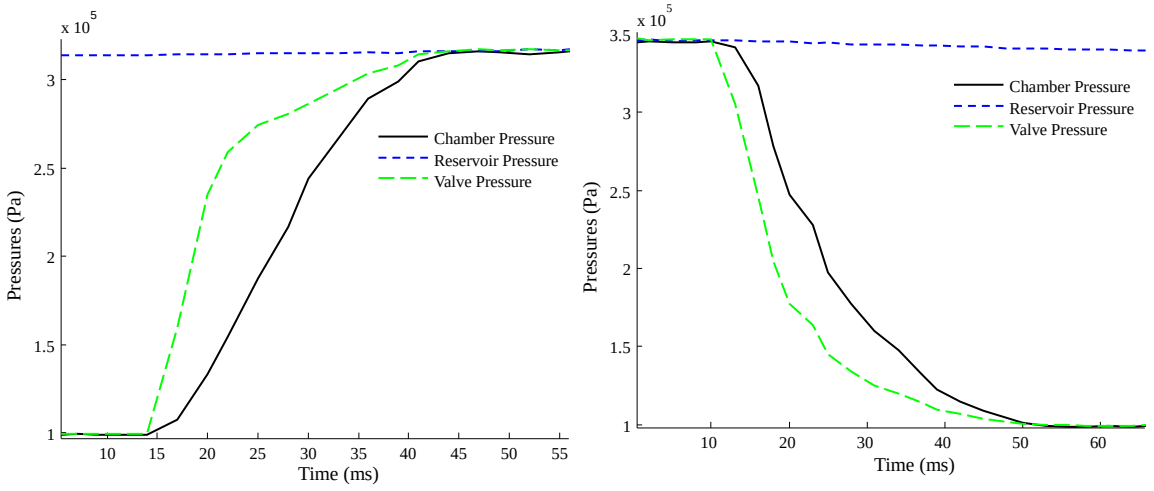


Figure 5: Measurements on a setup with no transmission line with a step input a) Pressurization b) Depressurization

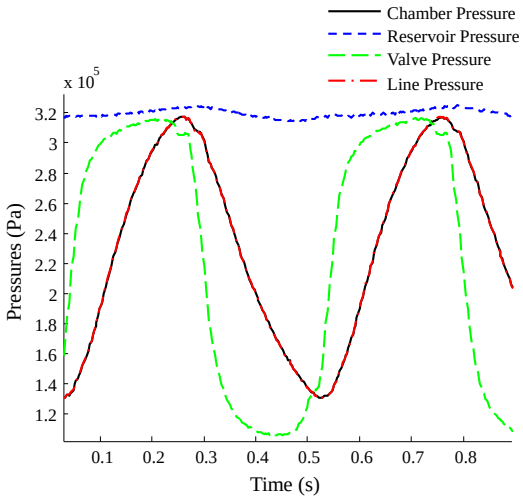


(a)

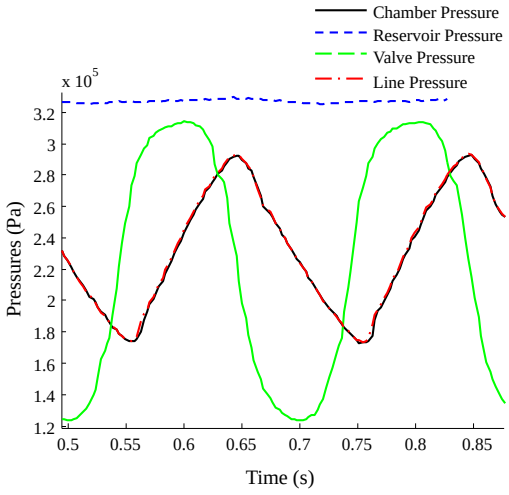


(b)

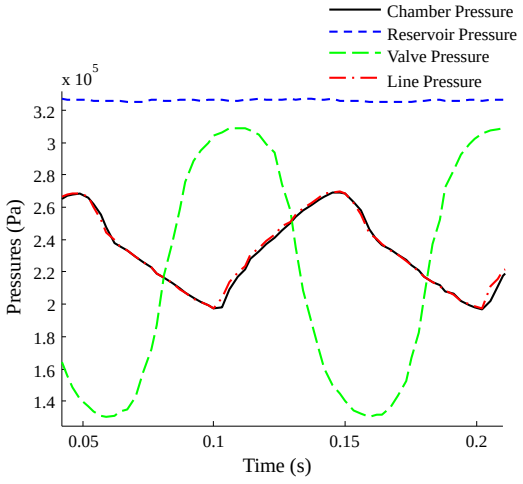


(c)

Figure 6: Measurements on a setup with 7.25 meters long transmission with a) 2 Hz valve excitation b) 5 Hz valve excitation b) 10 Hz valve excitation

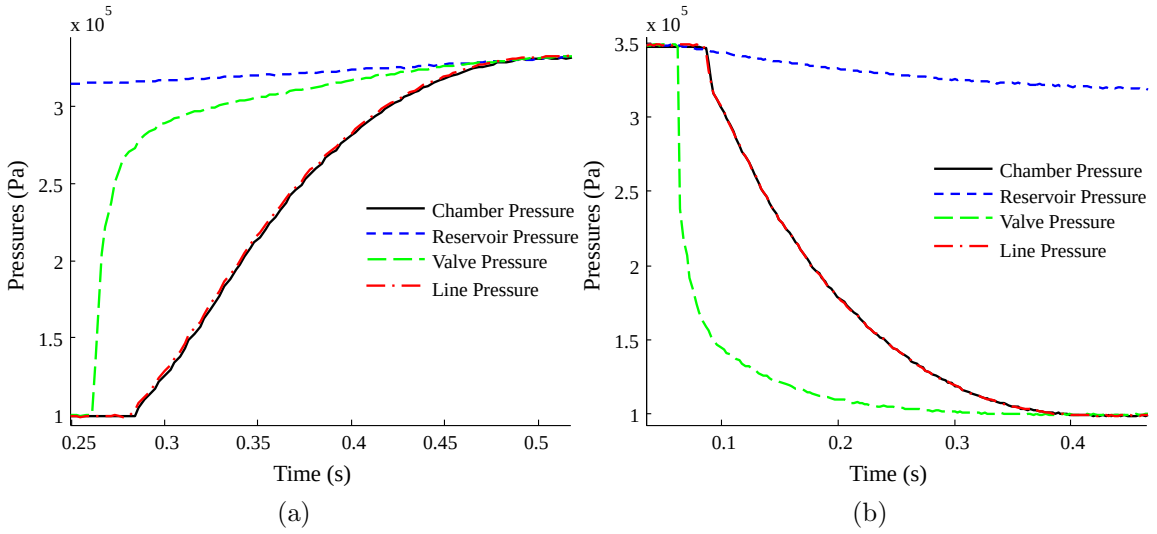


Figure 7: Measurements on a setup with 7.25 meters long transmission with a step input a) Pressurization b) Depressurization

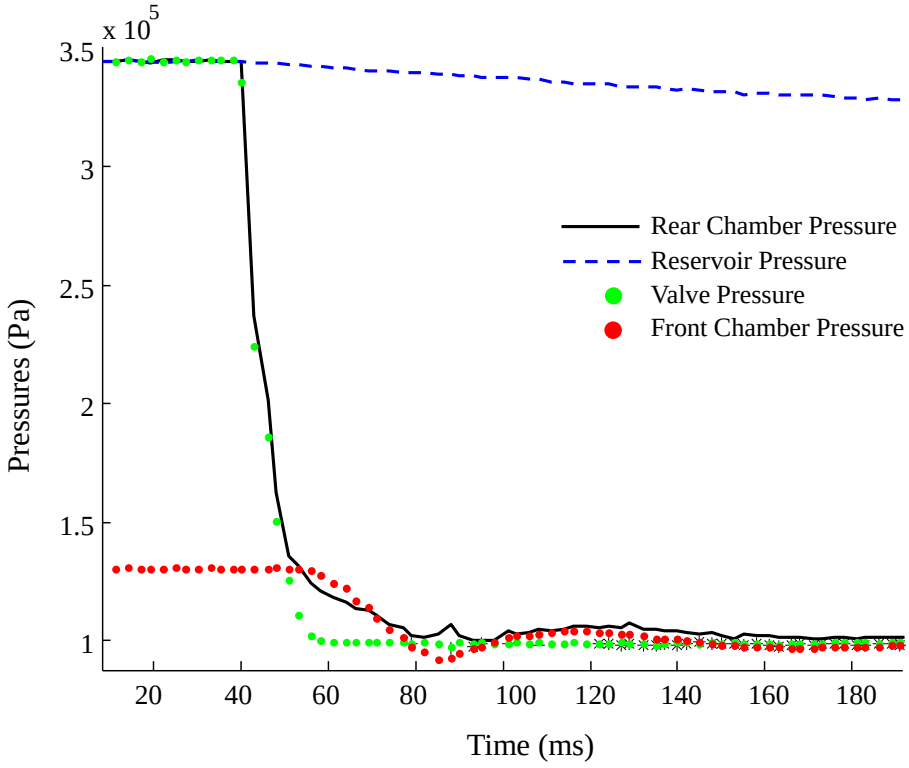


Figure 8: Measurements on a setup with no transmission line with a step input

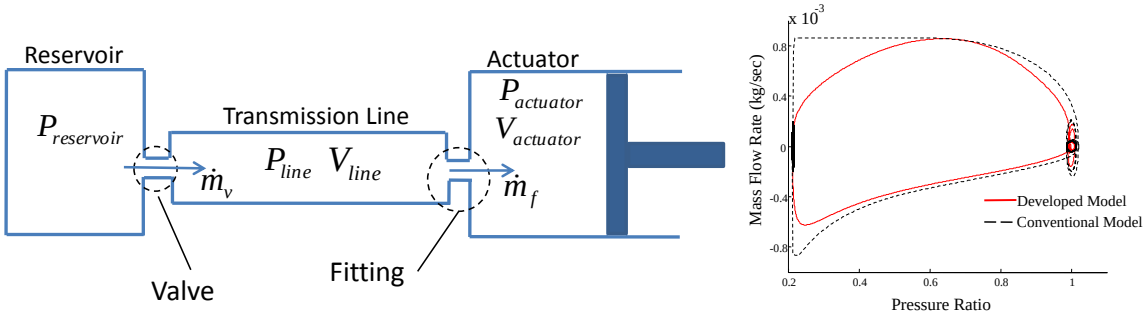


(a) (b)

Figure 9: The preliminary model for tele-operated pneumatic systems (a) Schematics (b) The resultant change in the relation between the mass flow rate and system pressures

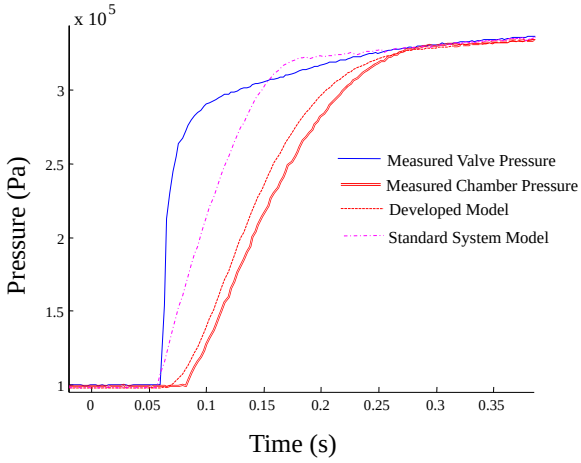


(a)

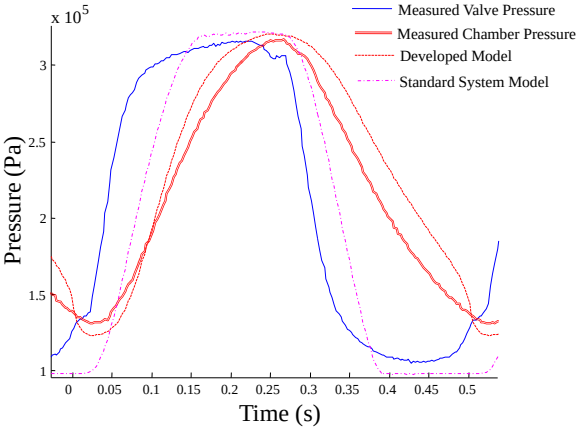


(b)

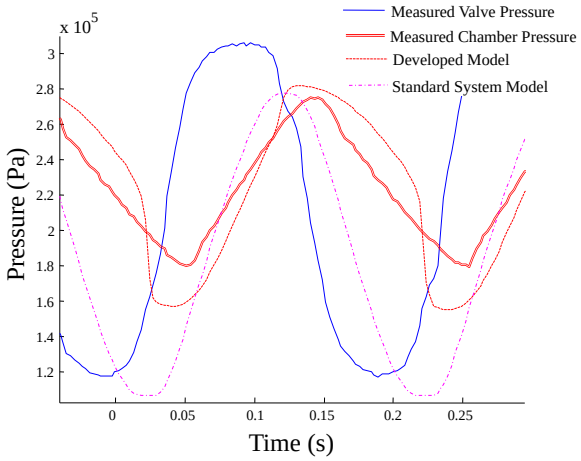


(c)

Figure 10: Estimated and measured chamber pressures on fixed-volume chamber pressurization tests with the valve input being (a) Step signal (b) 2 Hz sinusoidal (c) 5 Hz sinusoidal

# CHAPTER IV

# AN ASYMPTOTICALLY STABLE PRESSURE OBSERVER BASED ON LOAD AND DISPLACEMENT SENSING FOR PNEUMATIC ACTUATORS WITH LONG TRANSMISSION LINES

Pneumatically actuated systems became increasingly popular in mechatronic and robotic applications for their improved compactness and efficiency [83],[63]. In the recent years, the use of pneumatic systems has been preferred to conventional actuation methods on new areas such as tele-operated medical robots[8], [89], wearable human assistive devices[6], and humanoids[78] by virtue of their inherent compliance, and suitability for safe and clean operations. In particular, pneumatic actuation is preferred to hydraulic systems on human-robot interfaces as the force range required for human interaction is limited and the compressibility of air provides additional compliance. Pneumatic actuators can be built compatible to MRI, where electromagnetic motors would pose a danger. Compressed air is commonly available in health-care units, making pneumatic systems low-cost and efficient. To improve the performance of pneumatically actuated systems, pressure information is used and combined with a controller. When direct pressure measurement is not available or not desirable in some circumstances, pressures can be estimated by a model of the system, called pressure observer.

Pressures in the actuator chambers can be challenging to acquire when the system dynamics involves aforementioned complexities that restrict direct pressure measurement. For instance, the use of pressure sensors is limited on the robots that operate in MRI rooms in order to prevent magnetic interference with MRI scanners. All ferrous

components, including pressure sensors, are located outside the MRI environment and are connected to the actuator via transmission lines. Transmission lines introduce a time-delay and additional dynamical relation between the readings of the pressure sensors and actuator pressures. Even in other applications where the pressure sensors are located close to the actuator, the measurement accuracy can be reduced by the additional flow resistance at the connection ports of the actuator and air leakage across the piston. In the absence of direct pressure measurement, the actuator pressures have been estimated, using standard system models.

This chapter presents an algorithm that utilizes force and displacement feedback to compensate for the mitigated accuracy of standard pneumatic system modeling under the presence of unmodeled dynamics. The standard pneumatic system modeling is outlined in the next section for reference.

## 4.1 A Standard Dynamic Model of Pneumatic Systems

A typical pneumatic system consists of a cylinder with a piston that divides the cylinder into two chambers and control valves that regulate the flow to/from the cylinder. Compressible air flow through the valve is transformed into linear motion actuated by pressure differential between the chambers. This section outlines a well-established model for each component. The combination of these individual models is referred as the standard model in the rest of the paper and will be used as a basis for evaluating the performance of the proposed observer.

### 4.1.1 Valve

The mass flow through a pneumatic valve is widely characterized as an isentropic flow through a frictionless orifice [57]. The following relation between the area of the valve orifice and mass flow rate is given assuming steady-state boundary conditions [2]:

$$\dot{m}_{v_i} = (C_{(u_v)})\psi(P_u, P_{d_i}) \tag{14}$$

where $C_{(u_v)}$ is the net conductance of the valve at a given input command, $u_v$, and $\psi$ is a piecewise function of the upstream ($P_u$) and downstream ($P_{d_i}$) pressures across the valve. A detailed explanation on the formulation of $\psi$ and the relation between the conductance, $C_{(u_v)}$, and the valve input command, $u_v$, are given in Appendix A. For the sake of readability, the conductance, $C_{(u_v)}$, is referred as the control input, denoted by $u$, in this thesis.

In this paper, the dynamics of the spool of a valve is neglected as the valve's bandwidth is in general significantly higher than the bandwidth of operation. In general, neglecting spool dynamics combined with quasi-static flow equations results in an aggressive model, since the transient phase of the mass flow is not considered.

#### *4.1.1.1 Chamber Dynamics*

The dynamic relationship between the displacement of the actuator piston and valve input can be characterized by the mass flow rate. Using the ideal gas law and continuity equation, the following dynamic expression of the chamber pressure is obtained:

$$r\dot{m}RT = rP\dot{V} + \dot{P}V \tag{15}$$

where $r$ varies from 1 to 1.4 depending on the level of heat transfer when the chamber is being charged or discharged. $r$ becomes 1 for the isothermal process and 1.4 for the adiabatic [1], [69]. $R$ is the ideal gas constant and $V$ represents the volume of the chamber being charged/discharged.

When the length of the transmission line is considerably long, e.g. the teleoperation case, the volume that is being charged/discharged has to involve the volume of the line. Therefore, in a conventional model, the effective volume becomes:

$$V = V_{actuator} + V_{line} \tag{16}$$

with $V_{actuator}$ as the chamber volume and $V_{line}$ as the fixed volume of the transmission line that is connected to that chamber.

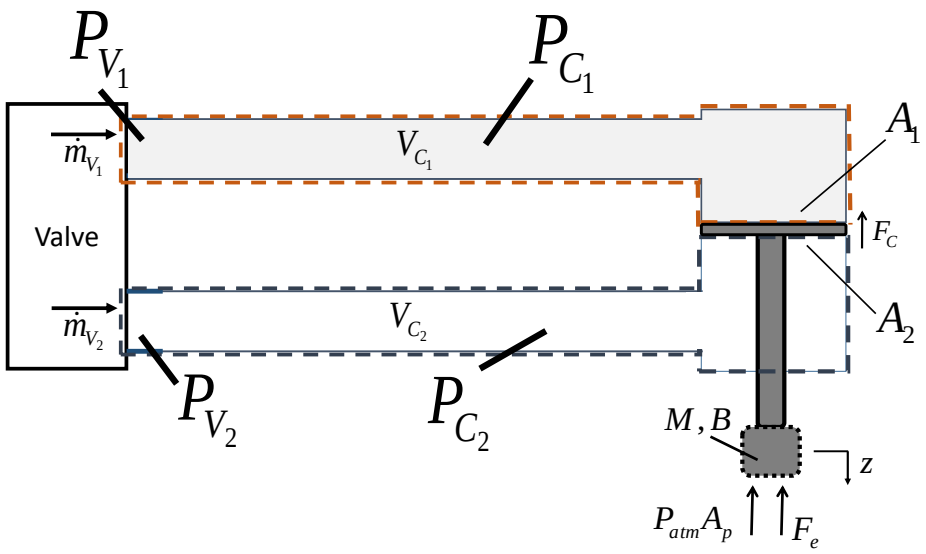


Figure 11: Free-body diagram of the actuator piston with the schematics that shows the classical pneumatic system modeling

By combining the volume of the transmission line and actuator chamber, a standard model of chamber dynamics assumes a homogeneous pressure distribution along the system beyond the valve. Hence, this model cannot characterize the pressure gradient along the transmission line introduced by friction.

#### *4.1.1.2 Piston Dynamics*

The piston of a pneumatic actuator is displaced by the pressure difference between the chamber pressures, shown in Fig 11. The magnitude of the force produced by an actuator, referred as actuator force, $F_p$, is given by:

$$F_p = P_1 A_1 - P_2 A_2 - P_{atm} A_p \tag{17}$$

where $A_1$ and $A_2$ represent the piston areas of the rear and front chambers respectively, and $A_p$ is the area of the piston rod.

The relationship between the dynamics of the piston and the actuator force is represented by the following equation:

$$F_p = F_e + M\ddot{z} + B\dot{z} + F_c sign(\dot{z}) \tag{18}$$

The dynamics of the piston is characterized by an inertia and a damping constant: $M$ and $B$ respectively. The external force, $F_e$, can be measured by using a force sensor attached to the tip of the piston rod. In our study, possible coulomb friction across the piston, $F_c$, is neglected for the actuator being utilized has a graphite piston that produces negligible friction over glass surfaces.

## 4.2 Design of the Proposed Observer

The standard pneumatic system model outlined in the previous section would oversee the additional dynamics on a tele-operation setup introduced by transmission lines. In the absence of pressure sensors, the accuracy of pressure observation via standard model could be improved by measuring force and displacement at the piston.

### 4.2.1 Proposed Observer Dynamics

In the proposed observation method, state variables are chosen as the stored energy in the system [24]:

$$x = \begin{bmatrix} x_1 \\ x_2 \end{bmatrix} = \begin{bmatrix} P_1 V_1 \\ P_2 V_2 \end{bmatrix} \tag{19}$$

Since the volume of each chamber can be easily calculated from the position sensor reading, individual chamber pressures can be obtained by:

$$P_1 = \frac{x_1}{V_{line} + (\frac{L_p}{2} - \Delta z) A_1} \tag{20}$$

$$P_2 = \frac{x_2}{V_{line} + (\frac{L_p}{2} + \Delta z) A_2} \tag{21}$$

where $P_{1,2}$ is the pressure in an actuator chamber, and $L_p$ is the length of the cylinder stroke shown in Figure 11.

Considering the chambers as isothermal, i.e. $r = 1$ in (15), the derivative of the states can be modeled by flow rates [24]. Measured force and piston displacement are utilized to correct errors in the estimated state variables, $\widehat{x_{1,2}}$, and help them

converge:

$$\dot{\widehat{x}} = \begin{bmatrix} \dot{\widehat{x}}_1 \\ \dot{\widehat{x}}_2 \end{bmatrix} = \begin{bmatrix} \widehat{\dot{m}_1} RT \\ \widehat{\dot{m}_2} RT \end{bmatrix} + k \begin{bmatrix} f_1(\widehat{F_p} - F_p) \\ f_2(\widehat{F_p} - F_p) \end{bmatrix} \tag{22}$$

where $\widehat{\dot{m}_{1,2}}$ represent estimated mass flow rates. $k$ is a scalar observer gain, and $\widehat{F_p}$ is the observed actuator force calculated from estimated pressures $\widehat{P_1}$ and $\widehat{P_2}$ by (17). The external force, $F_e$, and position, $z$, measurements can be substituted into (18) to obtain the measured actuator force denoted by $F_p$. The velocity, $\dot{z}$, and acceleration, $\ddot{z}$, of the piston can be obtained by subsequent numerical derivations of the position measurement. The difference between the observed and measured actuator force is utilized by functions $f_1$ and $f_2$ given as:

$$\begin{aligned} f_1 = -\frac{1}{V_1 A_2} \{ & \hat{P}_1 A_1 - \hat{P}_2 A_2 - P_{atm} A_p \\ & - (F_e + M\ddot{z} + B\dot{z}) \} \end{aligned} \tag{23}$$

$$\begin{aligned} f_2 = +\frac{1}{V_2 A_1} \{ & \hat{P}_1 A_1 - \hat{P}_2 A_2 - P_{atm} A_p \\ & - (F_e + M\ddot{z} + B\dot{z}) \} \end{aligned} \tag{24}$$

The proposed observer given in (22) is comprised of estimated mass flow rates and correction terms based on force and displacement measurements. The flow rates are calculated by using estimated pressures on (14)-(89). The correction terms minimize the difference between estimated actuator force, $\hat{F}_p$, and measured actuator force, $F_p$. To achieve asymptotic stability with regard to estimation errors, the following control scheme is introduced:

$$A_{v_1} A_{v_2} < 0 \tag{25}$$

This condition is common for generic valves to enable flow control of two chambers with single control input. Four-way valves inherently satisfy this condition. The proposed observer can still preserve its stability regardless of the condition of the mass flow to the system. In addition, the proposed observer guarantees a limited reduction in observation accuracy in the presence of measurement errors. The proof

of the asymptotically stable pressure observation and the analysis of robustness will be provided in the following sections. In this paper, observer stability refers to the convergence of pressure estimation error to zero.

#### *4.2.1.1 Proof of Asymptotically Stable Pressure Observation based on Force Feedback*

Following Gulati and Barth's approach [24], a Lyapunov candidate that represents the error in the stored energy between the actual and observed systems is selected to show the stability of the observer equations:

$$L = \frac{1}{2}\boldsymbol{e}^T\boldsymbol{e} = \frac{1}{2}(\tilde{x_1}^2 + \tilde{x_2}^2) \tag{26}$$

where $\boldsymbol{e}$ is defined as:

$$\boldsymbol{e} = \begin{bmatrix} \tilde{x_1} \\ \tilde{x_2} \end{bmatrix} = \begin{bmatrix} \hat{x_1} - x_1 \\ \hat{x_2} - x_2 \end{bmatrix} \tag{27}$$

Given the observer equations in (22), $\dot{\boldsymbol{e}}$ becomes:

$$\dot{\boldsymbol{e}} = \dot{\boldsymbol{e}}_m + \dot{\boldsymbol{e}}_f \tag{28}$$

where $\dot{\boldsymbol{e}}_m$ and $\dot{\boldsymbol{e}}_f$ are related to the errors in the estimated mass flow rates and actuator force respectively:

$$\dot{\boldsymbol{e}}_m = \begin{bmatrix} (\hat{\dot{m}_1} - \dot{m}_1)RT \\ (\hat{\dot{m}_2} - \dot{m}_2)RT \end{bmatrix} \tag{29}$$

$$\dot{\boldsymbol{e}}_f = k \begin{bmatrix} f_1(\hat{F_p} - F_p) \\ f_2(\hat{F_p} - F_p) \end{bmatrix} \tag{30}$$

Consequently, the derivative of the positive-definite function in (26) involves both the control inputs for the system and force measurement. Differentiating (26), and substituting (29) and (30):

$$\dot{L} = \boldsymbol{e}^T\dot{\boldsymbol{e}}_m + \boldsymbol{e}^T\dot{\boldsymbol{e}}_f \tag{31}$$

which leads to:

$$\dot{L} = \tilde{x_1}\tilde{\dot{m}_1}RT + \tilde{x_2}\tilde{\dot{m}_2}RT + k(\tilde{x_1}f_1(\tilde{F_p}) + \tilde{x_2}f_2(\tilde{F_p})) \tag{32}$$

where $\tilde{F_p}$ respresents the error in the actuator force estimation, i.e. $\hat{F_p} - F_p$.

The derivative, $\dot{L}$, can be shown to be negative semi-definite, satisfying the Lyapunov stability requirements for the observer. The following statement proven in [24] guarantees the negative semi-definiteness of the first product, $\boldsymbol{e}^T\dot{\boldsymbol{e}}_m$, in (31):

$$\begin{aligned} \tilde{x_i}\tilde{\dot{m}_i} &\leq 0 \text{ if } A_{v_i} \geq 0 \\ &< 0 \text{ if } A_{v_i} < 0 \end{aligned} \tag{33}$$

The second product, $\boldsymbol{e}^T\dot{\boldsymbol{e}}_f$, is related to the correction terms and can be shown to be negative semi-definite as well. The proof of this term being negative semi-definite is given in Lemma 1, followed by the proof of stability of the observer in Lemma 2. Then, asymptotic stability of the observer in the condition described by (25) is proven in Theorem 1.

**Lemma 1:** The product $\boldsymbol{e}^T\dot{\boldsymbol{e}}_f$ is negative semi-definite regardless of the condition of the air flow in the system, or the position of the piston.

**Proof of Lemma 1:** The product mentioned leads to the following expression:

$$\boldsymbol{e}^T\dot{\boldsymbol{e}}_f = -k\left(\tilde{P}_1\sqrt{\frac{A_1}{A_2}} - \tilde{P}_2\sqrt{\frac{A_2}{A_1}}\right)^2 \tag{34}$$

which is negative semi-definite for $k > 0$. Therefore, this lemma can be satisfied with the choice of a positive value for $k$.

**Lemma 2:** The pressure observer described in (22) is globally Lyapunov stable with regard to the errors in the estimated pressures.

**Proof of Lemma 2:** Being a radially unbounded, positive-definite, scalar Lyapunov function; $L$ in (26) is zero if and only if the errors in estimated pressures are zero. The statement given in (33), combined with the results of Lemma 1, assures $\dot{L}$ to be negative semi-definite.

**Theorem 1:** The pressure observer described in (22) is globally asymptotically Lyapunov stable with regard to the errors in the estimated pressures, if at least one of the actuator chambers is guaranteed to be in the discharge mode.

**Proof of Theorem 1:** As explained in the proof of Lemma 2, $L$ in (26) is a globally stable Lyapunov function. To prove Theorem 1, the following statement will be satisfied to ensure the asymptotic stability of $L$ according to invariant set theorem [66]:

$$\dot{L} = 0 \textit{ if and only if } L = 0$$

The equilibrium of the error dynamics, $\dot{L} = 0$, requires both $\boldsymbol{e}^T\dot{\boldsymbol{e}}_m$ and $\boldsymbol{e}^T\dot{\boldsymbol{e}}_f$ to be individually zero, since they are negative semi-definite functions. $\boldsymbol{e}^T\dot{\boldsymbol{e}}_m$ becomes negative-definite when at least one of the actuator chambers is in the discharging mode, as outlined in (33). The condition given in (25) guarantees this situation, leading to the statement below:

*Assuming* $A_{v_1}A_{v_2} < 0$*; if* $\boldsymbol{e}^T\dot{\boldsymbol{e}}_m = 0$*, then:*

$$\tilde{x_1}\tilde{x_2} = 0 \tag{35}$$

The remaining part of $\dot{L}$, $\boldsymbol{e}^T\dot{\boldsymbol{e}}_f$ given in (34), becomes zero if and only if the following condition is met:

$$\tilde{x_1}\frac{A_1}{V_1} = \tilde{x_2}\frac{A_2}{V_2} \tag{36}$$

The equilibrium point, $\dot{L} = 0$, strictly requires both (35) and (36), which is satisfied if and only if $\widetilde{x_{1,2}} = 0$. Therefore, the proof of Theorem 1 can be concluded by showing that the observer satisfies global invariant set theorem as follows:

$L_{(\tilde{P}_1,\tilde{P}_2)}$ *is a radially unbounded Lyapunov function,* $\dot{L}$ *is negative semi-definite, and* $\tilde{\boldsymbol{x}} = 0$ *is the only set where* $\dot{L} = 0$*.*

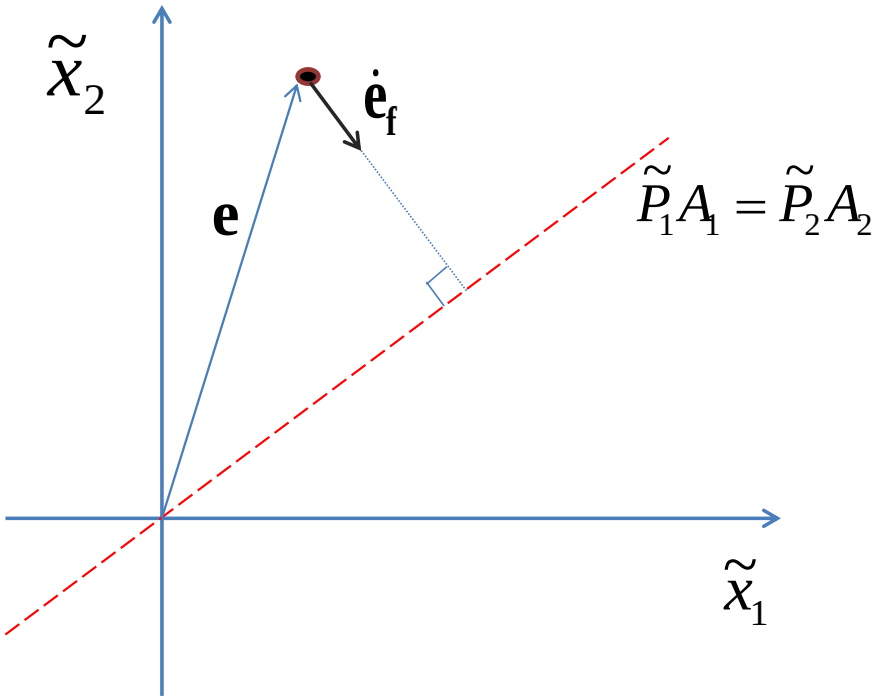


Figure 12: The role of the error correction terms on the pressure observation

Then, the system described by the scalar function $L$ globally asymptotically converges to $\tilde{\boldsymbol{x}} = 0$ as $t \to \infty$.

The proof of Theorem 1 assures an asymptotical decrement in the magnitude of the error defined in (27). Asymptotical stability is accomplished by imposing a relationship between the estimated pressures, using the correction term. The role of the correction term, $\dot{\boldsymbol{e_f}}$, on the convergence of observation errors at an arbitrary instant is elaborated in Figure 12. That term imposes the errors to converge to a theoretical valley that has a time-variant slope, interpretation of which is given in (36). The term is designed to point in the direction towards that valley at right angles, assuring a reduction in the magnitude of $\boldsymbol{e}$. The scalar gain, $k$, affects the magnitude of $\dot{\boldsymbol{e_f}}$; hence, the convergence rate towards the valley. This method keeps the errors from diverging independently and they drag each other to the origin when either of the estimated states is converging to true value, e.g. in the discharge mode. Note that the part of $\dot{\boldsymbol{e}}$ associated with the system model, $\dot{\boldsymbol{e_m}}$, always reduces the

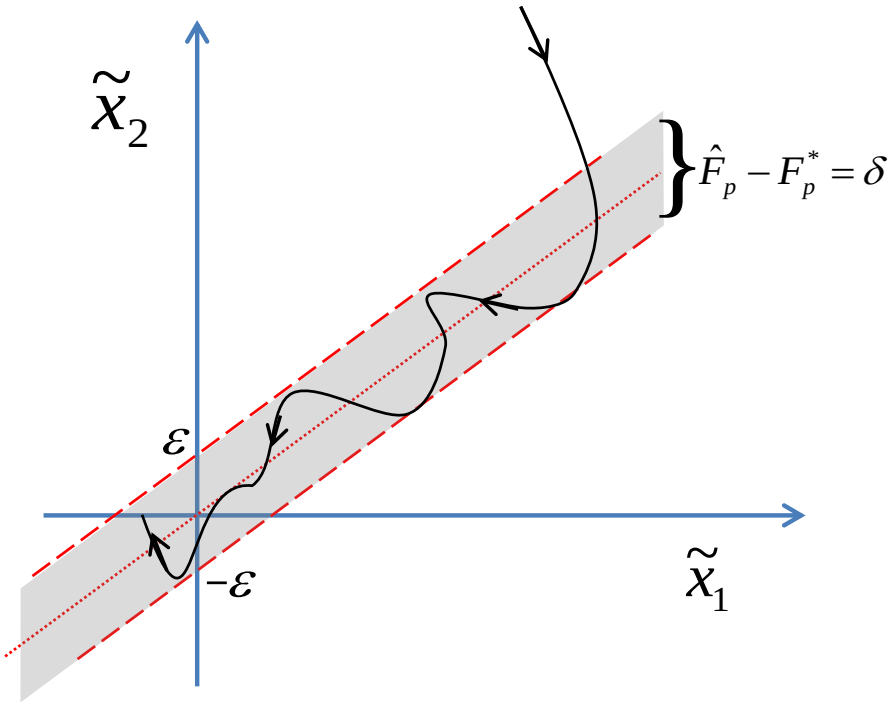


Figure 13: Robustness of the proposed algorithm against the errors in the calculation of actuator force

estimation error of at least one of the estimated states, under the condition (25).

The proposed observer equations contain both pressure dynamics of the pneumatic system and dynamics of the piston individually, i.e. the part that is derived from the original pneumatic system model does not require any knowledge on the load dynamics and vice versa. Therefore, any uncertainty arisen from either one does not affect the other. The following analysis assures the robustness of the pressure estimation despite any uncertainty associated with actuator force measurement errors.

### 4.2.2 Robustness of the Proposed Method

The proposed correction algorithm guarantees a robust estimation against disturbances in the measurement of the actuator force, $F_p$, that is obtained by (18). The uncertainty related to the measurement of the environmental force, $F_e$, the identified

impedance parameters, or the numerical derivations of $z$ is assumed to be bounded. Let

$$F_p = F_p^* + \delta \tag{37}$$

where $F_p^*$ represents the true value of the actuator force and $\delta$ is a bounded error, defined as:

$$-\epsilon < \delta < \epsilon \tag{38}$$

As the correction algorithm minimizes the difference between the estimated, $\widehat{F_p}$, and measured actuator force, $F_p$; the errors in the observed states converge to a bounded region shown in Figure 13, i.e. $\hat{F}_p - F_p^* = \delta$. Following the same Lyapunov function described in (26), the correction related part of the derivative of the Lyapunov function, given in (34), becomes:

$$\boldsymbol{e}^T \dot{\boldsymbol{e}}_f = -\frac{k}{A_1 A_2} \left( \left( \widetilde{F_p^*} - \frac{\delta}{2} \right)^2 - \frac{\delta^2}{4} \right) \tag{39}$$

where

$$\widetilde{F_p^*} = \hat{F}_p - F_p^* \tag{40}$$

This expression reduces to zero when $\widetilde{F_p^*}$ equals to zero or $\delta$, and becomes negative outside the interval [0,$\delta$]. Therefore, as $\widetilde{F_p^*}$ converges to a value within that interval; the estimation converges to a point where the flow rate related negative semi-definite term, $\boldsymbol{e}^T \dot{\boldsymbol{e}}_m$, and the correction related term, $\boldsymbol{e}^T \dot{\boldsymbol{e}}_f$, cancel each other. That means the estimation stays within a bounded region, defined by the disturbance term, $\delta$, as shown in Figure 13.

Apart from the uncertainty in the feedback, the observer equations involve perturbations related to the flow parameters in (88), due to the temperature variations and calibration errors. Assuming those perturbations to be bounded, the modeling part of the observer equations (22)-(24) lead to a bounded steady-state bias, as discussed by Gulati and Barth [24].

### 4.2.3 Experimental Setup

The accuracy of the proposed observer was verified by performing typical force control experiments. A double acting cylinder (Airpel E2.0DU) was connected to a four-way spool valve (FESTO MPYE-5-1/8-LF-010-B) via 7.25 m long transmission lines of 4 mm inside diameter. Pressure was measured by analog pressure sensors (SSI Technologies P51 series) at the four locations shown in Figure 14: at the inlet of each actuator chamber and at each exit port of the spool valve. The pressure measured at the inlet of each actuator chamber was regarded as true pressure in the corresponding chamber. The actuator is chosen to be of short stroke and small volume in order to minimize difference between the pressures in the actuator chambers and pressure readings at the inlet ports of the actuator. The external force applied to the actuator was measured by a load cell (FUTEK LSB200) attached at the tip of the piston rod. The piston was connected to a spring system that provided an external force proportional to the piston displacement, as shown in Figure 14. The piston position was measured by using a Honeywell linear potentiometer (model F38000106). The velocity and acceleration of the piston are obtained by numerical differentiation with a first-order filter at 50 Hz. The system was controlled by a platform of Intel i7 @2.80GHz processor with 6.00 GB RAM, where the control algorithm were implemented using Labview. The National Instruments A/D board (NI USB-6343) was used for data acquisition.

The pressure of the reservoir was set to 34 kPa and its fluctuation was monitored by a pressure sensor similar to the ones used for line and valve pressure measurements. The inertia and damping coefficients of the actuator piston were experimentally derived by performing motion tests while the actuator chambers were kept open. Similarly, the stiction of the piston-cylinder was identified to be 0.25 N, which was negligibly small compared to the range of force of the actuator. The sonic conductance of the valve, $C_{A_{v_i}}$, was determined through a series of calibration tests by following

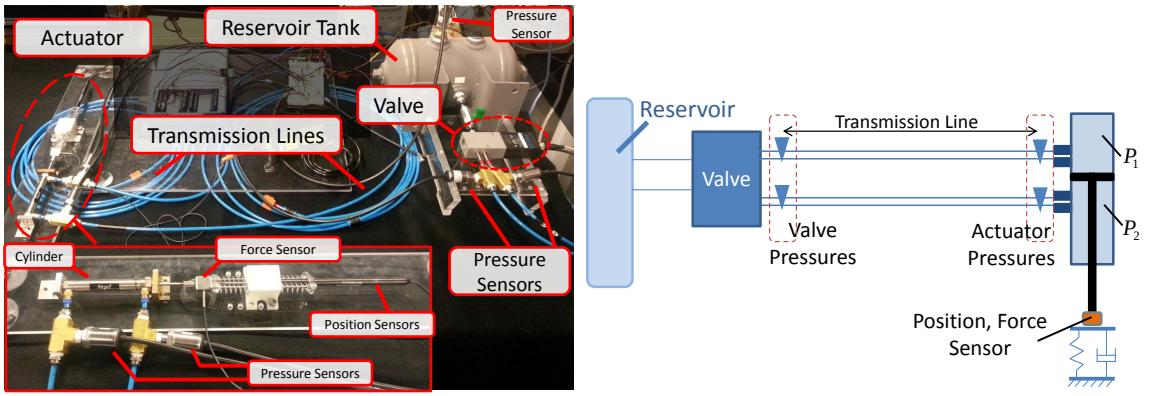


(a) (b)

Figure 14: (a) Photo of the experimental setup. (b) Schematics showing the components on the experimental setup.

the procedure outlined in the literature [35]. The variation of $C_{A_{v_i}}$ with regard to the valve input is given in Appendix A. The particular valve used in this study is under lapped, meaning that flow in either direction occurs around the mid-position of the spool. The calibration tests showed that the conductance of the valve within that range is significantly small (less than 1.3% of the capacity, as shown in Figure 54). Therefore, the bi-directional flow in the mid-range was regarded as leakage and neglected. Steady-state reservoir pressures when the spool is in that range were measured and utilized as the upstream pressure of the valve, in order to avoid a steady-state bias in the estimations. The rest of the model parameters, including the geometrical properties of the actuator were obtained from its datasheet.

Two major types of force controller were chosen to evaluate the performance of the proposed observer in the course of interactive robot manipulation tasks. Direct force controlling and impedance controlling experiments were implemented on the pneumatic system, as illustrated in Figure 15. The proposed observer was also implemented. Note that the output of the observer was not utilized for any of the force controller to simplify the evaluation by decoupling the force controller and observer. The direct force control was used to track 1 Hz and 2 Hz of sinusoidal desired force

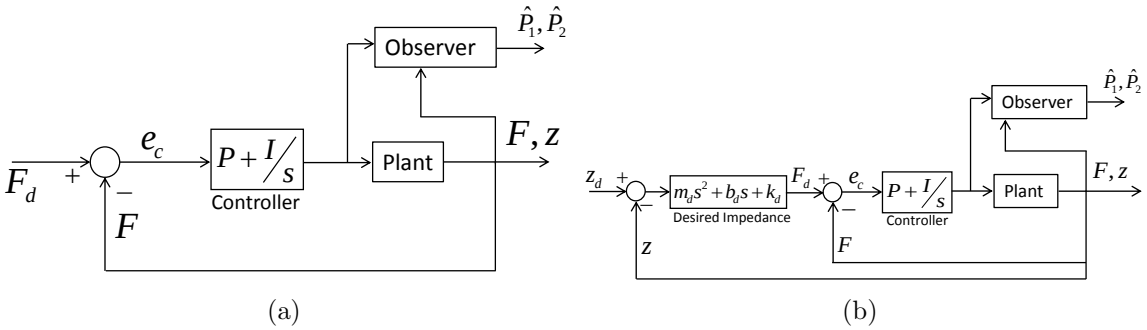


Figure 15: Control algorithms used in the observer evaluation (a) Direct force control with a sinusoidal reference force (b) Impedance control

profiles where a PI controller was chosen and tuned. Whereas, the impedance controller was used to realize a desired impedance shown in (42). A reference position, $z_d$, was given as a neutral position of a mass-spring-damper in the desired impedance. Based on the difference between the reference and actual positions, the desired force, $F_d$, was calculated as follows:

$$\tilde{z} = z_d - z \tag{41}$$

$$F_d = m_d \ddot{\tilde{z}} + b_d \dot{\tilde{z}} + k_d \tilde{z} \tag{42}$$

Finally, $e_c$ defined as below and is fed to the controller in both types:

$$e_c = F_d - F_e \tag{43}$$

In our experiments, the impedance parameters $m_d$,$b_d$, and $k_d$ were chosen for a critically damped response. The reference position, $z_d$, was defined by a square wave function. The magnitude of the feedback gain, $k$, was adjusted to yield a fast error convergence without inducing any chatters on the impedance control tests with the step reference signal. All controller gains including the impedance parameters can be found in Appendix B. The controller output was added to the value of the valve excitation that keeps the spool in the mid-position. Comparisons were made between the proposed observer and the following two conventional approaches:

**Valve pressure measurements:** On a typical system with no transmission line, chamber pressures are measured at the valve ports. In this study, the pressure

readings at the ports of the valve are evaluated to see how well they can represent the chamber pressures when there are transmission lines in the system, as illustrated in Figure 14. On certain applications, valve ports can be the only available location for measuring pressure states, e.g. tele-operations in MRI.

**Standard system model with no force measurement:** The details of a standard pneumatic system model is given in section III. On an isothermal actuator, this model provides a stable pressure estimation with regard to errors without requiring any force or acceleration feedback from the actuator [24]. In this study, the actuator chambers are assumed isothermal considering the frequency of the valve excitation [47], [34], [1].

### 4.2.4 Results

Errors in the estimation of chamber pressures are illustrated using phase diagrams. The performance of the proposed observer is compared to both the standard system model and valve pressures. The theoretical valley with a time-invariant slope, explained in Figure 12, is represented with a dashed line for reference. In each experiment, the reference for the controller was chosen to be cycloid, and each phase plot involves at least 10 cycles in each figure. Estimation performances are evaluated quantitatively by the averaged sum of squared errors (MSE) within one cycle in the steady-state condition as follows:

$$\text{MSE} = \frac{1}{2}\frac{\int_0^T \boldsymbol{e}^T \boldsymbol{e} \mathrm{d}t}{T} \tag{44}$$

Figure 16 presents the errors in the chamber pressure estimations as well as the integrated sum of errors per cycle for the force tracking experiment with 1 Hz desired force. The amplitude of the desired force is chosen as 24 N, considering the max force capacity of the given pneumatic circuit. The initial values of estimated pressures were set to zero for both the model and the proposed observer.

Figures 17 and 18 show the same comparisons as Figure 16, for force tracking

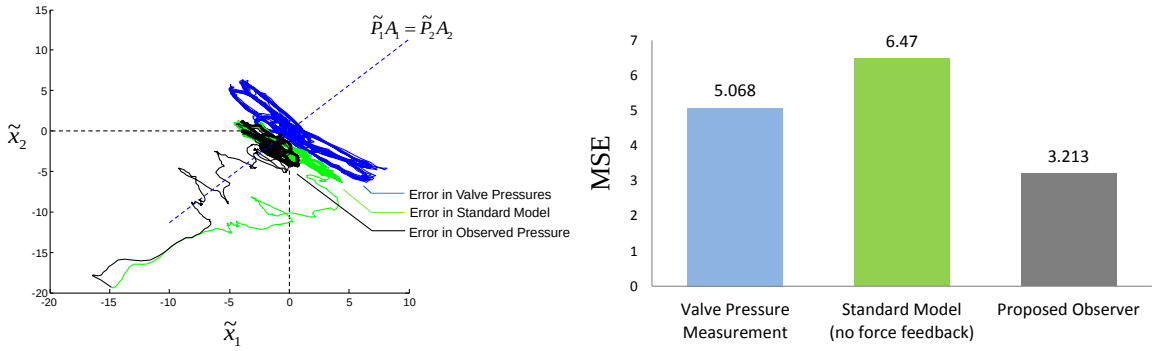


(a) (b)

Figure 16: Pressure estimation errors on the 1 Hz force control experiment. (a) Phase diagram that shows estimation errors $\tilde{x_1}$ and $\tilde{x_2}$. (b) The averaged sum of squared errors (MSE) within one stable cycle.

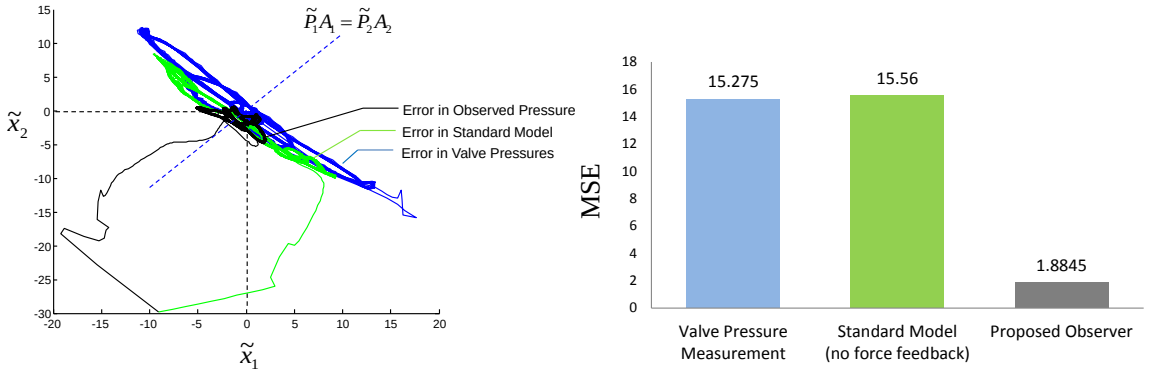


(a) (b)

Figure 17: Pressure estimation errors on the 2 Hz force control experiment. (a) Phase diagram that shows estimation errors $\tilde{x_1}$ and $\tilde{x_2}$. (b) The averaged sum of squared errors (MSE) within one stable cycle.

with 2 Hz desired force and square wave impedance force tracking respectively. The performance of the controller on each experiment is given in Appendix B.

Since the impedance controlling experiment involves a steady-state period in each cycle during which the actuator pressures are stationary, a close look at the transient phase of the experiment is given separately in Figure 19. The measured and estimated pressures are shown in time domain.

Efficiency of the correction term in estimating the measured actuator force is illustrated in Fig 20. Both the estimated and measured actuator force, $\hat{F}_p$ and $F_p$

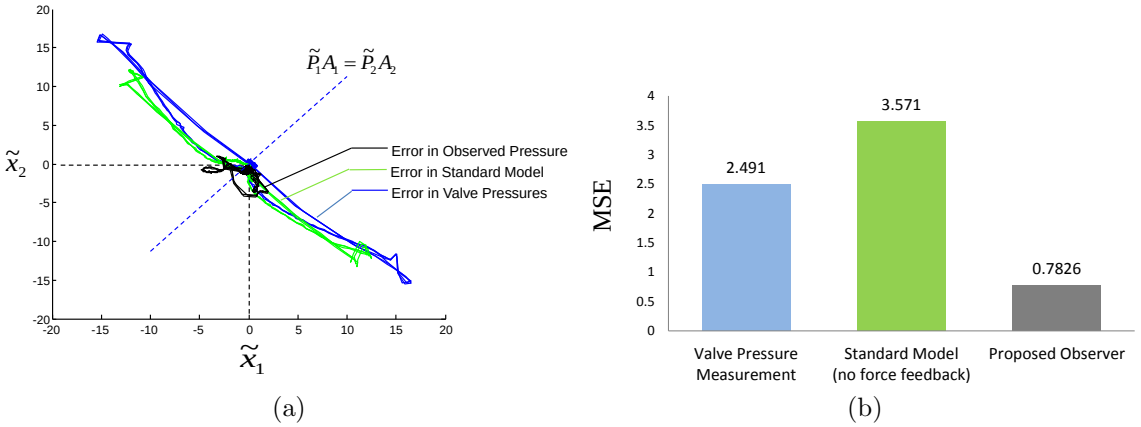


(a) (b)

Figure 18: Pressure estimation errors on the impedance control experiment. (a) Phase diagram that shows estimation errors $\tilde{x_1}$ and $\tilde{x_2}$. (b) The averaged sum of squared errors (MSE) within one stable cycle.

respectively, and the difference between them are presented.

The measurement errors and uncertainty in the calibrated load dynamics of the piston affect the precision of the measured actuator force. Figure 21 presents a comparison of the measured actuator force, $F_p$, with the true value of the actuator force, $F_p^*$, that is realized by substituting measured true actuator pressures into (17). The plots in both Figure 20 and Figure 21 belong to 1 Hz and 2 Hz force controlling experiments.

### 4.2.5 Discussion

The error phase diagrams shown in Figure 16, 17 and 18 indicate a significant improvement in the estimation accuracy by the use of the proposed observer. The estimation error of the standard system model can be explained by the uncertainty in the flow parameters that define the mass flow rate and the inhomogeneity of the pressure along the transmission lines. The standard model assumes the homogeneous pressure distribution beyond the valve in contrast to the pressure gradient due to friction. For similar reasons, the pressure measurements at the valve suffer a significant distortion comparable to that of the standard model estimations. These two

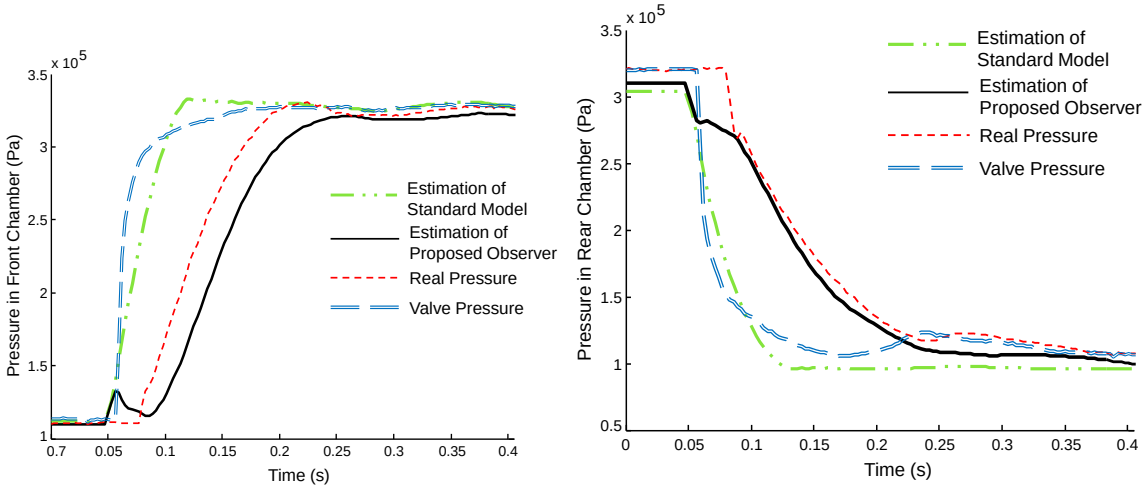


(a) (b)

Figure 19: Pressure signals measured at the valve and actuator ports in addition to the estimated actuator pressures obtained using the conventional model and the proposed observer, during impedance force tracking (a) Pressure in the rear chamber (b) Pressure in the front chamber

approaches present a more severe deviation at a higher frequency, causing larger oscillations in error shown in Figure 17. This can be attributed to the increasing phase with respect to true actuator pressures, and the mass flow attenuation that occurs more sharply at higher frequencies [38],[2]. On the other hand, pressure observation based on force sensing appears to be beneficial and effective in reducing estimation errors. The improvement mainly stems from the correction term that suppresses the oscillation around the valley, as was elaborated in Figure 12. The ultimate convergence of errors to origin is determined by the accuracy of the modeling part of the observer, which depends on the valve calibration and the valve input range for a given task.

The proposed observer based on force sensing achieves a quick response and substantially reduces the estimation errors in the transient phase. This improvement can be observed in Figure 19 where the transient pressure fluctuations during the impedance controlling experiment are shown. The time delay and attenuation in the mass flow rate introduced by transmission lines are not captured by the standard

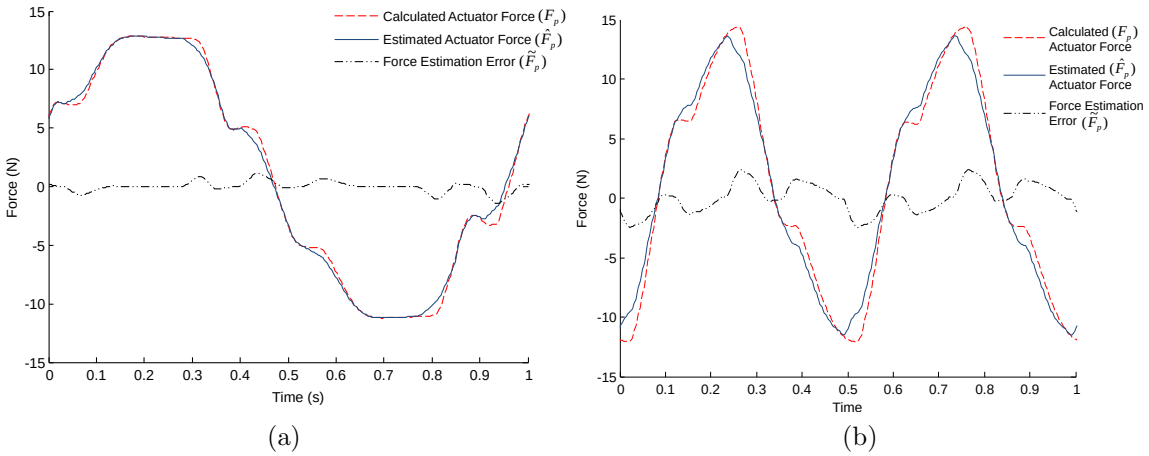


(a) (b)

Figure 20: Estimated actuator force using the proposed observer and the estimation error. (a) 1 Hz force control (b) 2 Hz force control

model. On the other hand, the proposed feedback term improves the estimation accuracy, establishing a relation between the estimated and measured actuator force. A steady-state error is observed in both the model and observer estimations as opposed to the valve pressure measurements. This deviation may be resultant from a bias in the valve model due to the air leakage at small valve openings.

The proposed correction algorithm for pressure estimation achieved a satisfactory precision in minimizing the mismatch between the estimated and measured actuator forces, $\hat{F}_p$ and $F_p$ respectively. Figure 20 shows the efficiency of the correction in estimating the calculated force. The observer gain, $k$, was kept constant in this study; yet, it can be adjusted for even faster convergence, when needed to compensate for rapid changes at higher frequencies.

The experiments indicated that the proposed algorithm can tolerate a bounded uncertainty in the calculation of the actuator force. Neglected friction, filtered signals and numerical differentiations result in a bounded variation in the difference between the measured and true actuator force, represented as $\delta$ in (37), shown in Figure 21. The substantial improvement in the pressure estimation accuracy despite such experimental errors confirms the robustness of the correction algorithm of the proposed

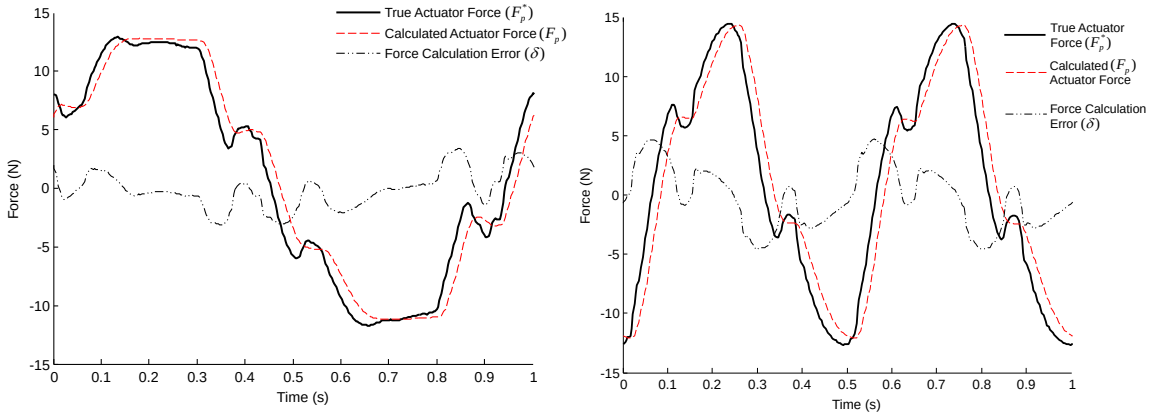


Figure 21: Actuator force calculated using the force and displacement sensors vs. obtained using true chamber pressures. (a) 1 Hz force control (b) 2 Hz force control

observer.

The proposed method is experimentally shown to provide accurate pressure estimations of a complex pneumatic system that would otherwise require advanced and customized system modeling. Open-loop estimation via detailed modeling often lacks assuring stability in pressure observation, and requires empirical parameters for characterizing customized hardware. The proposed observer involves a standard system model and utilizes force sensing for error correction. Admittedly, the proposed observer requires a force sensor in addition to a displacement sensor which is commonly used in the closed-loop control of pneumatic actuators. The same correction algorithm can still be used without a force sensor, if there is no external force on the piston, i.e. the piston is in free motion. In this paper, the friction across the actuator piston was assumed to be negligibly small. For applications where the piston friction is significant, a friction model added to the actuator force calculation would be necessary to improve the precision of pressure estimation.

The standard pressure estimation methods present a lower accuracy; as the hardware involves more significant unmodeled dynamics, e.g. longer transmission lines, especially at higher frequencies [38]. Theoretically, the correction algorithm always

serves to attenuate the estimation errors; yet, the magnitude of its contribution depends on the operation. This study aims to provide experimental validation of the described method at typical reference frequencies as well as the mathematical proof of its contribution. It should be noted that the correction term presented in this paper can be used with different models, provided that those models are stable.

The proposed observer is most useful when the system hardware involves unmodeled dynamics. As demonstrated in this chapter, tele-operated systems are very suitable for the described method. Pneumatically driven robots designed to function in MRI often include long transmission lines that would introduce a significant uncertainty in pressure estimation [83], [89]. Force measurements have recently become available in MRI with the use of plastic optical sensors [81],[54]. Position measurement is relatively easy to achieve as MRI-compatible optical encoders are commercially available. Consequently, the proposed method can benefit from the development of new sensors.

## 4.3 Sliding Mode Control with the Proposed Observer

Obtaining accurate information on the pressure states of a tele-operated system is difficult for structural reasons. Direct pressure reading in MRI via pressure sensors is not available, due to the strict material limitations for MR compatibility. Open-loop estimation also yields limited accuracy. Pressure attenuation and time-delay introduced by long transmission lines make it difficult to apply conventional models for pressure estimation and control [13]. In addition, such models unfortunately cannot fully characterize additional hardware-specific complex dynamics such as frictional losses or leakage in the equipment [38] For MRI compatibility, glass cylinders with carbon pistons are being used. In addition to low magnetic susceptibility, glass cylinders can achieve low friction, yet the gas leakage through their ports are not negligible.

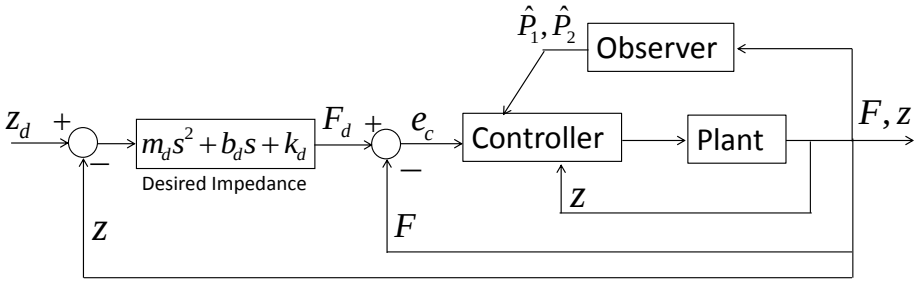


Figure 22: The block diagram of the developed impedance controller

In this section, the developed pressure observer is tested with a sliding-mode impedance controller and its performance is compared to the conventional pressure estimation method outlined in the previous sections. The contribution of the proposed observation method in the pressure estimation accuracy was elaborated in this chapter. This section presents the impact of the method to the control performance with a standard model-based controller.

### 4.3.1 CONTROLLER

The aim of the control algorithm is to make the contact force $F_e$, exerted by the environment, reflect a desired impedance behavior in 42. For this study, a critically damped impedance characteristic is selected as the reference.

A sliding-mode based controller is utilized to satisfy the desired contact force. The sliding surface is selected as:

$$s = e + \lambda \int e \quad dt \tag{45}$$

where $e = F_d - F_e$.

The design of the control law that provides the desired output motion, represented by $s = 0$, is well-defined and widely applied on the control of pneumatic actuators [66]. Therefore, the derivation of the valve input will be briefly described here and proofs for the controller stability are omitted.

The error dynamics is stabilized by choosing a Lyapunov candidate, $V = \frac{1}{2}s^2$ and setting its time derivative as a negative definite function, or $s\dot{s} < 0$. This relation is

satisfied by calculating an equivalent valve input that correspond to $\dot{s} = 0$ according to the valve model and adding a robustness term. Based on the definition of the sliding surface, $s$, its derivative can be represented as:

$$\dot{s} = \dot{F}_d - \dot{F} + \lambda(F_d - F) \tag{46}$$

The value of the sonic conductance, $C_{A_v}$, that will set the derivative of $s$ to the targeted value can be calculated substituting (14)-(18):

$$C_{A_{v_{eq}}} = \frac{\dot{F}_d + M\dddot{z} + B\ddot{z} + \frac{\hat{P}_1\dot{V}_1A_1}{V_1} - \frac{\hat{P}_2\dot{V}_2A_2}{V_2}}{\text{sign}(A_{v_{eq}})RT(\psi(P_u, \hat{P}_1)\frac{A_1}{V_1} + \psi(P_u, \hat{P}_2)\frac{A_2}{V_2})} \tag{47}$$

Then the equivalent valve input value, $A_{eq}$, that correspond to the calculated sonic conductance is solved utilizing the calibration of the valve. Note that the observed pressure states are substituted for the derivation of the equivalent input. The resultant input value, including the robustness term becomes:

$$\dot{A}_v = A_{v_{eq}} - \eta sat(\frac{s}{\phi}) \tag{48}$$

where $\eta$ is strictly positive to ensure error convergence to zero. To avoid chatter around the equilibrium, the robustness term involves a saturation function of $s$ over a boundary layer value of $\phi$ [66].

### 4.3.2 EXPERIMENTAL SETUP

A double acting cylinder (Airpel E9.0DU) was connected to a four-way spool valve (Enfield Tech. LH05) via 7.25 m. long transmission lines of 4 mm inside diameter. The actuator pressures were measured by analog pressure sensors (SSI Technologies P51 series) at the cylinder ports. The pressure measured at the inlet of each actuator chamber was regarded as true pressure in the corresponding chamber. The external force applied to the actuator was measured by a load cell (FUTEK LSB200) attached at the tip of the piston rod. The piston was placed in front of a spring system that provided an unknown external force upon interaction, as shown in Figure 23. The piston

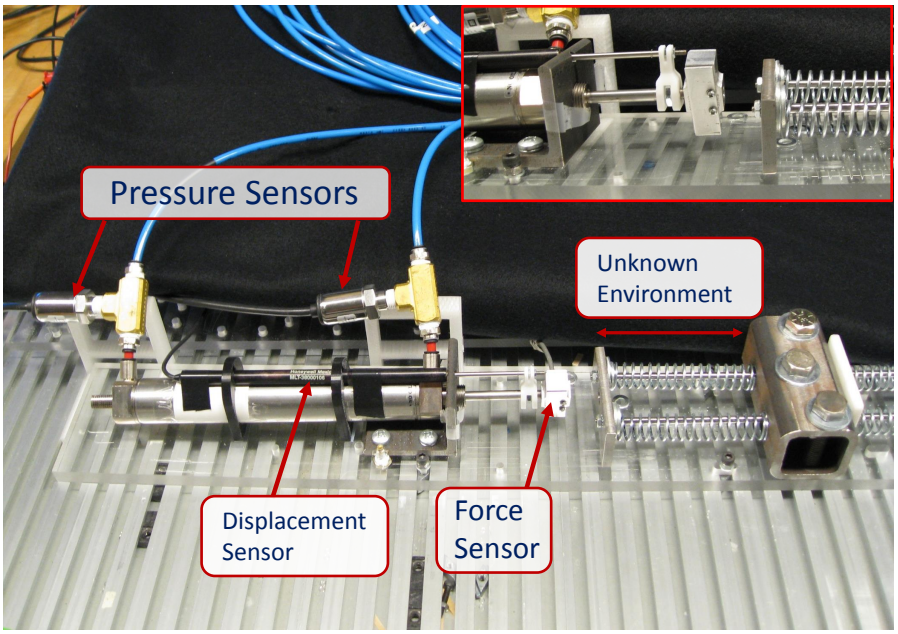


Figure 23: The photo of the experimental setup used for the observer-based control tests

position was measured by using a Honeywell linear potentiometer (model F38000106). The velocity and acceleration of the piston are obtained by numerical differentiation with a first-order filter at 50 Hz. The system was controlled by a platform of Intel i7 @2.80GHz processor with 6.00 GB RAM, where the control algorithm, shown in Figure 22, were implemented using Labview. The National Instruments A/D board (NI USB-6221) was used for data acquisition.

### 4.3.3 RESULTS

The performance of the observer-based impedance controller is shown in Figure 24-25. Figure 24 presents the desired and measured interaction force values, $F_{ed}$ and $F_e$ respectively, when the desired position of the piston, $z_d$, was changed to different fixed locations. The response of the proposed system was also tested under a periodically varying desired position.

The contribution of the described pressure observation was analyzed by comparing the control performance of the system with the one that utilizes open-loop pressure

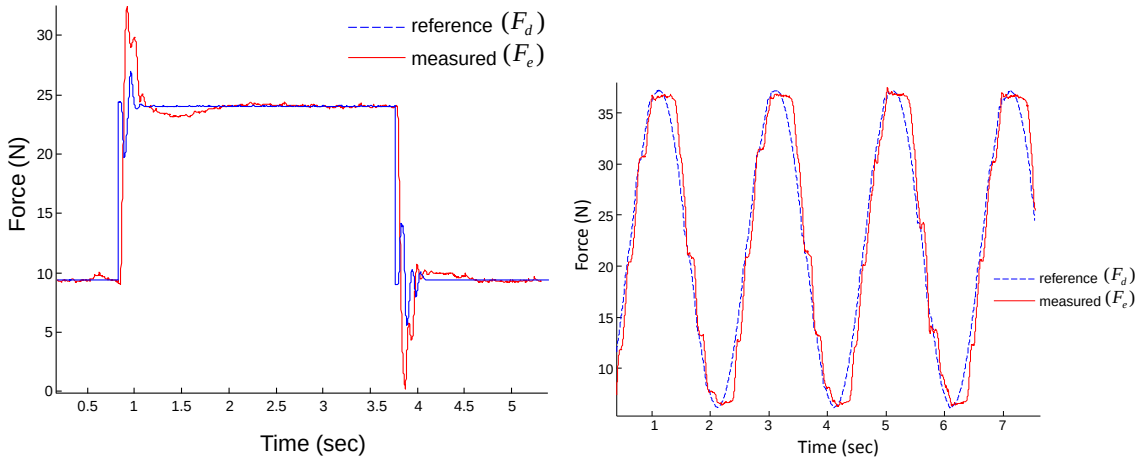


(a) (b)

Figure 24: The desired and measured piston forces. The response of the system for a) a step change in the reference position. b) 0.5 Hz sinusoidal reference position.

estimation, i.e. standard system modeling. The tests with sinusoidal desired position were selected for this comparison. The control and observation accuracy are evaluated quantitatively by the averaged sum of squared errors (MSE) within one cycle in the steady-state condition, given in (44). For the evaluation of control performances the error vector has one element, the error in the interaction force. Whereas for evaluating the pressure observation accuracy, the following error vector is selected: $\boldsymbol{e} = [(P_1 - \tilde{P}_1) \quad (P_2 - \tilde{P}_2)]^T$.

The data shown in Figure 26 corresponds to MSE in six steady-state cycles for each estimation type, open-loop and closed-loop, and each experiment. Figure 26.a presents the mean and the variation of MSE in force. Figure 26.b shows the average MSE in pressure estimation.

Figure 27 shows the transition in the system response when the described closed-loop observer was turned on. The MSE in force for each cycle during the 0.5 Hz sinusoidal reference position test is presented in Figure 27.a. The MSE in pressure estimation on the same test is provided in Figure 27.b.

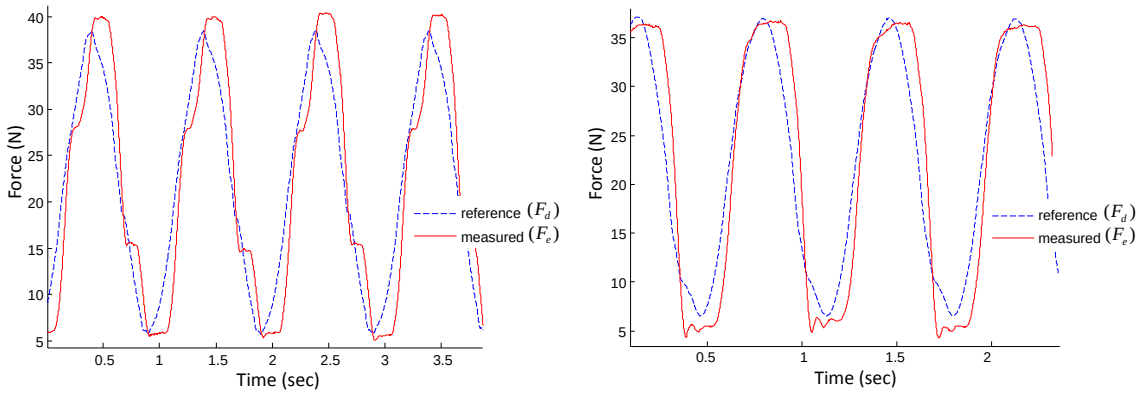


Figure 25: The desired and measured piston forces. The response of the system for a) 1 Hz sinusoidal reference position. b) for 1.5 Hz sinusoidal reference position.

### 4.3.4 DISCUSSION

This work has presented the use of a new pressure observer on the control of tele-operated pneumatic systems. The observed pressures were utilized in an impedance controller to achieve an accurate force tracking on a pneumatic actuator with 7.25 meters long transmission lines.

The developed control scheme provided a interaction force tracking against an unknown environment. The system presented a time-delay issue with a rising magnitude as the reference variation frequency increases. This study was limited to 1.5 Hz, as the contact stability was not preserved beyond. These limitations can be attributed to the significantly long transmission lines. A fixed mass transportation delay and an attenuation in the mass flow rate through the lines reduce the bandwidth of the actuation.

Figures 26 and 27 illustrate the benefit of the described observer both in pressure estimation and the control performance. The improvement in control accuracy is more significant at higher frequencies -%25 on the 1.5 Hz force tracking experiment- where the demand for the valve flow is greater. Pressure states are involved in the equivalent valve input; hence, they are more effective when the magnitude of the ideal flow rate

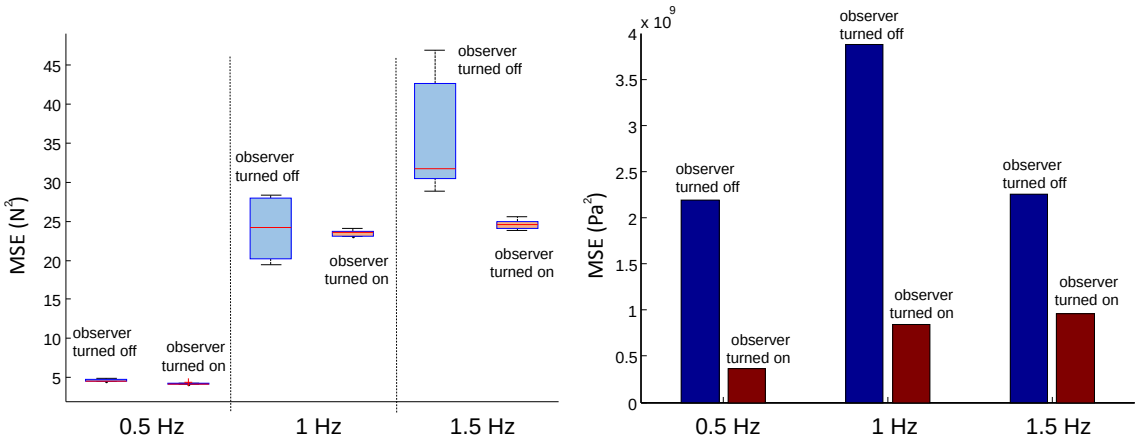


(a) (b)

Figure 26: Mean squared error (MSE) for the sinusoidal reference position tests (a)in output force (b) in pressure estimation

is higher. On the other hand, the improvement in the pressure estimation may not follow the same trend. The described observer substantially reduced the pressure estimation errors in this study. Yet, the magnitude of the improvement depends on the quality of the valve calibration within the given interval of valve inputs for a specific operation. The advantage of utilizing the observer can also be viewed by the rate of error convergences, shown in Figure 27. A rapid improvement in the pressure estimation initiates a downward slope in the force error when the observation is tur

## 4.4 Conclusion

A pressure observer based on force sensing for pneumatically driven actuators has been developed and tested. The observer takes advantage of force measurement of the load dynamics when the pressure dynamics of the system cannot be accurately characterized by the pneumatic system model. The proof of the observer being globally Lyapunov-stable is given. The proposed approach achieves asymptotic stability to pressure estimation under a widely-used controller constraint. Also, the robustness against measurement errors was provided. The efficiency of the observer has been demonstrated in a series of experiments on force control of a tele-operated pneumatic

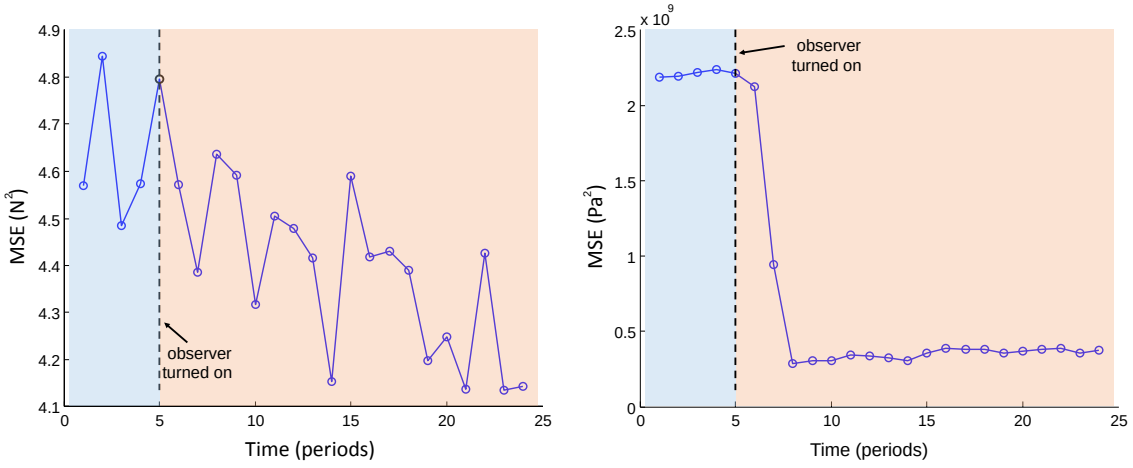


(a) (b)

Figure 27: Mean squared error (MSE) for 0.5 Hz sinusoidal reference position (a)in output force (b) in pressure estimation

system with long transmission lines. The results indicated significant reduction in estimation error compared to the conventional pneumatic system model and pressure measurement at the transmission line distant from the actuator. The proposed observer can achieve high accuracy in complex pneumatic systems without requiring an advanced model of pressure dynamics. The established pressure observation approach fits very well to pneumatic medical robots designed to operate in MR rooms, since direct pressure measurement is not available and the pressure dynamics of such systems present complexity due to compressible flow. A benchmark study on a medical application is planned and will be reported as future work. This study presented a pressure observer based impedance controller for pneumatic systems with long transmission lines. The adverse effects of the transmission lines in pressure estimation and the lack of direct pressure feedback from the actuator are compensated by the described observer. The experiments on a system with 7.25 meters long transmission lines indicated that the use of the observer improves the accuracy of the force tracking as well. This study can be extended by analyzing the range of impedance characteristics that can be provided by the tested system. The motivation for the developed algorithm

comes from the potential of pneumatically driven systems for robotic rehabilitation in MRI. The described algorithm will be applied on an MRI-compatible haptic interface with long transmission lines in the future.

## 4.5 Summary

This chapter presented a force-feedback based pressure observation method that is capable of providing accurate pressure estimations despite the complex dynamics introduced by the transmission lines. The developed method is experimentally shown to provide accurate pressure estimations of a complex pneumatic system that would otherwise require advanced and customized system modelling. The provided feedback method effectively improves the accuracy of the standard pneumatic system model, particularly at higher frequencies. It does not require a transmission line model and guarantees bounded stability in the presence of disturbance in force measurements, hence it is able to provide a robust pressure estimation. The effectiveness of the proposed observer is confirmed by performing force control experiments in a tele-operated pneumatic system. The use of the proposed observation method is not limited to the tele-operated systems. Any pneumatic actuation setup with unmodeled dynamics would be a suitable application for the introduced feedback method.

Pressures of a pneumatic actuator are commonly used to improve control performance. The contribution of the proposed observation method on the control accuracy was also experimentally validated. Implemented in a standard model-based control method for impedance control, the proposed observation method achieved a higher accuracy in the output compared to the conventional pressure estimation method. Although, the proposed observation improved the control of tele-operated pneumatic actuation; the improvement was not significant. A novel control method that accounts for the line dynamics was considered to be necessary. The next chapter presents a new approach on the control methodology for a more enhanced control performance.

# CHAPTER V

# FORCE CONTROLLER DESIGN BASED ON TRANSMISSION LINE MODEL

Recent trends in the use of tele-operated pneumatically driven systems necessitate advanced approaches for mitigating the adverse effects of those connecting lines on the system dynamics. Standard pneumatic modeling, which assumes the line as a dead volume, or linearizing the flow equations have been satisfactory for low-bandwidth (¡1 Hz) position control of tele-operated systems [90], [14]. However, more accurate modeling tools are needed for relatively faster operations such as haptic interfaces, rehabilitation robots and exoskeletons, in which force or impedance control is objected.

Long transmission lines have been characterized by a number of complex methods, yet only a very few of them was suitable for online control applications. Detailed numerical simulation models are too complicated to be implemented in non-linear controllers and they often involve hardware specific parameters that limit the use of such methods [85], [42]. Krichel et al. presented an average friction model on a segmented profile that is feasible for online control applications [38]. Their study suggested the use of numerical time-domain models over modeling in frequency domain with a finite order transfer function. The average-friction model has potential to improve the control performance in tele-operation, when combined with non-linear control methods that are proven to be effective on pneumatic systems.

This chapter proposes a cascaded architecture for the control of tele-operated pneumatic actuators. The developed multi-layer controller accounts for the non-linear pressure dynamics in the line, unlike standardized methods. In the first layer,

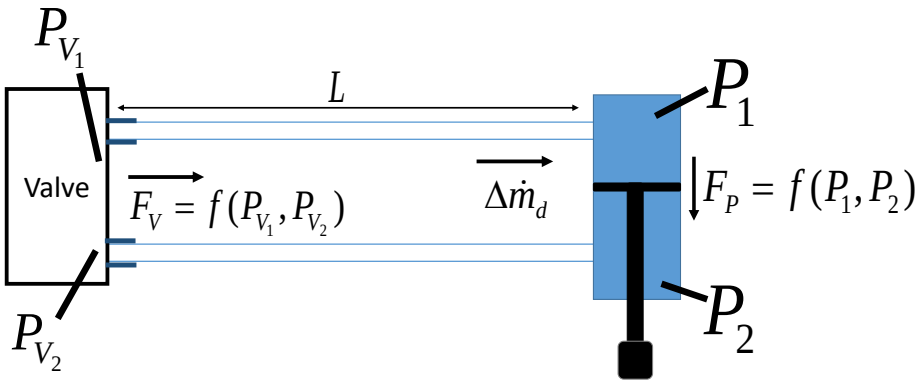


Figure 28: The intended idea in the developed model based control algorithm

a line model is utilized to design a virtual input that brings the system to the desired state. The second layer provides a closed-loop controller for tracking the designed virtual input. Figure 28 illustrates the key elements of the proposed approach. A virtual input, valve force ($F_v$), was defined as a function of pressures at the valve ports. Its relation to the actuator force, $F_p$, and the desired mass flow rate towards the actuator, $\delta\dot{m}_d$, were characterized by a low-order version of the averaged friction model described by Krichel et al. [38]. In this work, the performance of the proposed method is compared to that of a sliding-mode controller with the standard system model. The comparisons were made on different line lengths at various reference signal frequency.

## 5.1 Standard Sliding-Mode Controller for Force Control on Pneumatic Actuators

A typical sliding-mode force control for pneumatic actuators is implemented by defining a sliding surface based on the error in the output force. Let $e = F_d - F_e$, where $F_d$ is the desired force and the $F_e$ is the environmental force as described in Figure 11. Choosing a Lyapunov function:

$$L = \frac{1}{2}s^2 \tag{49}$$

with the sliding surface:

$$s = e + \lambda \int e dt \tag{50}$$

The control input, $u$, that assures $\dot{L} = s\dot{s} \leq 0$ can be derived by substituting (18) and (14):

$$u = \frac{\dot{F}_d + M\dddot{z} + B\ddot{z} + \lambda e + ksat(s)}{\psi_T} \tag{51}$$

where

$$sat(s) = \begin{cases} \frac{s}{\phi}, & \text{if } s \leq \phi \\ 1, & \text{if } s > \phi \end{cases} \tag{52}$$

and

$$\psi_T = \psi(P_u, P_{d_1})A_1 + \psi(P_u, P_{d_2})A_2 \tag{53}$$

with $\phi$ being a given boundary thickness for smoothing the input as the sliding mode converges to equilibrium [66]. The control input, $u$, that corresponds to the net sonic conductance of the valve can be obtained by calibrating the valve, as shown in Appendix A.

## 5.2 Line Modeling in Time Domain

The tele-operated pneumatic system model developed in this study follows the same logic as the distributed pipeline models decribed in [38]. The transmission line is discretized in its longitudinal axis and the governing equations are implemented on each of the elements with averaged parameter values. Figure 29 presents the elements for each dynamic relation adopted in our method. In this work, the line is assumed to be comprised of two control volumes with one associated mass flow rate in between. Therefore, the flow rate dynamics is defined between two local pressures: the valve pressure, $P_v$, and the actuator pressure, $P_c$. The first half of the line volume is associated with the valve pressure, whereas The other half and the actuator chamber volume are combined for the actuator chamber pressure. The following equations are

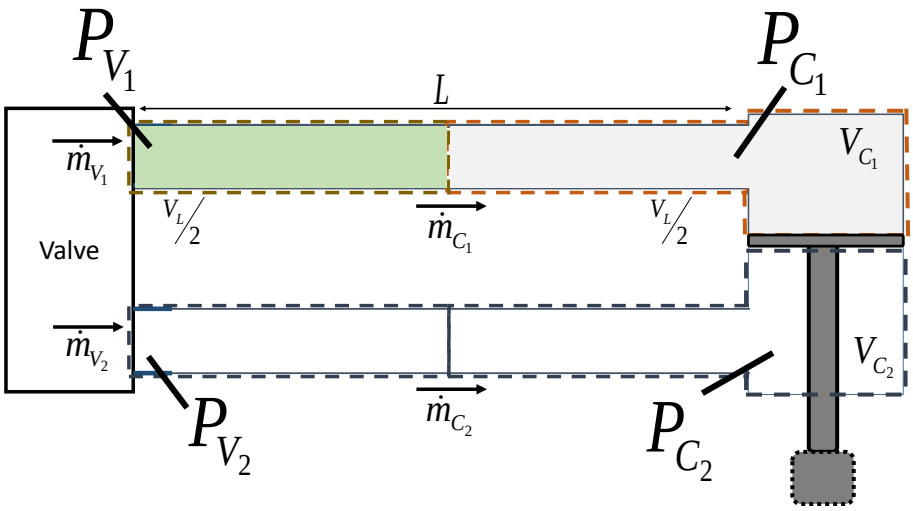


Figure 29: The line schema

formulated to represent the flow and pressure dynamics of the system:

$$\frac{d\dot{m}_{c_i}}{dt} = (P_{v_i} - P_{c_i})\frac{A}{L} - f_{(\dot{m}_{c_i}, P_{v_i}, P_{c_i})}\dot{m}_{c_i} \tag{54}$$

$$\dot{P}_{c_i} = \frac{\dot{m}_{c_i}RT - P_{c_i}\dot{V}_{c_i}}{V_{c_i} + V_L/2} \tag{55}$$

$$\dot{P}_{v_i} = \frac{(\dot{m}_{v_i} - \dot{m}_{c_i})RT}{V_L/2} \tag{56}$$

where $L$ is the line length and $A$ is the line cross-section area that defines the volume of the line: $V_L = AL$. Each of the two sides of the pneumatic system, shown in Figure 29, is denoted by $i = 1, 2$. The volume of the actuator chamber, $V_{c_i}$ is added to half of the line volume, $V_L$, to define the volume associated with $P_{c_i}$. The rate of mass flow through the valve, $\dot{m}_{v_i}$, is a function of the pressures across the valve and the area of the valve opening. The details on the calculation of $\dot{m}_{v_i}$ is given in Appendix A.

This method assumes an average friction, $f$, for the whole line. $f$, is approximated as the following continuous function of the mass flow $\dot{m}_{c_i}$ and the pressures $P_{v_i}, P_{c_i}$:

$$f(\dot{m}_{c_i}, P_{v_i}, P_{c_i}) = \frac{32\mu}{D^2}\frac{1}{\rho_i} + 0.158\frac{\mathrm{Re}_i^{3/4}\mu}{D^2}\frac{1}{\rho_i} \tag{57}$$

where $\mu$ is the dynamic viscosity of air, $D$ is the tube diameter, $\rho_i$ is the density of the air and $\mathrm{Re}_i$ is the Reynolds number calculated using the mass flow rate. This friction

definition accounts for the change in flow regime. The density, $\rho_i$, is calculated by averaging the boundary pressures at the line:

$$\rho_i = \frac{P_{v_i} + P_{c_i}}{2RT} \tag{58}$$

where $R$ is the thermodynamic constant, $T$ is the room temperature.

Note that the position of the piston; hence, the chamber volumes are calculated and substituted at each time step to obtain the pressure values. The valve pressure is also considered to be available by the use of pressure sensors at the valve ports. The pressure in the actuator chamber is then obtained assuming an isothermal chamber model. The state-space model for pressure and flow rate estimation, therefore, becomes:

$$x = \begin{bmatrix} P_{c_1}V_1 \\ \dot{m}_{c_1} \\ P_{c_2}V_2 \\ \dot{m}_{c_2} \end{bmatrix} \quad , \quad \dot{x} = \begin{bmatrix} \dot{m}_{c_1}RT \\ (P_{v_1} - P_{c_1})\frac{A}{L} - f_{(\dot{m}_{c_1}, P_{v_1}, P_{c_1})} \\ \dot{m}_{c_2}RT \\ (P_{v_2} - P_{c_2})\frac{A}{L} - f_{(\dot{m}_{c_2}, P_{v_2}, P_{c_2})} \end{bmatrix} \tag{59}$$

### 5.2.1 Passivity of the Line Model

The non-negative friction coefficient in 54 provides a passive mapping from the valve pressure, $P_{v_i}$, to the mass flow rate $\dot{m}_{c_i}$. Indeed, the stability of the described system for any input valve pressure could be shown when the rate of change in the actuator volume is sufficiently low. In our study, the targeted force control bandwidth is limited to 2 Hz, which results in a considerably slow piston motion.

**Theorem 1:** The mapping from the valve pressure, $P_{v_i}$, to the mass flow rate, $\dot{m}_{c_i}$, described in 59 is passive when the rate of change in the actuator volume is sufficiently low.

**The proof of theorem 1:** By selecting the mass flow rate, $\dot{m}_c$, as the output

and the valve pressure as the input, let:

$$E = \frac{1}{2}\dot{m}_c^2 + \frac{1}{2}P_c^2 V_c \frac{A}{LRT} \tag{60}$$

represent the energy developed in the system. The derivative of $E$ can be described in the following way, substituting 54 and 55:

$$\dot{E} = \dot{m}_c P_v - f_{(\dot{m}_c, P_c)}\dot{m}_c^2 + \delta_{(\dot{V}_c, P_c)} \tag{61}$$

where $\delta_{(\dot{V}_c, P_c)} = -\frac{A}{2LRT}P_c^2\dot{V}_c$ is the perturbation due to the variation in the chamber volume. The perturbation is assumed to be bounded, such as $|\delta_{(\dot{V}_c, P_c)}| < \beta$, where $\beta$ is a positive constant. Since the friction function, $f$, is always positive for a non-zero mass flow rate; the described mapping is passive when:

$$f_{(\dot{m}_c, P_c)}\dot{m}_c^2 > \beta \tag{62}$$

which holds true for sufficiently low rates of change in the chamber volume.

This system can be utilized to estimate the chamber pressures and the mass flow, $\dot{m}_c$, from the measured valve pressure. In addition, a desired valve pressure based on a targeted mass flow rate can be obtained. The next section introduces the algorithm that would ensure a robust force control on tele-operated pneumatic actuators, based on the system described here.

## 5.3 Controller Design

### 5.3.1 Simplifications

A few simplifications have been made on the described line model for the ease of controller implementation and to allow force control with a four-way spool valve. These valves operate on two valve outlets with one electronic input. A discussion on the use of the proposed control idea on different valves is given in section VII.

The rate of pressure change in each actuator chamber can be described by substituting the flow rate in 54 to 55:

$$\dot{P}_{1,2} = (P_{V_{1,2}} - P_{1,2})\frac{A}{L}h_{1,2} - P_{1,2}\frac{\dot{V}_{C_{1,2}}}{V_{C_{1,2}}} - \ddot{m}_{1,2}h_{1,2} \tag{63}$$

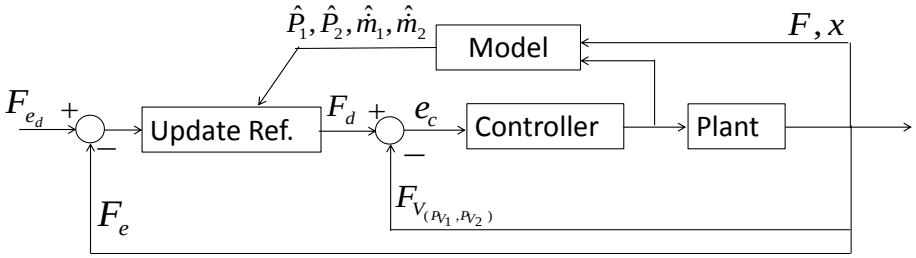


Figure 30: The block diagram for the developed force control algorithm

where

$$h_{1,2} = \frac{RT}{f_{1,2} V_{C_{1,2}}} \tag{64}$$

The rate of change in the mass flow rate is neglected and the coefficients $h_{1,2}$ are unified by averaging the side-specific parameters in each side as follows:

$$\bar{h} = \frac{RT}{\bar{f}\bar{V}}, \ \textit{where } \bar{f} = \frac{f_1 + f_2}{2} \ \textit{and } \bar{V_C} = \frac{V_{C_1} + V_{C_2}}{2} \tag{65}$$

With these simplifications, the rate of change in the piston force, $F_p$, given in 17 becomes:

$$\dot{F}_p = F_V \bar{h} - F_p \bar{h} - (P_1 \frac{\dot{V}_{C_2}}{V_{C_2}} A_1 - P_2 \frac{\dot{V}_{C_2}}{V_{C_2}} A_2) \tag{66}$$

where,

$$F_V = f_{(P_{v_1}, P_{v_2})} = P_{V_1} A_1 - P_{V_2} A_2 \tag{67}$$

$F_V$, which is shown in Figure 28, is referred as valve force in this manuscript.

This simplified relation between the valve force, $F_V$, and the time derivative of the piston force, $\dot{F}_p$, has been utilized in a cascaded line model-based controller, shown in Figure 30. The valve pressures and the chamber volumes are measured, whereas the tube friction and chamber pressures are obtained using the original line model described in section III.

### 5.3.2 Design of the Controller

Consider the system below, which is obtained based on the simplified line model:

$$\begin{aligned} \dot{F}_e &= F_V\bar{h} - F_p\bar{h} - G_1 + \delta_1(x) \\ \dot{F}_V &= \frac{\psi_T u - (\dot{m}_{c_1}A_1 + \dot{m}_{c_2}A_2)}{V_l/2} + \delta_2(x) \end{aligned} \tag{68}$$

where

$$G_1 = (M\dddot{z} + B\ddot{z}) + (P_1\frac{\dot{V}_{C_2}}{V_{C_2}}A_1 - P_2\frac{\dot{V}_{C_2}}{V_{C_2}}A_2) \tag{69}$$

$\delta_1(x)$ and $\delta_2(x)$ are perturbation functions that are assumed to be bounded and Lipschitz: $\delta_1(x) < \beta_1|x|$ and $\delta_2(x) < \beta_2|x|$. The substitution $\dot{m}_v = \psi_T u$ has been made in (68) to represent the control input, $u$, in the system equations. The control input is multiplied with a flow function, $\psi_T$, that is defined in (53).

In the first step, a virtual input of valve force is defined:

$$F_{v_d} = F_p + \frac{\lambda e + \dot{F_{e_d}} + G_1}{\bar{h}} + k_{p_1}e_1 + k_{i_1}w_1 \tag{70}$$

where $e_1 = F_{e_d} - F_e$, $\lambda_1$ is a positive constant and $w_1 = \int e_1 dt$, with positive constants $k_{p_1}, k_{i_1}$ that yield:

$$\dot{e}_1 = -k_{p_1}e_1 - k_{i_1}\int e_1 dt + \delta_1 \tag{71}$$

where $e_2 = F_{v_d} - F_v$. The next step is to select the control input for tracking $F_{v_d}$. Let,

$$u = \frac{(\dot{F_{v_d}} + k_{p_2}e_2 + k_{i_2}w_2)V_l/2 + (\dot{m}_{c_1}A_1 + \dot{m}_{c_2}A_2)}{\psi_T} \tag{72}$$

where $w_2 = \int e_2 dt$ and $k_{p_2}, k_{i_2}$ are positive constants that yield:

$$\dot{e}_2 = -k_{p_2}e_2 - k_{i_2}\int e_2 dt + \delta_2 \tag{73}$$

**Theorem 2:** The control input, $u$, described in 72 satisfies a stable force control against the errors in the output force, $e_1$, and the virtual input, $e_2$.

**The proof of theorem 2:** The stability of this multi-layer control algorithm can be analyzed by choosing the following Lyapunov candidate:

$$L = \frac{1}{2}(e_1^2 + e_2^2 + (k_{i_1}w_1)^2 + (k_{i_2}w_2)^2) \tag{74}$$

The derivative of the Lyapunov candidate, $L$, can be obtained substituting (71) and (73):

$$\dot{L} = -\bar{h}k_{p_1}e_1^2 + \bar{h}e_2e_1 + \delta_1e_1 - k_{p_2}e_2^2 + \delta_2e_2 \tag{75}$$

Using Young's inequality [67], $ab \leq \frac{\epsilon}{2}a^2 + \frac{1}{2\epsilon}b^2$, the derivative of $L$ can be shown as:

$$\dot{L} \leq e_1^2(\bar{h}(-k_{p_1} + \frac{\bar{h}}{2\epsilon_1}) + \frac{1}{2\epsilon_2}) + e_2^2(-k_{p_2} + \frac{\epsilon_1}{2} + \frac{\epsilon_3}{2}) + \frac{\epsilon_2}{2}\delta_1^2 + \frac{1}{2\epsilon_3}\delta_2^2 \tag{76}$$

where

$$\begin{aligned} e_1e_2 &\leq e_1^2\frac{\bar{h}^2}{2\epsilon_1} + e_2^2\frac{\epsilon_1}{2} \\ e_1\delta_1 &\leq e_1^2\frac{1}{2\epsilon_2} + \delta_1^2\frac{\epsilon_2}{2} \\ e_2\delta_2 &\leq e_2^2\frac{\epsilon_3}{2} + \delta_2^2\frac{1}{2\epsilon_3} \end{aligned} \tag{77}$$

and $\epsilon_1$, $\epsilon_2$, $\epsilon_3$ are positive constants. Since $\bar{h}$ is always positive, the stability of $L$ is satisfied if $k_1$ and $k_2$ are chosen, satisfying:

$$\begin{aligned} k_{p_1} &> \frac{\bar{h}}{2\epsilon_1} + \frac{1}{2\bar{h}\epsilon_3} \\ k_{p_2} &> \frac{\epsilon_1}{2} + \frac{\epsilon_3}{2} \end{aligned} \tag{78}$$

The robustness gains in both (71) and (73) act as simple P.I. Continuous saturation functions with finite boundaries can be designed as shown in [[74]], if needed. The derivatives of the position measurement and the desired virtual input, $F_{V_d}$, can be approximated using numerical derivations with digital filters.

## 5.4 Experiments

### 5.4.1 Experimental Setup

A double acting cylinder (Airpel E2.0DU) was connected to a four-way spool valve (Enfield Tech LH-05) via long transmission lines of 4 mm inside diameter. Pressure was measured by analog pressure sensors (SSI Technologies P51 series) at the four locations shown in Figure 31: at the inlet of each actuator chamber and at each exit port of the spool valve. The pressure measured at the inlet of each actuator chamber

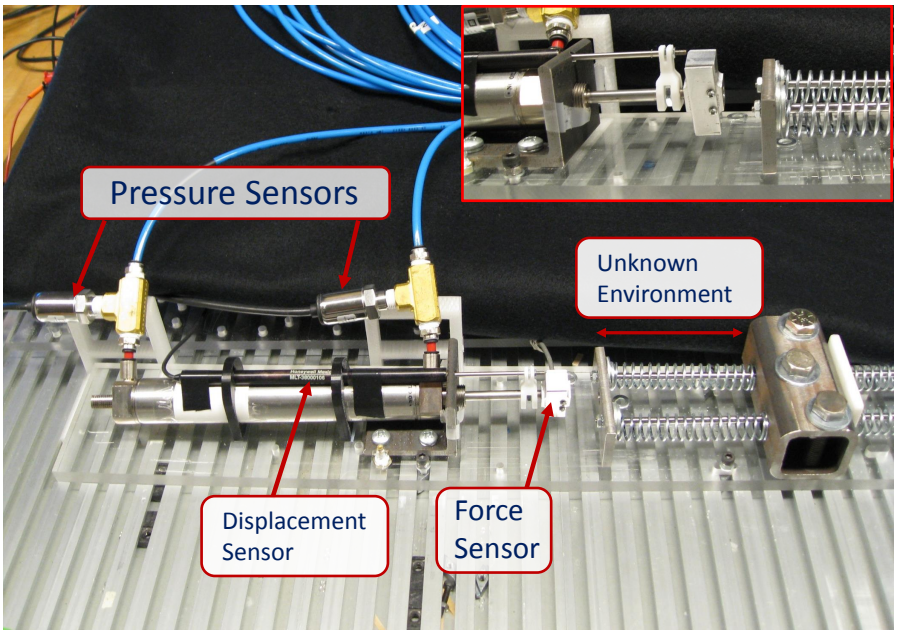


Figure 31: The photo of the experimental setup for the developed force controller

was regarded as true pressure in the corresponding chamber. The external force applied to the actuator was measured by a load cell (Omegadyn LC703-50) attached at the tip of the piston rod. The piston was connected to a spring system that provided an external force proportional to the piston displacement, as shown in Figure 31. The piston position was measured by using a Honeywell linear potentiometer (model F38000106). The velocity and acceleration of the piston are obtained by numerical differentiation with a first-order filter at 50 Hz. The system was controlled by a platform of Intel i7 @2.80GHz processor with 8.00 GB RAM, where the control algorithm were implemented using Labview. The National Instruments A/D board (NI DAQ-6221) was used for data acquisition.

### 5.4.2 Procedure

The proposed method was compared to the standard sliding-mode based force controller, described in section II. The performance of each method was tested on four different force reference types: step, 0.5 Hz, 1 Hz, and 2 Hz signals; on four different setups with the following transmission line lengths: 2, 5, 7.25, and 10 meters. The

Table 4: Mean Squared Error in the Output Force Control ($MSE_1$) and the Virtual Input Tracking ($MSE_2$)

| Line length (m) | 0.5Hz Reference $MSE_1/MSE_2$ | 1Hz Reference $MSE_1/MSE_2$ | 2Hz Reference $MSE_1/MSE_2$ |
|---|---|---|---|
| 2 | 6.38 / 4.33 | 9.28 / 5.68 | 17.63 / 8.16 |
| 5 | 1.23 / 3.66 | 2.63 / 5.89 | 6.44 / 8.22 |
| 7.25 | 1.6 / 4 | 3.36 / 5.52 | 12.83 / 7.97 |
| 10 | 2.44 / 6.33 | 7.08 / 8.85 | 22.85 / 10.37 |

comparison in the accuracy of each method was based on the mean of error squares obtained in a 2-second time interval.

The controller gains in each method were tuned to yield similar settling time and damping ratio on a step change in the reference force. The same set of gains were utilized for all other reference types on a given transmission line-length. For the proposed method, the inner closed-loop gains were adjusted first, and held fixed for all setup types.

## 5.5 Results

The accuracy in the force control of each method was compared in Figure 32. The mean of the squared control error, $MSE_1$, was selected as a measure for the controller accuracy. The diagrams in Figure 32 refer to 0.5 Hz, 1 Hz and 2 Hz reference signals.

The proposed method achieves the desired force output by tracking the desired virtual input. Figures 33 and 34 show the performance in virtual input and the desired output force tracking on the setup with 5 meter long transmission line. The accuracy in tracking the desired virtual input is quantified by the mean of the squared tracking error, $MSE_2$. A quantitative comparison for each experiment in this study is given on Table I. The accuracy in the actuator pressure estimation based on the valve pressure measurements via the described line model was also analyzed. Figures

35 and 36 present the pressure estimation performance on two different settings: 10-meters long tele-operation setup with 2 Hz reference and 2-meters long setup with 0.5 hz reference signal respectively. The mean squared errors in pressure estimations were obtained utilizing the measured actuator chamber pressures. The estimation errors were generally increasing with the added length of transmission line. Figure 37 provides a comparison on the accuracy level of each method at various transmission line lengths with 2 Hz reference signal.

## 5.6 Discussion

This study aims to adapt an accurate line modeling technique to the model-based control of tele-operated pneumatic systems. Standard pneumatic system models with widely applied sliding-model controllers neglect the line dynamics which has been previously shown to be very significant on tele-operation [82]. The comparative analysis presented in this work indicates the need for an advanced approach to account for the effects of the lines.

In general, the contribution of the proposed method is more significant as the transmission length and the reference frequency increase. However, the experiments indicate that the described method pays off only when the line length is 5 meters or longer, as shown in Figure 32. With a short connection tube length, the efficiency of the feedback gain $k_1$ drops; since, the parameter $\bar{h}$ is greater. The rate of convergence in $e_1$ is affected by the magnitude of $\bar{h}$, as can be seen in 78. Furthermore, the weight of the line volume on the mass-flow dynamics decrease, making the standard SMC more accurate compared to the proposed method at 2-meter long transmission. The standard SMC presents a severe reduction in the accuracy as the line length increases. Only for the 2-meter transmission setup with 0.5 Hz reference, its accuracy is exceptionally low. At that configuration, the performance of both controllers were affected by the uncertainty in the valve calibration that is more significant on small

valve opening ranges. A small volume setup with low actuation frequency generally results in a small operation range, resulting in calibration-related mismatches that can be seen in Figure 36.a.

The desired virtual input, $F_{V_d}$, represents the target force profile at the inlet of the transmission lines. As shown in Figure 33 and 34, that new target force signal appears to be slightly shifted to the left in time, and upward in magnitude. This emergent negative phase shift is the reason for an improved force control. The proposed method compensates for the dynamic delay due to the lines, matching the actuator force, $F_p$, with the desired output force, $F_d$. The upward shift in magnitude compensates the static difference between the actuator force, $F_p$, and the environmental force, $F_e$, which is $P_{atm}A_p$ in (18). That static difference can be seen in Figure 33.a as well.

The tracking accuracy of the inner closed-loop, $MSE_2$, stays almost fixed for a given reference signal across different line lengths. Except at 10 meters of transmission, where the error in each closed-loop $MSE_1$ and $MSE_2$ are relatively higher. Still, the reduction in the accuracy of the proposed method from 5 meters to 10 meters is very small compared to that of the standard method. Table I shows a similar trend for the control accuracy with different reference frequencies on a given transmission length. Pressure estimation accuracy of the described line model that is based on the valve pressures dramatically surpasses the standard model as seen in Figure 37. The success of the described line model in actuator pressure estimation is also a very important factor on the overall performance of the proposed method.

The force control experiments in this work indicated the suitability of the described line model-based control method for tele-operated, pneumatically driven robotic applications. The method is more effective on the 5-10 meters long transmission range, which is the typical length of connection in magnetic resonance imaging (MRI) compatible robotic devices [90], [93], [40]. Yu et al. has compared hydraulic and pneumatic actuation with regard to their use in tele-operation. They reported that the

moderate bandwidth of the pneumatic actuation is a major advantage over hydraulics [92]. The proposed method was shown to be effective in that bandwidth, maintaining its advantage in the control accuracy as the reference signal frequency rise. Another interesting application would be the pneumatically actuated exoskeletons or humanoids. Transmission lines are needed for non-collocated system components to achieve a desirable weight distribution. In such applications, the connection tubes are relatively short. But they are smaller in diameter either [63]. Therefore, they can affect the flow dynamics.

The control method described in this manuscript involved simplifications for its use on four-way spool valves with single input. The introduced idea can be utilized for individual pressure control by the use of separate valves without the need for any simplifications. Such hardware implementations have been suggested for force and stiffness control in previous works [94], [62], [74]. The inner closed-loop was designed to make the flow-controlled spool valve act as a pressure-controlled servo. Following the idea introduced here, a Lyapunov-based integrator backstepping controller can be designed on the same setup.

## 5.7 Conclusion

Compressible flow through pneumatic transmission lines complicate the control of tele-operated pneumatic actuators and reduce the accuracy of conventional control methods. In this chapter, a method to adapt numerical line modeling to model-based controllers was proposed and experimentally validated. The performance of the described method was compared to a sliding-mode controller with a standardized system model. The experiments showed a significant improvement in the force control accuracy for systems with 5-10 meters long transmission lines between the actuator and the drivers.

The introduced method utilizes a non-linear line model to compensate for the line

dynamics. It has a potential to improve the performance of tele-operated systems; such as MRI-compatible medical devices, or pneumatically actuated humanoids. This chapter provided an experimental proof for the efficiency of the introduced method on tele-operation tasks, leaving the potential applications as future work.

## 5.8 Summary

Recent trends towards the use of pneumatic actuation for tele-operation requires long transmission lines between the actuator and the drivers. Pneumatic systems with non-co-located system components started to appear in medical robots designed for operations in magnetic resonance (MR) rooms, mobile tele-operated transportation robots, or pneumatically actuated humanoids. The transmission lines affect the system dynamics significantly, complicating the control of actuators. Conventional control methods utilize standardized system models that present large errors in characterizing the pressure dynamics of tele-operated actuators. This chapter introduces a novel control method that adapts an accurate non-linear line model to non-linear controllers. The line model is utilized to calculate a virtual input to be tracked by a flow controlled valve. The experiments validated the contribution of the proposed method in the force control accuracy for systems that involve 5 to 10 meter long transmission lines. The introduced method achieved up to 75% reduction in the error compared to a standard sliding-mode based force control at reference frequencies between 0.5 Hz to 2 Hz.

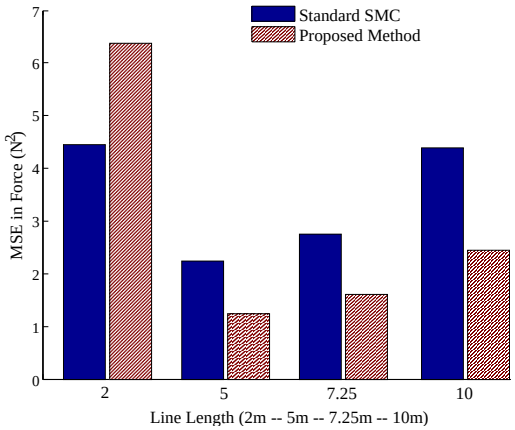


(a)

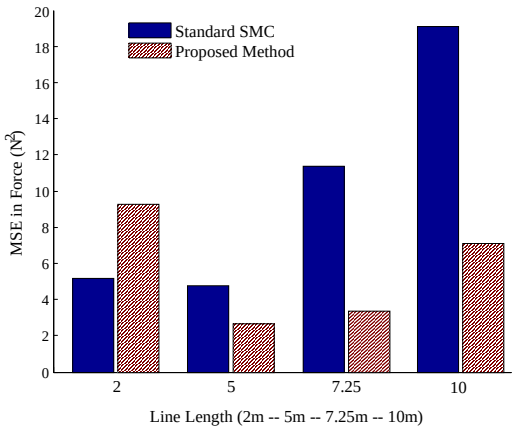


(b)

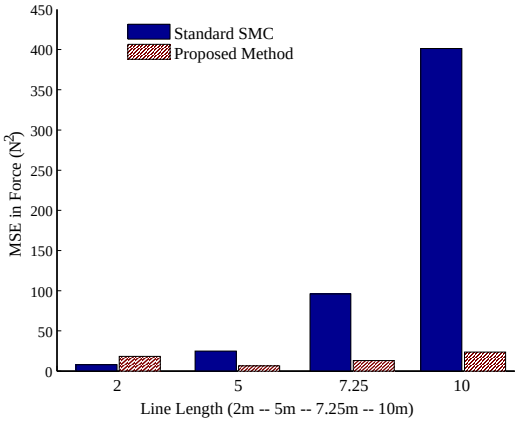


(c)

Figure 32: The accuracy in the force control of both the standard SMC and the proposed method, obtained on setups with different transmission lengths. a) Mean squared control error ($MSE_1$) at 0.5 Hz reference signal b) $MSE_1$ at 1 Hz reference signal c) $MSE_1$ at 2 Hz reference signal

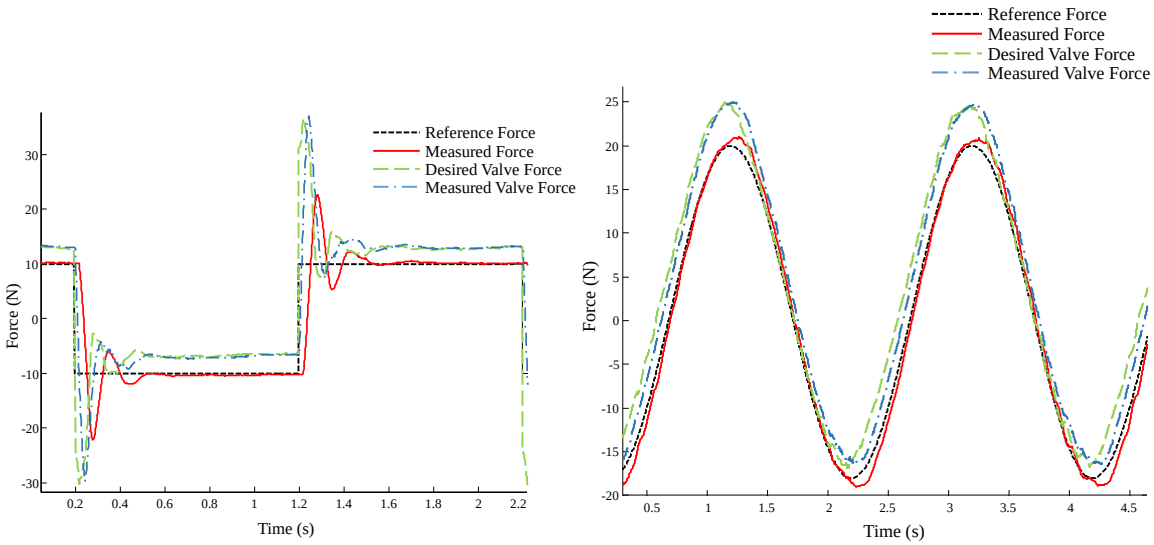


Figure 33: Virtual input tracking as well as output force control performance of the proposed method at the setup with 5 meters long transmission. When a) The desired force is a step signal. b) The desired force is a 0.5 Hz sinusoidal.

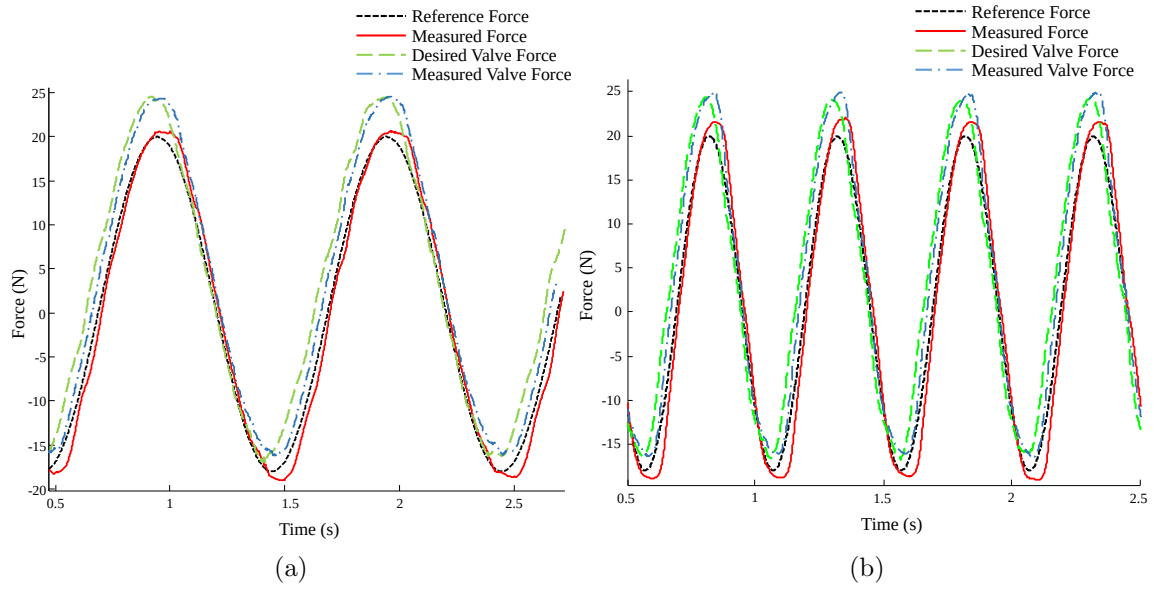


Figure 34: Virtual input tracking as well as output force control performance of the proposed method at the setup with 5 meters long transmission. When a) The desired force is 1 Hz sinusoidal. b) The desired force is a 2 Hz sinusoidal.

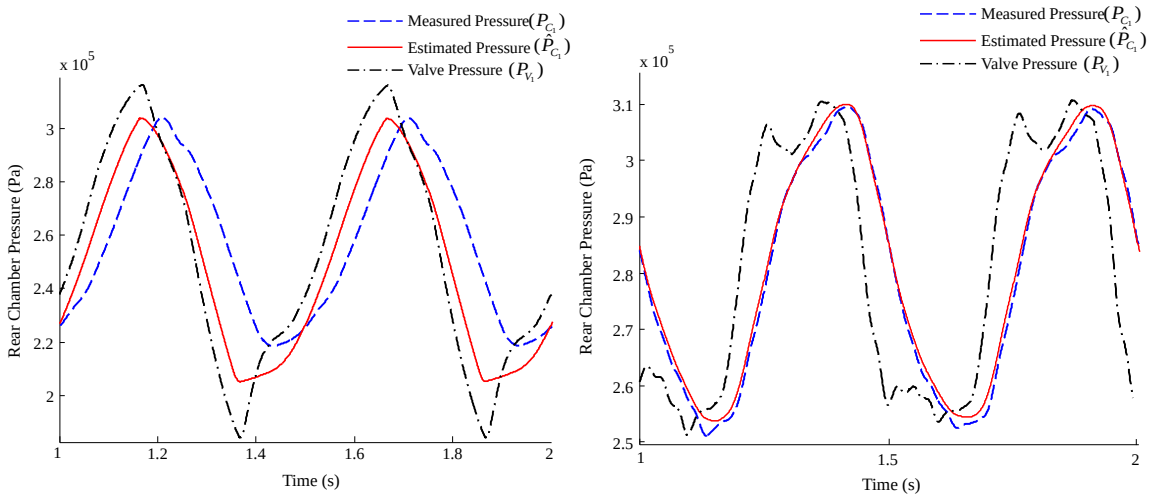


Figure 35: Measured and estimated actuator pressures for the setup with 10 meters long transmission at 2 Hz force reference. a) Standard system modeling. b) The proposed system modeling.

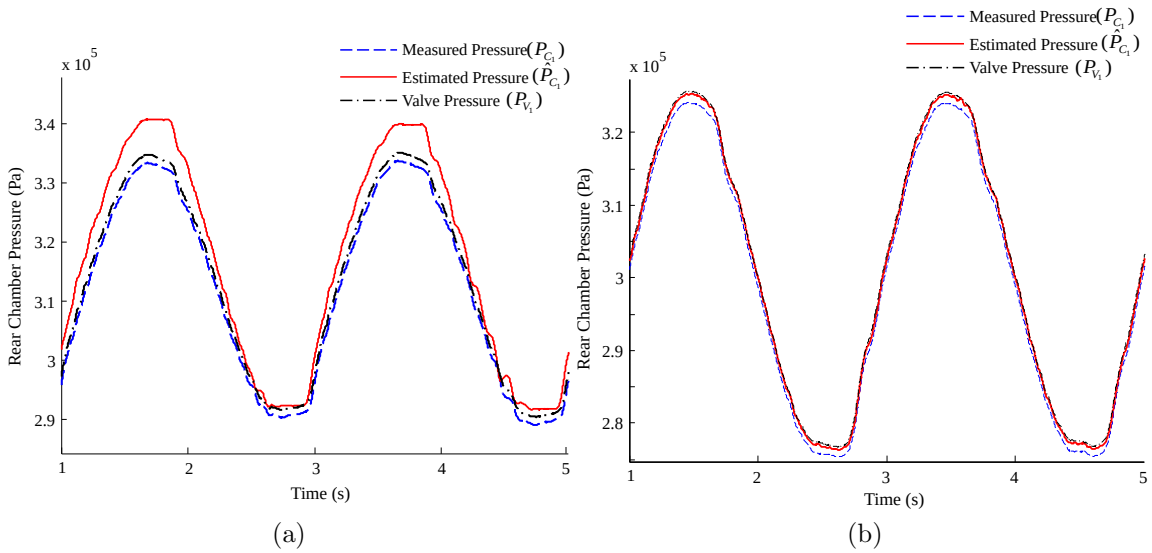


Figure 36: Measured and estimated actuator pressures for the setup with 2 meters long transmission at 0.5 Hz force reference. a) Standard system modeling. b) The proposed system modeling.

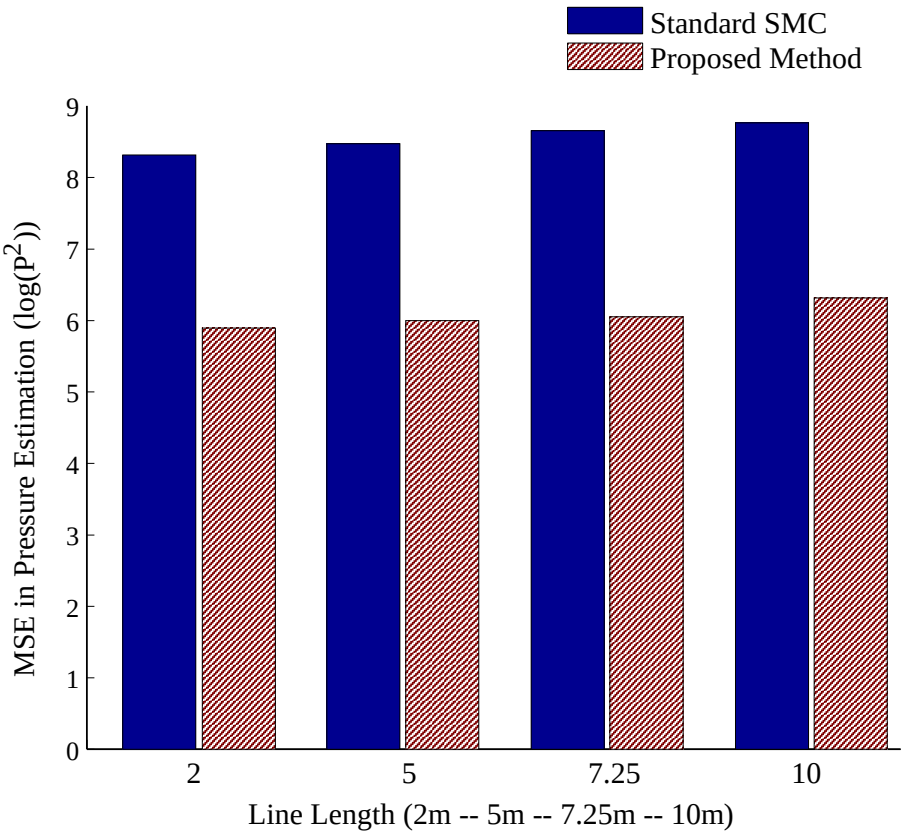


Figure 37: The mean squared error (MSE) in actuator chamber pressure estimation. The standard pneumatic modeling, is compared to the proposed line model on various transmission lengths with 2 Hz reference signal.

# CHAPTER VI

# A MRI COMPATIBLE OPTICAL FORCE SENSOR

This chapter will present a compact, 1-axis fiber optic force sensing unit that can be easily extended to multi-axis designs. Design of the 1-axis sensing unit and its suitability for an extension to multi-axis sensing are primarily discussed. Since the volume inside MRI chamber is tight, a compact sensor body is aimed. The sensing principle of the proposed design is chosen to minimize the cable traffic and input handle. A genuine displacement amplification compliant mechanism is designed to increase the sensitivity in the axial direction exclusively and reduce hysteresis.

The displacement amplification mechanism is designed to reduce the total strain energy deployed on the sensor body, which would alleviate the hysteresis problem of the plastic sensors. In this chapter, the developed sensor body is analyzed for higher accuracy and amplification performance. MRI compatibility and mechanical performance of this sensing unit under axial and lateral loading are tested.

## 6.1 Design and Fabrication

### 6.1.1 Sensing Principle

The proposed sensing principle is shown in Figure 38. A mirror and a fiber optic cable are assembled on a deformable structure. As in almost every force sensors, an applied force deforms the structure moving the mirror with respect to the fiber optic cable. A genuine compliant mechanism is designed to amplify the displacement of the mirror in axial direction. As the gap between the fiber tip and mirror changes, the intensity of reflected light varies. The reflected light is transmitted via the same fiber optic cable through a fiber optic circuit. The circuit involves 2 photodiodes, a light source and a bi-directional fiber optic coupler. Figure 3 shows a simplified schema

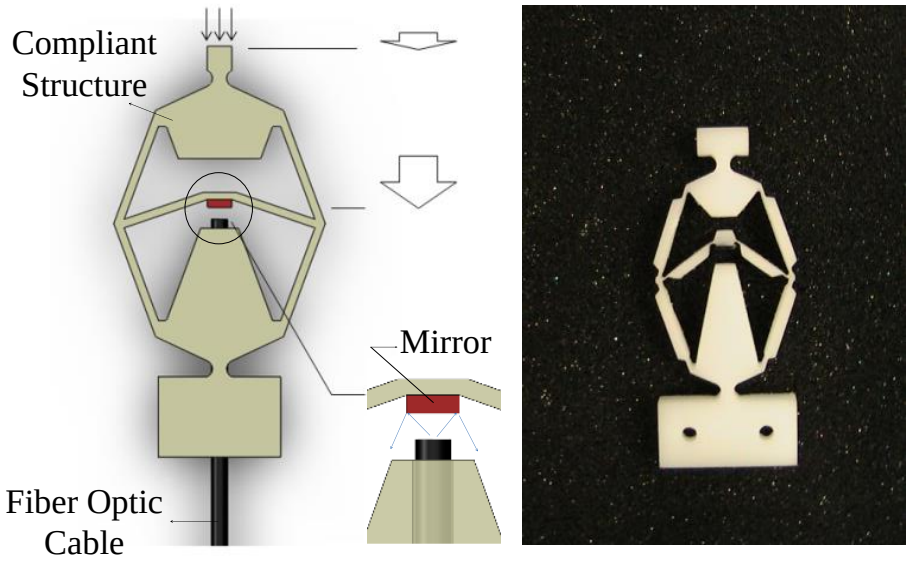


Figure 38: Deformable structure of the proposed sensor

of the circuit which was examined by Lazeroms et al. [41] Fiber to mirror assembly offers an easy and compact way to sense the deflection in the body. The variation in the output voltage and the distance between mirror-fiber couple is illustrated in Appendix. To have a linear variation with high sensitivity, 0.1-1.50 mm interval is chosen for the assembly.

### 6.1.2 Structure

A deformable structure is developed to transduce the force into displacement. To have a good resolution the displacement should be high and overall stiffness of the body should be low. Also, an ideal 1-axis sensor is only sensitive in one direction. Considering these facts, a new displacement amplification compliant mechanism (DACM) is designed for sensing purposes. In order to optimize the initial design idea, significant geometric parameters of the structure is derived by a trivial kinematic analysis. Then the performance of the design is optimized by playing with those parameters using finite element analysis software. Due to elastic deformation in the body, kinematic models do not represent the structure but may reveal the effective parameters. In order to avoid energy absorption by unwanted internal elastic deformations, the top

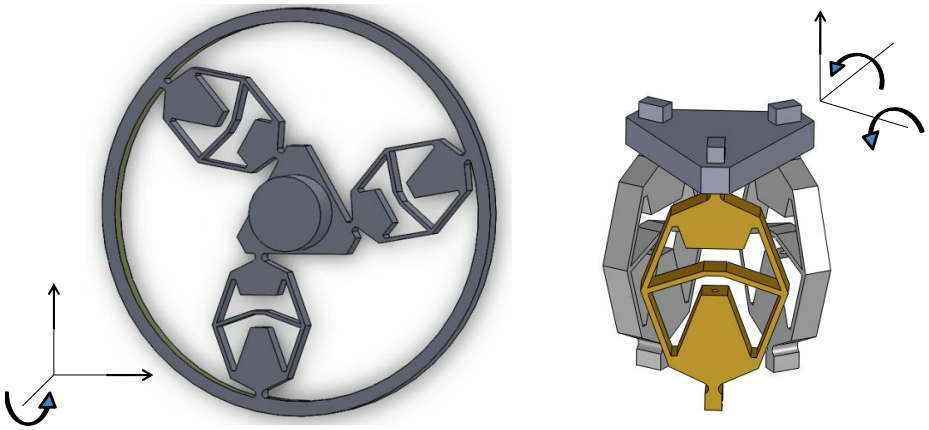


Figure 39: The possible multi-axis force sensing configuration with the developed sensor units

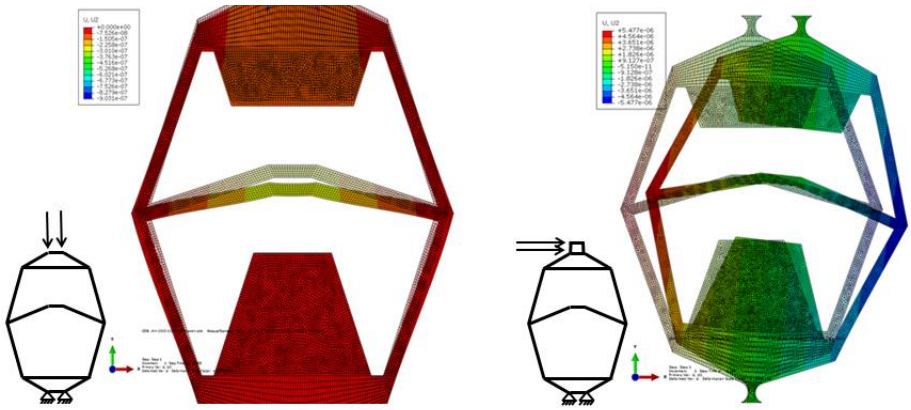

Figure 40: Preliminary FEA analysis on the deformation of the samples with loading styles)

and bottom part of the body is strengthened by adding more material. Besides improving the 1-axis sensing unit, it is aimed to expand this sensing idea to multi-axis. A combination of such sensing units can be arranged to get the desired number of freedom force sensors. Figure 16 illustrates two, triaxial sample configurations. Initial kinematic analysis yielded the following equation for the amplification ratio:

$$Amplification = Lsin\beta + \frac{\frac{w-d}{2} - cot\beta}{2h} \tag{79}$$

#### *6.1.2.1 Fabrication*

A compliant mechanism involving many hinges with sub-millimeter dimensions within a limited space brings manufacturing challenges. The manufacturing method should have sufficient resolution and should not yield the material creating residual stresses on the body. As stated, the repeatability of the deformation under load is highly important for accuracy. The material has to be polymers and that reduces the number of available manufacturing options. Among polymers, the type of the plastic brings additional constraints on available manufacturing methods.

Rapid-prototypers are often used for creating complex structures in 3D. They are exteremely helpful if the object to be created has 3D features. However, the available material types for rapid-prototyping machines are limited and only the powder of a material could be used. Also, due to the layer-by-layer manufacturing method of rapid-prototypers, the material undergoes a thermal treatment which is effective on the materials mechanical properties.

Laser-cutter is a suitable process as it has a great resolution yet Acetal Delrin, which is a recommended material for its repeatability and machinability, cannot be cut by laser-cutter since the laser beams melt the material instead of cutting sharply. CNC machines or water-jet cutters can be used with Delrin. The resolution and surface quality of those processes become primary constraints in that case. Especially the hinges in a compliant mechanism require good resolution and a suitable way of cut. An alternative method, UV-lithograpy, is also limited to specific material types and this method is usually chosen for MEMS applications.

In addition to performance restrictions of the applications and mechanical properties of the materials, the manufacturing processes impose dimensional constraints to the design of small-sized structures. It is vital to have the object fabricated with no residual damage or deformation occur in the manufacturing process.

### 6.1.3 Experiments

#### *6.1.3.1 Manufacturing the Test Samples*

Available fabrication methods for the designed structure become a matter to consider if the material of interest is plastic. Fabrication opportunities vary with the type of plastic and fabrication type is a significant factor on the performance of the sensor. Delrin (Acetal) has high MRI-compatibility and relatively low hysteresis characteristics yet delrin could be cut to precision only by water jet cutter Water jet cutter has significant resolution limits compared to laser cutter or rapid prototyper. Whereas ABS-plastic is a cheap material and a complicated, 3D structure can be produced in rapid prototyper easily; but that does not guarantee better mechanical performances. Finite element simulations for two lading conditions have been made: axial loading and lateral loading cases.

#### *6.1.3.2 Experimental Setup*

A number of mechanical tests have been made to check the sensitivity of the structure in axial and lateral directions. The fiber optic cable is a plastic 0.9 mm fiber from Industrial Fiber Optics Co. and the fiber optic coupler is 50:50 IF-540 from the same vendor. The light source is 5 mW red lasers from Lasiris Inc. A magenta, silicon mirror is used in the experiments. The 1-axis sensing unit was fixed to a plastic frame as seen in Figure 41 since a real application would also be a fixture to a plastic frame. A load cell, OMEGA-DYNE LCM703-50, is attached to a linear XY-stage and positioned next to the sensor. The sensor was compressed via the linear stage in axial and lateral directions to realize the configurations in finite element analyses. The tests are done on two sensors with the same geometry but different materials. One acetal delrin piece and an ABS-plastic piece are tested under the same conditions. The output from the photodiode of the optic circuitry is amplified by an electronic circuit. The data is collected by National Instruments USB-6221 data acquisition

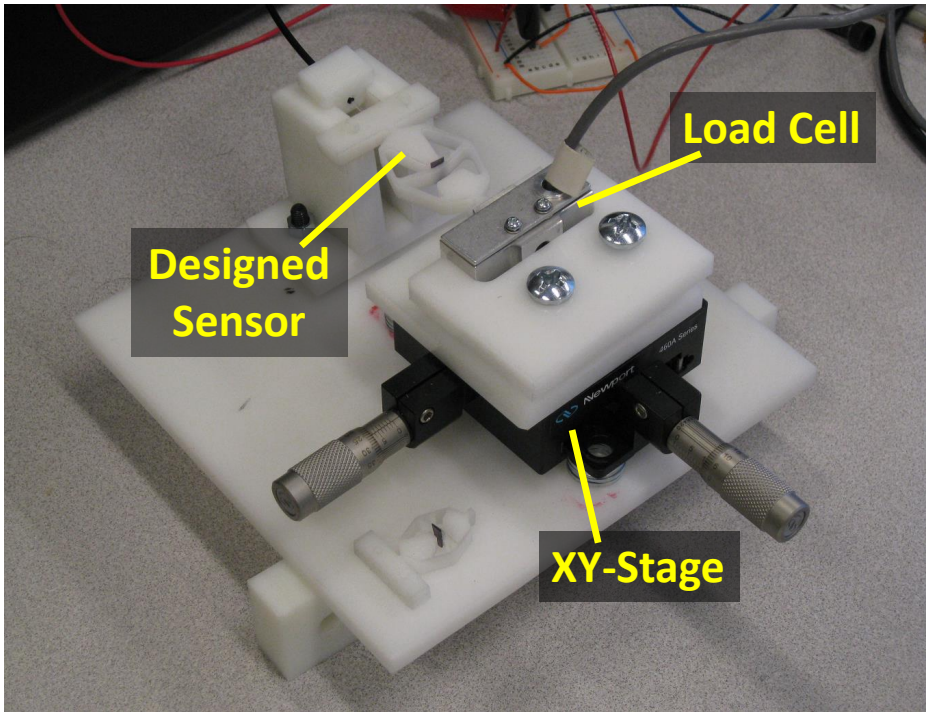


Figure 41: Experimental apparatus for mechanical testing of sensing units. Known deformations are induced by an XY-stage aligned to the sensor and the calibration data is received by a commercial force sensor.)

device.

#### *6.1.3.3 Results*

Figure 42.b illustrates the results of axial loading and lateral loading experiments conducted on delrin structure. Comparing the plots in Figure 42 the structure is concluded to be very well capable of decoupling axial and lateral forces. For 1 mm of displacement, the variation in lateral loading case is 1.66% of the variation in axial displacement. However, it is also evident that only a portion of the compression is absorbed by the sensing mechanism and the rest is absorbed by the fixture of experimental setup. The total displacement of the top of the sensor exceeds the length of the gap between fiber and the mirror which implies that the whole setup deflects during the experiment. The diagram in Fig 42.a presents the calibration data of the device made of delrin under axial loading. The output of the sensor is linearly

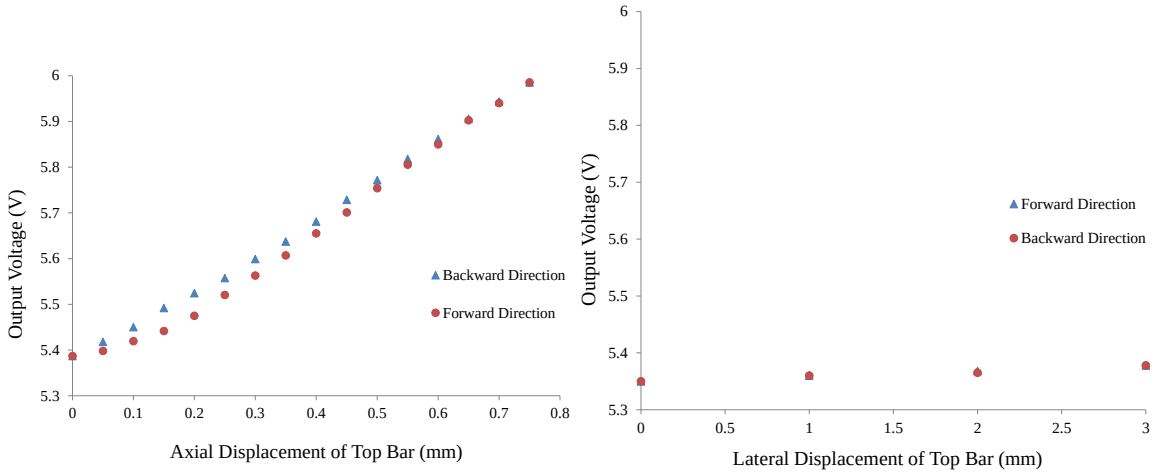


(a) (b)

Figure 42: Output voltage vs. displacement diagram that presents several loading-unloading cycles for delrin sample. The diagrams indicate that the sensor can decouple lateral load. a) Axial loading experiment. b) Lateral loading experiment. No hysteresis is seen in lateral loading case.

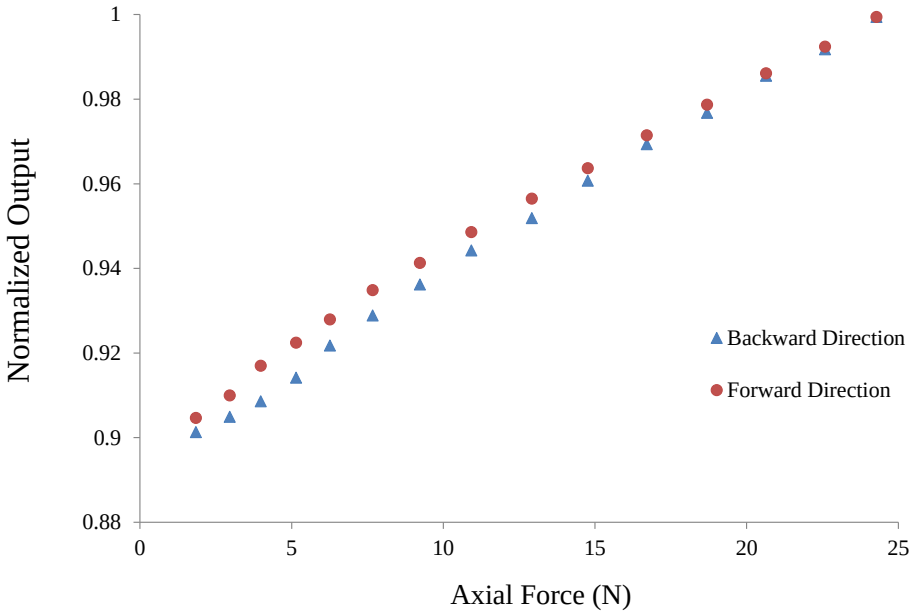


Figure 43: Calibration data for the sensor made of delrin. Hysteresis is seen in 0-5 N range. The output voltage is linear with respect to the force.

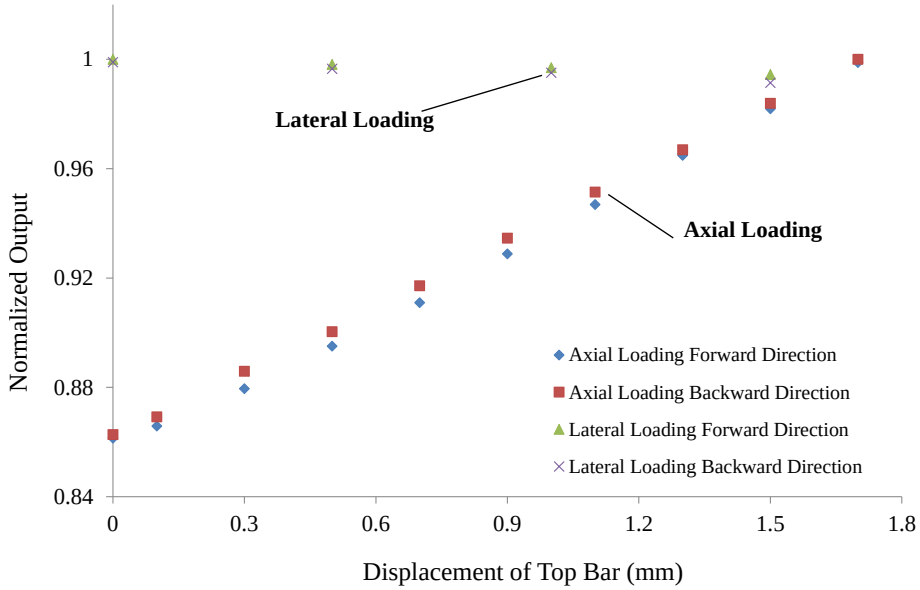


Figure 44: Output voltage vs. displacement diagram for both axial and lateral loading tests for ABS-plastic sample. The diagram involves several loading-unloading cycles for each loading case.

related to the force. Yet, a certain amount of hysteresis, 4.99%, is evident. The plots in Figure 44 and 45 show the output of same axial and lateral loading tests applied on the sensor made of ABS-plastic. Figure 44 presents both axial and lateral loading experiments revealing that the ABS-plastic sensor is also capable of decoupling axial and lateral forces. For 1.7 mm of displacement, the variation in lateral loading case is 3.29% of the variation in axial displacement. Figure 45 demonstrates the hysteresis performance of the sensor. Stiffness of the ABS-plastic piece is lower yet the hysteresis is significantly higher compared to delrin piece. The hysteresis in ABS-plastic sample is 13%.

### 6.1.4 Summary

A sensing unit to be used in multi-axis force measurements is introduced in this chapter A genuine, compact and effective displacement amplification mechanism was designed for sensing applications and analyzed by finite element simulations. The ratio of amplification in the device can be adjusted by changing several geometric

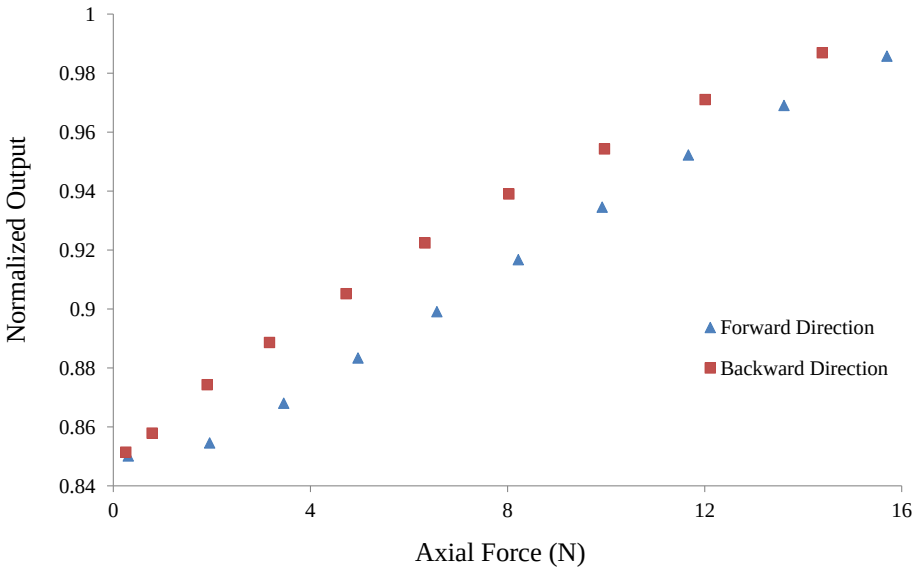


Figure 45: Calibration data for the sensor made of ABS-plastic. Hysteresis is a more significant problem for ABS-plastic sample compared to the delrin sample

parameters without compromising the compactness of the structure. Two samples made of different materials, delrin and ABS-plastic, were tested and compared for their suitability for this application. Delrin sample is realized by water jet cutter whereas ABS-plastic sample is made by 3D prototyper. Delrin sensor is superior both in mechanical performance and MRI compatibility compared to ABS-plastic unit.

Experiments showed that the sensor can decouple lateral and axial loads, which confirms that this idea can be used for multiple-axis applications. The sensitivity of the sensor in lateral direction is 1.66% of the sensitivity in axial direction. Initial linearity and hysteresis performance of the delrin sensor is promising. However, the overall stiffness of the delrin piece is higher than an acceptable value for a haptic device. In the future it is aimed to improve the force range and resolution of the device for haptic applications. To enhance the performance of the sensor, the hysteresis of 4.99% in the mechanical test data of delrin sample will also be analyzed. MRI tests confirmed that this sensor can be used for both MRI studies and surgical operations

as the SNR values calculated for both applications are satisfactory.

## 6.2 Analysis on the Precision of the Sensor

The idea of displacement amplification via compliant mechanisms (DACM) has been tailored for sensors aiming to increase the sensitivity. However, a kinematic amplification comes with a mechanical loss, meaning an increase in the stiffness of the deforming body. Also displacement amplification may require a complicated topology which may further propagate its stiffness. Therefore DACMs, even the ones with optimized topologies, may not be advantageous in sensitivity compared to non-amplifying, simple, flexible bodies. Additionally since displacement amplification modifies the deformation pattern, the amount of strain energy required for a certain output displacement is affected. Strain energy absorbed by a flexible body is related to its hysteresis error; higher the absorbed strain energy, more severe the hysteresis loss [22]. The performance of the displacement amplifying mechanism is important in both sensitivity and hysteresis aspects between which there is no straightforward relation.

In this work, a polymer based force sensor with a DACM topology, shown in Figure 38, is analyzed for both sensitivity and hysteresis. This topology has been proven to be robust in force sensing as it can decouple off-axis disturbances [81]. The performance of this proposed design is evaluated by varying the amplification factor of the topology and monitoring the changes in strain energy, which is related to hysteresis error, and output stiffness, which represents the inverse of sensitivity. Our analysis yielded the relation among amplification ratio, sensitivity and hysteresis to be utilized for an improved signal-to-noise ratio (SNR). To have a fair discussion on the benefits of the proposed design, it is compared to a primitive, low-amplification and low-stiffness, basic structure. The validity of the discussions is checked by experiments.

The deformation of the compliant structure is computed via an algorithm capable of performing a nonlinear analysis. Instantaneous deformations can be estimated using Castigliano's theorem which has been well implemented for compliant mechanisms by Howell [27]. In aforementioned works Howell's method could be directly applied since the deformation is small enough to be assumed as linear. Unlike those works, in this application, the maximum output displacement is achieved by a nonlinear deformation which requires a numeric algorithm that is capable of performing non-linear analysis. The established algorithm employs Howell's method iteratively and updates the state of the deformed body after each iteration for a better accuracy.

### 6.2.1 Method

The analytical model established in this work is based on an iterative method capable of performing nonlinear analysis. The final deformed state of the compliant structure is estimated in iterations, applying the load incrementally (a common practice to mitigate the errors associated with geometric changes during the deformation). The load-deformation relationship is predicted using Castigliano's displacement theorem. The performance of the sensor is evaluated by its amplification ratio, output stiffness and total strain energy.

The deflection at the output port of the mechanism is obtained using a method called "chain algorithm" which is explained in Howell's book [27] in detail. In this method, the body is discretized into beam members. The discretized body of the proposed force sensor as well as the model of one arbitrary beam is shown in Figure 46. Individual deformations of each beam member are calculated as if those members were cantilevered beams. At an arbitrary $j^{th}$ iteration, location of the tip of the $i^{th}$ beam member ($x_{i,j+1}$,$y_{i,j+1}$) is calculated using Castigliano's displacement theorem:

$$\delta x_{i,j} = \int_0^{l_{i,j}} \frac{M_{i,j}}{EA_i}\frac{\partial M_{i,j}}{\partial F_{x_{i,j}}}dx + \int_0^{l_{i,j}} \frac{N_{i,j}}{EA_i}\frac{\partial N_{i,j}}{\partial F_{x_{i,j}}}dx + \int_0^{l_{i,j}} \frac{kV_{i,j}}{GA_i}\frac{\partial V_{i,j}}{\partial F_{x_{i,j}}}dx \tag{80}$$

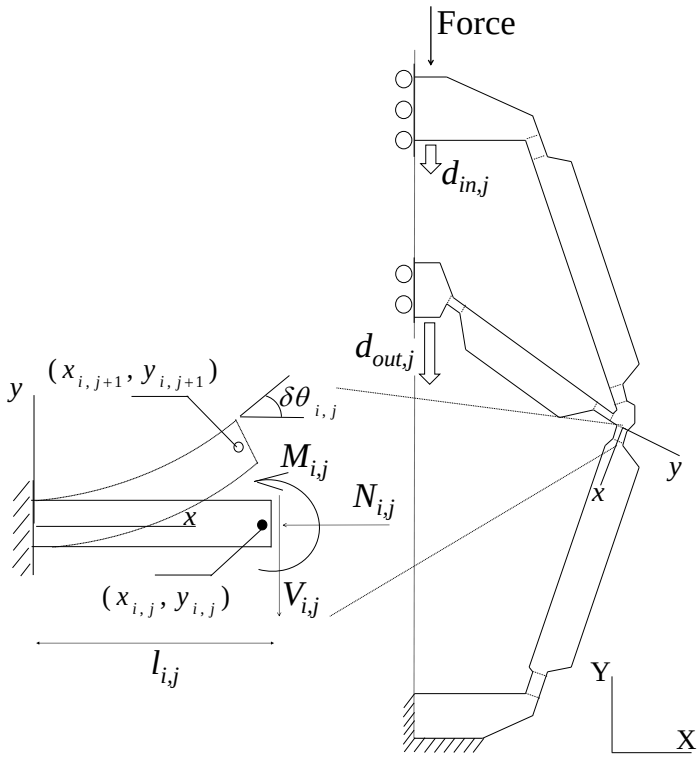


Figure 46: Symmetric half of the proposed mechanism. Each member of the structure is modeled as a cantilevered beam (on the left).

$$\delta y_{i,j} = \int_0^{l_{i,j}} \frac{M_{i,j}}{EA_i}\frac{\partial M_{i,j}}{\partial F_{y_{i,j}}}dx + \int_0^{l_{i,j}} \frac{N_{i,j}}{EA_i}\frac{\partial N_{i,j}}{\partial F_{y_{i,j}}}dx + \int_0^{l_{i,j}} \frac{kV_{i,j}}{GA_i}\frac{\partial V_{i,j}}{\partial F_{y_{i,j}}}dx \tag{81}$$

$$\delta\theta_{i,j} = \int_0^{l_{i,j}} \frac{M_{i,j}}{EI_i}dx \tag{82}$$

then

$$x_{i,j+1} = x_{i-1,j+1} + \delta x_{i,j} + l_{i,j}cos(\theta_{i,0} + \sum_{k=1}^{i-1}\delta\theta_{k,j}) \tag{83}$$

$$y_{i,j+1} = y_{i-1,j+1} + \delta y_{i,j} + l_{i,j}cos(\theta_{i,0} + \sum_{k=1}^{i-1}\delta\theta_{k,j}) \tag{84}$$

where $N_{i,j}$ and $V_{i,j}$ are the normal and transverse forces respectively and $M_{i,j}$ is the reaction moment acting on the $i^{th}$ member. $Fx_{i,j}$ and $Fy_{i,j}$ are pseudo forces in the directions of global frame ($OX$, $OY$). Elastic modulus, $E$, and the shear modulus, $G$, are kept fixed through the deformation. The length of $i^{th}$ member is denoted as $l_{i,j}$

while $A_i$ stands for the its area and $I_i$ represents the moment of area of that member. Note that $\delta\theta_{i,j}$ accounts for the change in the normal direction of the tip with respect to the local frame ($Ox$,$Oy$).

Each compliant member brings three deformation equations (equations 80 - 82). In addition, static equilibrium equations are employed to calculate the internal reaction forces $N$, $V$ and moment $M$. These equations are combined with the equations of the constraints in the deformation (shown in Figure46) and solved simultaneously. For a mechanism of n compliant members, r total members and c constraints the following augmented matrix equation is formed:

$$u^T = [\delta x_{1,j}, \cdots, \delta x_{n,j}, \delta y_{1,j}, \cdots, \delta y_{n,j}, \delta\theta_1, \cdots, \delta\theta_n \\ , M_1, \cdots, M_r, N_1, \cdots, N_r, V_1, \cdots, V_r]^T \tag{85}$$

$$K = \begin{bmatrix} k_{11} & \cdots & k_{1m} \\ \vdots & \ddots & \vdots \\ k_{m1} & \cdots & k_{mm} \end{bmatrix}$$

$$K \times u = 0 \tag{86}$$

where $m$ is the total number of equations involved which is equal to the size of the vector of variables, $u$, shown above. The matrix components, $k_{i,j}$, are determined by those $m$ equations. A proper model should yield a square matrix of full rank guaranteeing a unique solution.

For an accurate estimation on the deformation, the model of the structure is solved by a numeric algorithm capable of performing nonlinear analysis. Castigliano's theorem has been applied in compliant structure synthesis [43, 25] in order to derive a direct mathematical expression for the target performance qualifier. Unlike those works, the final state of the compliant body is calculated through iterations updating the status of the body and increasing the load after each iteration. The flowchart

in Figure 47 summarizes the algorithm of that iterative method. When the deformations on the body are significantly high, such an iterative method mitigates the errors caused by altering moment arms and normal directions of members. As the target output displacement, $d_{out}$, is attained, the iteration stops and the qualifiers: amplification factor, $A$, output stiffness, $k_{out}$, and total strain energy, $SE$, are derived for performance evaluation as shown in the flowchart. Note that the output stiffness, $k_{out}$, is the inverse of sensitivity. The amount of force added at each iteration is set by the variable: *increment* as shown in Figure 47.

The established model employs a similar method as finite element analysis softwares, yet there are two advantages in choosing such a customized routine. The algorithm described here is faster than finite element analysis packages because it deals with an assembly of fewer numbers of elements, only the beams, instead of an n-node mesh. Computing the final state of a typical configuration of the basis mechanism takes around 0.5 sec on a platform of Intel i7 @2.80GHz processor, 6.00 GB RAM and 64-bit operating system with MATLAB (R2010a) software. Also, FEA programs are not suitable for analyses made by varying several parameters.

A major limitation for this method is that it assumes a fixed elastic modulus throughout the whole deformation, although the stress-strain relationship is not linear for plastics even in the elastic range. Given the range of the stresses on the structure during the deformation, a representative fixed modulus was assumed. (See Appendix B for a detailed discussion on the selection of elastic modulus.)

In this work the hysteresis, denoted by $H$, is defined as:

$$H = \frac{max(\Delta f)}{F_{max}} \tag{87}$$

so as to have it resemble the precision of a reading on a sensor. $\Delta f$ stands for the largest gap between the outputs of the same input in the reverse directions of a loading-unloading experiment and $F_{max}$ is the output range of that experiment.

### 6.2.2 Analysis

### 6.2.3 Numerical Study

The topology of the proposed design is analyzed by varying several geometric parameters in an attempt to evaluate all possible configurations within the same footprint area. The purpose of this type of analysis is to find out how the sensitivity and precision of a sensor are affected by the amplification factor. Possible trade-offs on the performance characterization are observed while optimal configurations for sensitivity and precision are derived. The performance of allowable configurations of the proposed mechanism is compared to a primitive basis mechanism that has a simpler topology.

By definition, the proposed compliant structure should yield 1 mm of output deflection within a footprint area of 25 mm in width and 30 mm in height. A hexagonal structure of the same total area is selected as the basis for comparison. Significant geometric parameters on the proposed and basis mechanisms as well as the frame of the predefined footprint area are shown in Figure48. Note that the chosen basis mechanism is the proposed mechanism without the middle branch that connects the two vertical sides.

The geometric parameters $\phi_1$ and $\phi_2$, shown in Figure48, are selected as independent variables while the dimensions of the hinges are kept fixed. Based on the selected $\phi_1$-$\phi_2$ couple and hinge dimensions the link lengths are generated. The width of each link is adjusted so as to secure its rigidity and eliminate unwanted deformations. For a given $\phi_1$, each ($\phi_1$,$\phi_2$) configuration of the proposed design is compared to the corresponding basis mechanism with angle $\phi_1$. The comparisons are based on the resultant performance qualifiers: amplification ratio, output stiffness ($k_{out}$) and strain energy ($SE$). This procedure is repeated for two cases having different sets of hinges. In the first case (05-03 case), the hinges on the side bars (hinges 1-8 in Figure48, 0.5 mm wide) are thicker than those in the middle branch (hinges 9-12

in Figure48, 0.3 mm wide); whereas in the second case (03-03 case) all hinges are identical (0.3 mm wide). The former case represents a structure with a more flexible middle branch compared to the side bars; while in the latter; all hinges are made as flexible as possible considering the manufacturing constraints.

The contour plots in Figure 49 demonstrate the ratios of the qualifiers of the proposed mechanism over those of the basis mechanism. A value greater than 1 means the proposed design exceeds the basis mechanism in that performance qualifier. The figures 49a, 49c and 49.e belong to 05-03 case amplification, output stiffness and strain energy respectively. Sensitivity of the sensor is reduced with a higher amplification factor as seen in the parallel relation between the amplification factor, Figure 49a, and output stiffness, Figure 49c. On the other hand, the total strain energy absorbed by the structure, Figure 49e, decreases as the amplification factor is increased. As shown by the contours in Figure 49, the proposed design is generally more advantageous than the basis mechanism in the strain energy aspect, yet, only a certain number of $\phi_1$-$\phi_2$ couples yield a lower output stiffness, hence a better sensitivity. Dots on the plots represent the sample configurations tested.

The relation between amplification factor and strain energy changes when a different set of hinges is implemented. As the dimensions of the hinges are kept identical (03-03 case) the pattern in the contour plots alternated as shown in Figure 49b, 49d and 49f. In this case, the strain energy is not monotonically decreasing with an increasing amplification factor. The sensitivity of the sensor still drops as the amplification increases. The basis mechanism is better with regard to sensitivity for most configurations while a certain number of $\phi_1$-$\phi_2$ selections of the proposed mechanism attain a lower strain energy, hence a better precision than the basis mechanism.

### 6.2.4 Experimental Validation

The accuracy of the described iterative method and the validity of the arguments made via the analysis are tested by loading-unloading experiments performed on three specimens: a particular configuration of the basis mechanism and two corresponding configurations of the proposed mechanism with different amplification factors. Deformations of the samples, estimated by the analytical method, were compared to the experimental results.

The configuration selection of the samples was made using the data obtained by the analysis presented here. The basis mechanism sample was selected to have an amplification factor of 1 (i.e. no amplification). One of the samples of the proposed mechanism, sample A, has a similar output stiffness as the basis mechanism; whereas the other, sample B, achieves a higher amplification factor with a higher output stiffness yet much lower strain energy compared to the basis mechanism. The dimensions of the hinges on the tested mechanisms were selected to be the 05-03 case since the difference between the proposed and basis mechanisms is more significant in that case. Table 5 presents the independent parameters which define the amplification factor of the manufactured samples. All samples are cut from a 5.1 mm thick delrin sheet using a water jet cutter. Due to the inaccuracies in the manufacturing process the values of those parameters and dimensions of the hinges were not perfectly identical to those intended. A detailed list of the measured thickness values of the hinges of the tested samples is given in Appendix B. The analytical model is updated considering the measured hinge dimensions. In the experiments, a known displacement was applied on the input port of the samples using Newport 460A X-stages. The applied force at the input port was measured by a Futek LSB200 JR S-Series load cell and the deflection at the output port was measured using optoNCDT 1300 laser displacement sensor. Figure 48 shows the input and output ports of each sample and a picture of the experimental setup for the basis mechanism is shown in Figure50. In the first

Table 5: Significant parameters of the selected configurations

| Model | $\theta_1$ | $\theta_2$ |
|---|---|---|
| Basis Mechanism | 22° | - |
| Sample $A$ (Modarate Amplification Mechanism) | 21° | 34° |
| Sample $B$ (High Amplification Mechanism) | 22° | 17.2° |

experiment, performed on the basis mechanism, an effective elastic modulus constant was determined to be 2.3 GPa. The same empirical value was applied to all other cases. A more detailed explanation on the elastic modulus determination is given in Appendix B.

Since plastic, rubber-like materials exhibit altering deformation curves after each time being loaded, several loading-unloading cycles have been performed on the samples so as to have a fair discussion on their mechanical performances. The tests indicated no sign of softening or major repeatability errors. Details on the loading-unloading cycles of the experimental procedure and a discussion on the altering deformation behaviors of plastics due to stress relaxation, and Mullins effect is given in Appendix C. Figure51 presents the results of the analytical method and the experimental data. The resultant sensitivity, strain energy and hysteresis of each specimen, calculated using the experimental data as well as the estimations of the analytical model, are given in Table 6. The values calculated by the analytical method are given in parentheses. Analytical model data follows the same deformation trends as the experimental data, yet the analytical model appears stiffer than the samples. One of the main reasons for the error is the inaccuracy in the manufacturing process. 2D power cutting tools like water jet cutter often results in a V-shaped cut profile which makes it impossible to determine the true geometry of a hinge and the stiffness of a compliant mechanism is very sensitive to the thickness of the hinges. The samples involve more than 10 hinges per structure and due to the random nature of the manufacturing errors the symmetry on the structures is not guaranteed. The error could also be ascribed to the rigid boundary conditions which are not perfectly realistic and

Table 6: Performance qualifiers of the tested configurations

| Model | Strain Energy in mJ | Hysteresis | Sensitivity in mm/N | Overall Quality (SNR) |
|---|---|---|---|---|
| Basis Mechanism | 2.187 (2.385) | 0.135 | 0.227 (0.202) | 1.682 |
| Sample A-Modarate Amplification Mechanism | 0.815 (0.941) | 0.046 | 0.281 (0.239) | 6.109 |
| Sample B-High Amplification Mechanism | 0.550 (0.684) | 0.036 | 0.204 (0.178) | 5.667 |

the problem of non-linear stress-strain curve of the material i.e. variable elastic modulus. The method still estimates the deformation of a mechanism with several hinges with an error about 20%, which is not severely high compared to similar experimental works [44].

The experiments confirmed the parallel relation between hysteresis and strain energy predicted by our analysis as shown in Table 6. Sample B has the least hysteresis, yet it is poorer with regard to sensitivity than the basis mechanism. A slightly higher amount of hysteresis could be traded for a better sensitivity by selecting sample A. It is superior to the basis mechanism in both sensitivity and precision. If the ratio of sensitivity over hysteresis is accepted as a quality indicator for the overall sensing performance, describing the signal-to-noise ratio (SNR) of the sensor, sample A becomes the best among the samples tested. All these experimental results confirm the arguments made using the theoretical analysis.

### 6.2.5 Loading Cycles on Plastic Samples

In order to decouple the hysteresis error from other elements such as Mullins effect, softening and stress relaxation, a certain procedure was followed for all specimens. Firstly, three consecutive loading-unloading cycles were performed on the specimens.

A maximum output displacement of 1 mm was aimed in each cycle, and was completed in less than two minutes, depending on the amplification factor of the mechanism being tested. Following the consequtive loadings, the specimens were allowed to rest for 15 minutes for recovery. After the recovery, a fourth run was completed. The fourth run was followed by another recovery session of 15 minutes and a fifth run. Figure 52 shows the force-deformation data for the basis mechanism.

As shown in Figure 52b, the hysteresis error is mitigated after the repetitive cycles but partially recovered after a certain recovery session. However, there is no indication for softening or a drop in stiffness caused by these cycles, as shown in Figure 52a. The hysteresis error after recovery is repeatable for the specimens and the stiffness of the samples did not change significantly after multiple full-scale loadings. For the discussion in this article, the fifth runs were taken into account so as to get rid of the effects of consecutive loadings. Since the specimens presented no softening during the process, the Mullins effect was ruled out [4].

#### *6.2.5.1 Discussion*

We analyzed our proposed design to improve its sensing performance and characterized its performance with regard to both sensitivity and precision aspects. Rather than exercising a size and shape optimization routine, we compared the advantages of the proposed displacement amplifying compliant mechanism over these of a simpler, low or no-amplifying body. Such a comparison and a variation analysis yielded important insight on the use of displacement amplification on sensors. Depending on the set of hinges, high sensitivity and low hysteresis may become pareto qualifiers leaving a trade-off on the selection of optimal configuration. Displacement amplification can improve the signal-to-noise ratio (SNR) of a sensor by reducing the hysteresis error rather than increasing the sensitivity.

As shown in the analysis of selected cases, the amplification factor raises the

stiffness of the structure, making it harder to deform. This is consistent with the fact that amplification mechanisms do not necessarily improve the sensitivity. In the two cases analyzed herein, the proposed design was not significantly better with regard to sensitivity compared to the basis structure. However, its benefits become apparent when the total strain energy is considered. The proposed design reduces the necessary strain energy for an identical output deflection alleviating the hysteresis problem. The range of such advantageous configurations changes with hinge set, since the variations of the sensitivity and strain energy depend on the relative dimensions of the hinges. For the 05-03 case, a limited range of ($\phi_1$,$\phi_2$) selection yields both an improved sensitivity and precision; whereas for the 03-03 case, (when all the hinges are 0.3 mm), the proposed design cannot improve the sensitivity compared to the basis mechanism. It can, however, enhance the precision for a certain number of configurations.

To the best of our knowledge, there is no perfectly objective, indisputable method for comparing two displacement amplifying compliant mechanisms (DACM) with different topologies taking all performance qualifiers into account. In this work, the analysis of the proposed design is driven by the question: "What is the advantage of our specially designed mechanism over an ordinary, simple body" i.e., is it worth using such a complex structure instead of a simple geometry for force sensing? A hexagonal body was taken to be the basis mechanism for comparison since it allows for a translational displacement at the output port and could be adjusted to low or no amplification configurations. This analysis showed that it is the *hysteresis error* of the force sensor on which a DACM has the biggest impact. Optimizing a topology for sensitivity does not assure a better sensor; since even when it degrades sensitivity, a DACM can still prove to have a better SNR than a basic structure.

The experiments confirmed the outcomes of the analysis showing the trade-off between sensitivity and hysteresis. Among the selected configurations of the proposed

design, sample A is superior in both sensitivity and hysteresis to the selected basis structure. On the other hand, sample B is not better in sensitivity compared to the basis mechanism, yet it has a considerably higher SNR mainly because of its mitigated hysteresis error. Our hypothesis on the relation between strain energy and hysteresis was confirmed by the experiments. The numeric estimations made using the analysis are in parallel with the experimental results.

The inaccuracies in the manufacturing process of polymers may yield a structure different from what has been attempted to obtain. This could result in a drastic decrease in the expected performance of an optimal design if its optimality is so sensitive to the geometry of its members. The manufacturing tolerances and robustness of the optimization process should be considered when designing a DACM.

The analysis presented here is insufficient for proposing a genuine objective function that takes the hysteresis of a sensor into account. The direct numerical relation between strain energy and hysteresis, i.e. the weight of strain energy's effect on hysteresis, is not clear. Hysteresis should be explicitly defined by the design parameters for a helpful objective function which brings SNR into consideration. Also, the calculation method utilized in this study assumes a constant elastic modulus, whereas, in reality that of a plastic material such as delrin is not perfectly constant. An advanced method that could take varying elastic modulus without compromising other abilities of the existing algorithm could achieve an improved accuracy.

## 6.3 Conclusion

An MRI compatible force sensor, that is comprised of a displacement amplifying compliant mechanism, introduced in an earlier work [81], was analyzed for its sensitivity and precision. The results of the analysis were utilized to enhance the SNR of the proposed sensor. An iterative method capable of performing nonlinear analysis, faster than commercial softwares and applicable to any iterative study was established. The

effects of displacement amplification on the sensitivity and precision of the proposed force sensor were investigated and the proposed design was compared to a simple, low, or non-amplification mechanism. The analysis on the topology of the proposed compliant mechanism showed that an aggressive amplification raises the stiffness of the structure, degrading the sensitivity; yet it also lowers the strain energy absorbed by the structure, mitigating the hysteresis problem. The optimal configurations for sensitivity and precision vary with the stiffness values of the set of hinges on the mechanism. Predictions on the optimal configurations made by the analysis were confirmed by the experiments conducted on three samples of different configurations. An error of about 20% was observed compared to the analytical method which can be ascribed to the inaccuracies in the manufacturing technique, water-jet cutting.

Rather than optimizing the topology for a certain objective function as practiced in previous works, the analysis done herein provides an insight on the benefits of displacement amplification. The use of a DACM as a sensor should not be viewed only with regard to the aspect of sensitivity. The analysis on the stiffness and the amplification ratio of the design showed that the hinge dimensions have a significant influence on the efficacy of the deformation amplification. DACM topologies with a lower sensitivity may still improve the performance of sensors since the amplification of displacement can reduce the problem of hysteresis, enhancing the signal-to-noise ratio of a sensor. Lower hysteresis error, hence better precision, is the key factor that makes a displacement amplifying topology advantageous against a simple, flexible, low-stiffness body. Experiments on selected configurations of our proposed design showed that SNR of the proposed force sensor could be up to 3-4 times that of a non-amplifying structure.

### 6.3.1 Summary

MRI compatible force sensors are important components in medical robotics as they enable force feedback in a challenging environment for surgical and assistive robots. This paper analyzes a novel MRI compatible force sensor comprised of a displacement amplifying compliant mechanism (DACM) made of polymers. Hysteresis is an inevitable problem for sensors made of polymers which reduces the precision in measurements. Displacement amplification affects both the sensitivity and hysteresis error of a sensor, yet does not ensure an improvement in either of them. Optimization methods based solely on amplification ratio or sensitivity may be ineffective on reducing the hysteresis issue and result in a design with insufficient signal-to-noise ratio (SNR). Unlike previous works that are focused on optimizing topologies with regard to a specific objective function; this work presents an analysis that accounts for both sensitivity and hysteresis. An iterative method capable of performing nonlinear analysis is established in order to monitor sensitivity and hysteresis error of the proposed sensor topology and find out how those are affected by the amplification. Optimal configurations for sensitivity and precision are deduced and the predictions made by the analysis are confirmed by experiments. This study indicated that sensitivity of a compliant mechanism could be traded for a lower hysteresis error i.e. higher precision. DACMs could be targeted to achieve a low hysteresis error rather than improving the sensitivity in a sensor. Compared to a non-amplifying, basis structure our proposed design achieved a 3-4 times higher SNR, mostly due to its higher precision.

In this work, the analysis of the proposed design is driven by the question: What is the advantage of our specially designed mechanism over an ordinary, simple body i.e., is it worth using such a complex structure instead of a simple geometry for force sensing? A hexagonal body was taken to be the basis mechanism for comparison since it allows for a translational displacement at the output port and could be adjusted to low or no amplification configurations. This analysis showed that it is the hysteresis

error of the force sensor on which a DACM has the biggest impact. Optimizing a topology for sensitivity does not assure a better sensor; since even when it degrades sensitivity, a DACM can still prove to have a better SNR than a basic structure.

Rather than optimizing the topology for a certain objective function as practiced in previous works, our analysis provides an insight on the benefits of displacement amplification. The use of a DACM as a sensor should not be viewed only with regard to the aspect of sensitivity. DACM topologies with a lower sensitivity may still improve the performance of sensors since the amplification of displacement can reduce the problem of hysteresis, enhancing the signalto-noise ratio of a sensor. Lower hysteresis error, hence better precision, is the key factor that makes a displacement amplifying topology advantageous against a simple, flexible, low-stiffness body. Experiments on selected configurations of our design showed that SNR of the force sensor could be up to 3-4 times that of a non-amplifying structure.

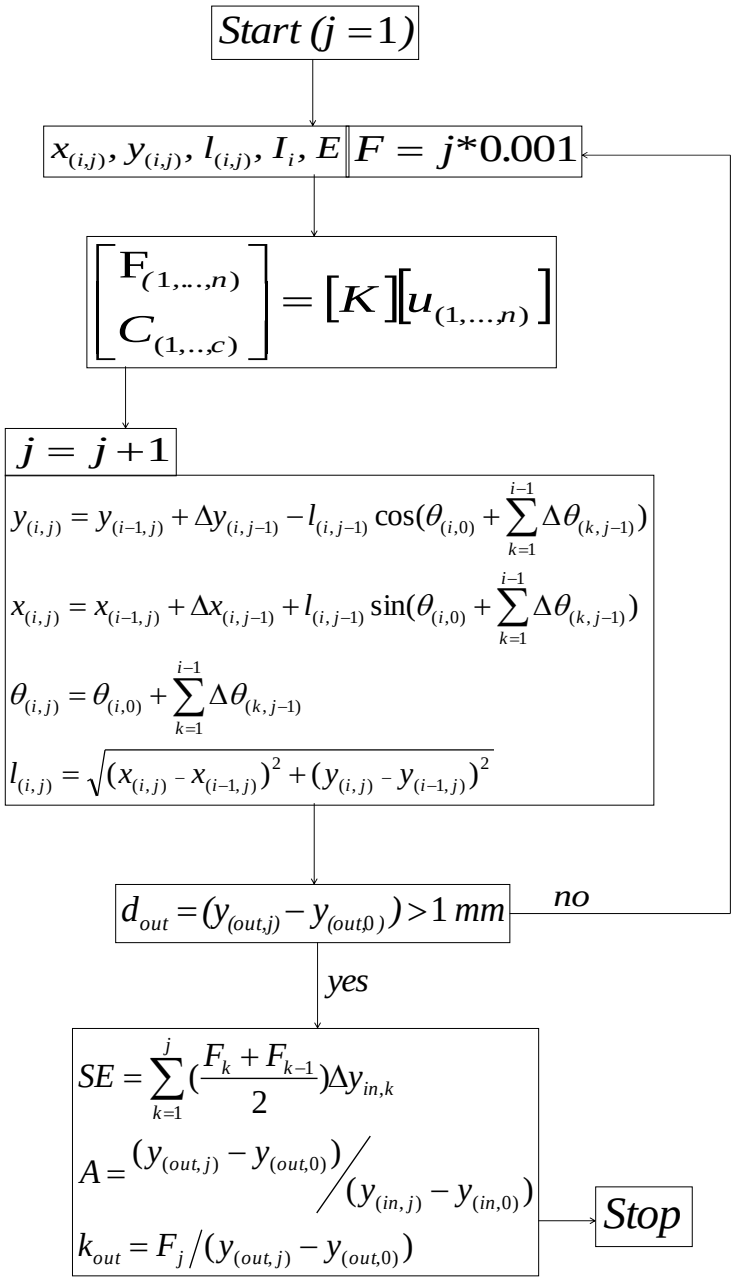


Figure 47: Flowchart of the iterative method developed for the nonlinear analysis of a compliant mechanism. The variables updated at each iteration are expressed with two subscripts: $i$ for the member and $j$ for the iteration number. $u$ is the vector of variables while $K$ is the corresponding square matrix as described in (86). The target output displacement is denoted by $p$ and the total number of members is $r$. The subscripts *out* and *in* refers to the output port and input port of the structure respectively.

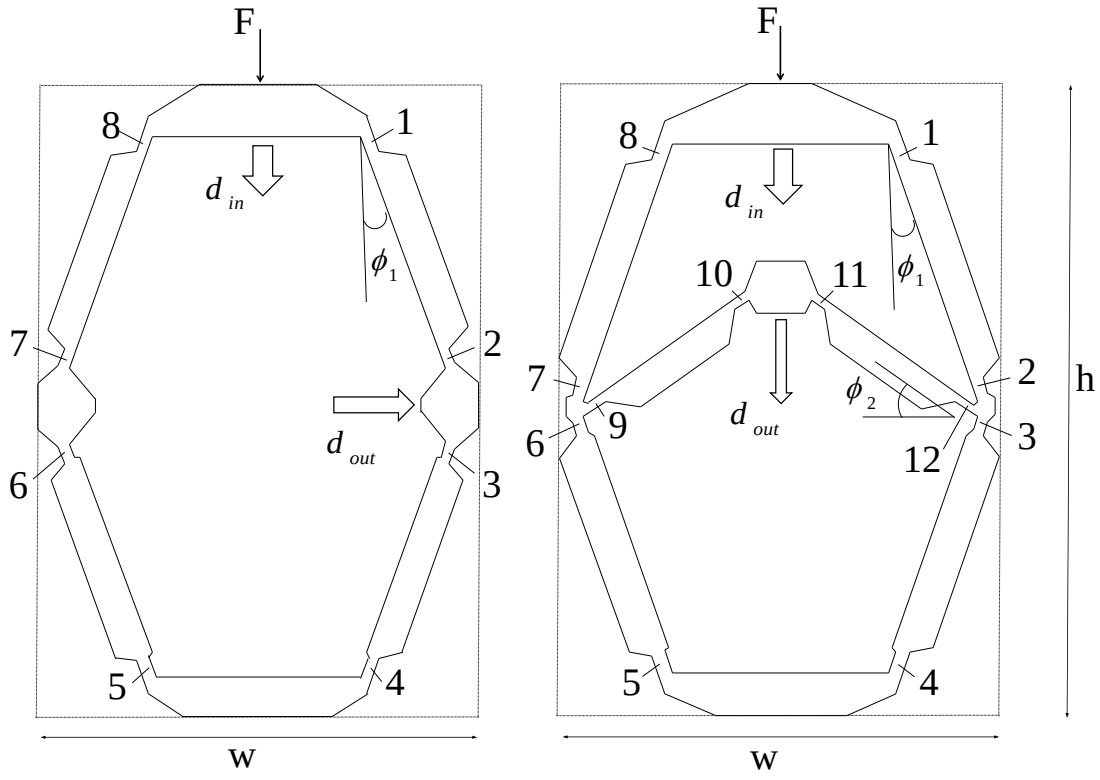


Figure 48: Full models of the basis mechanism (on the left), the proposed compliant mechanism (on the right). The hinges on the bodies are numbered. The footprint area for the mechanisms are defined by the parameters $h$ and $w$ as height and width respectively.

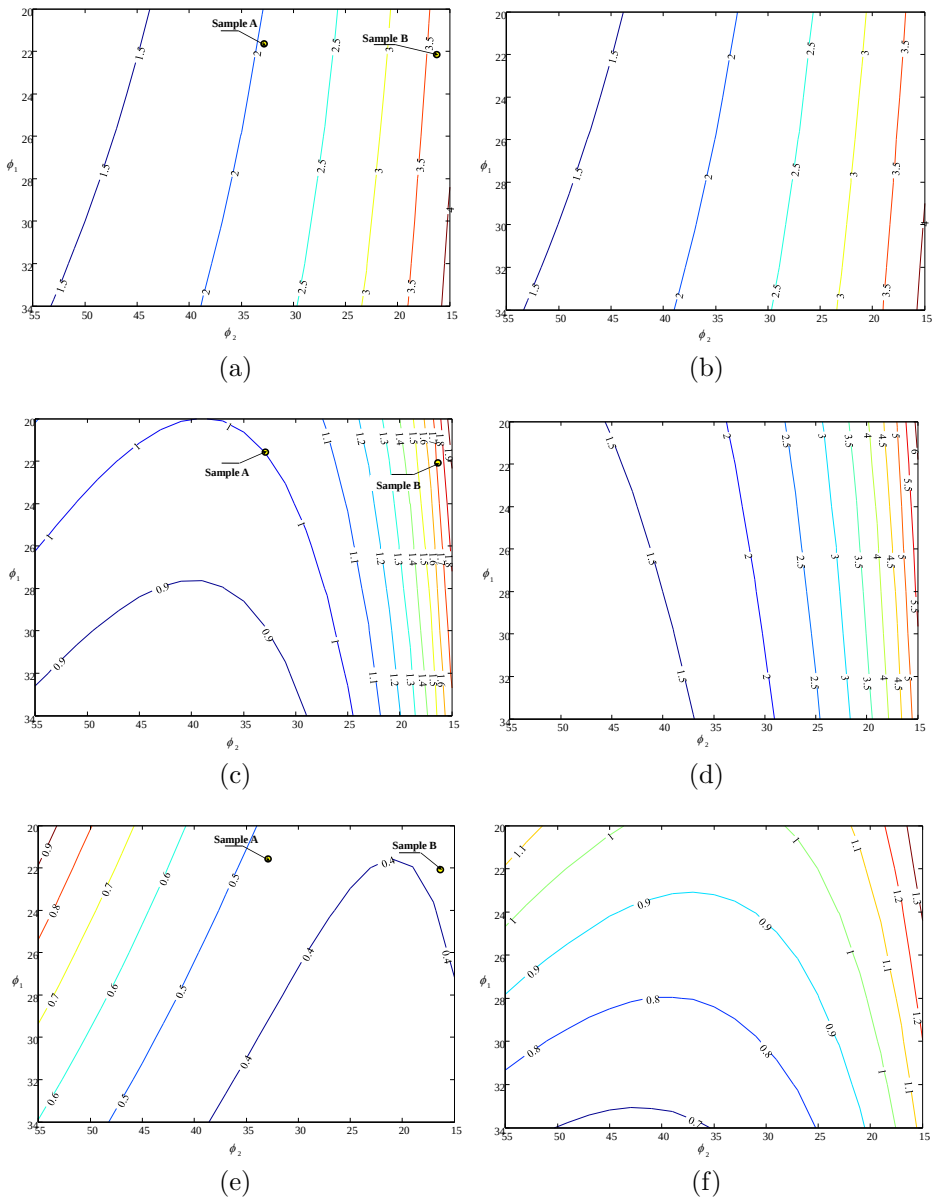


Figure 49: Contour plots showing the ratio of performance qualifiers of the proposed and basis mechanisms. Two configurations that were tested are shown by dots on the corresponding plots. a) The ratio of amplification factor of the proposed mechanism to that of corresponding basis design for the 05-03 case. A value more than 1 means that the amplification ratio of the proposed design is higher. b) The ratio of amplification factor values for the 03-03 case. c) The ratio of output stiffness of the proposed mechanism to that of corresponding basis design for the 05-03 case. A value less than 1 means that the proposed design has a higher sensitivity at that configuration. d) The ratio of output stiffness values for the 03-03 case. e) The ratio of strain energy of the proposed mechanism to that of corresponding basis design for the 05-03 case. A value less than 1 means that strain energy of the proposed design is smaller at that configuration. f) The ratio of strain energy values for the 03-03 case.

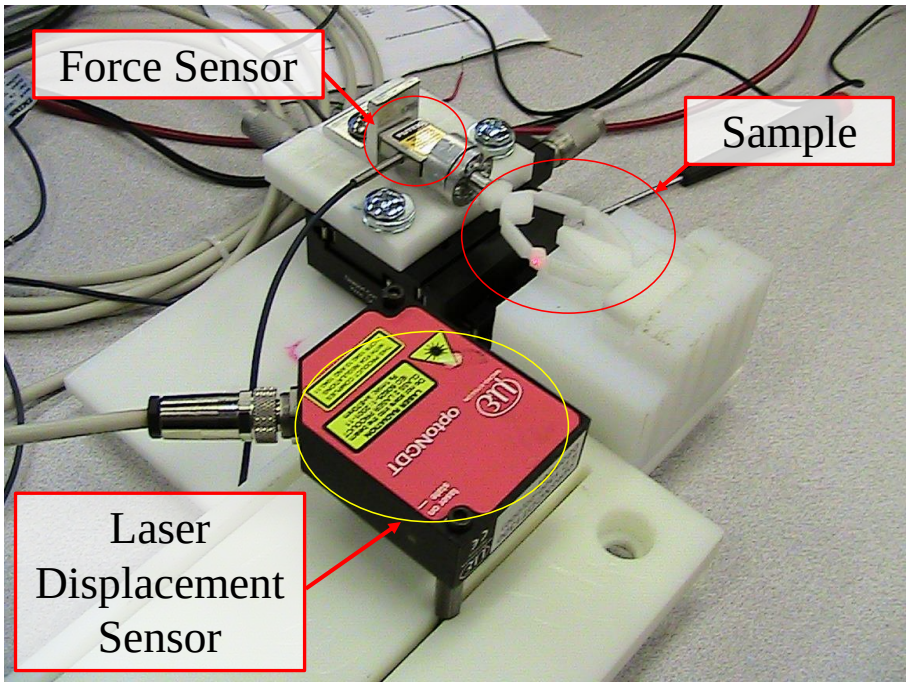


Figure 50: Experimental setup showing the displacement and force measuring apparatus

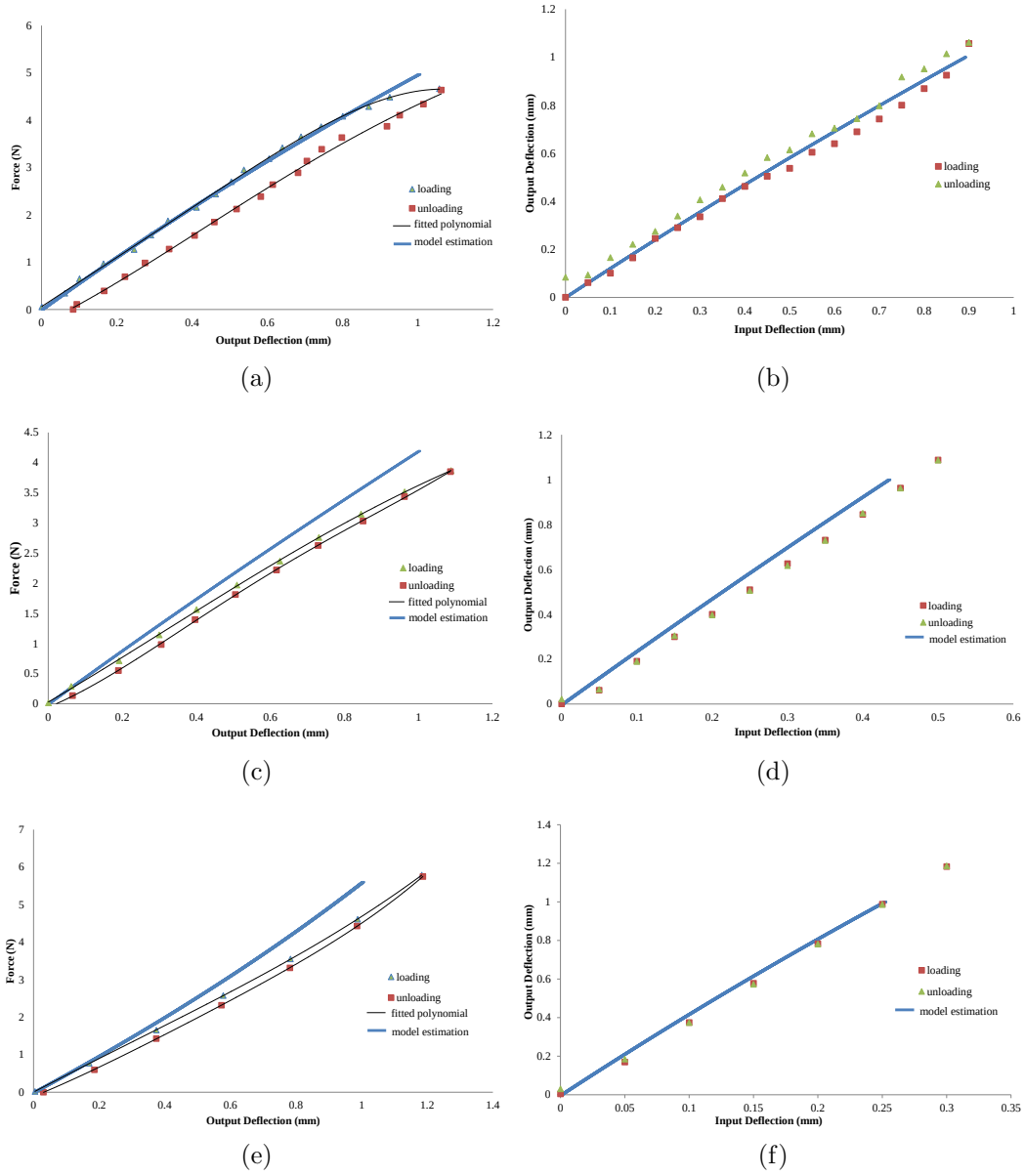


Figure 51: Experimental results (dotted) in comparison with the calculations of the analytical method. On the force vs. deformation plots, $4^{th}$ order polynommials are fitted to the experimental data points. a,b) Deformation of the basis mechanism c,d) Deformation of sample A, the one with a moderate amplification factor e,f)Deformation of sample B, the one with a high amplification factor

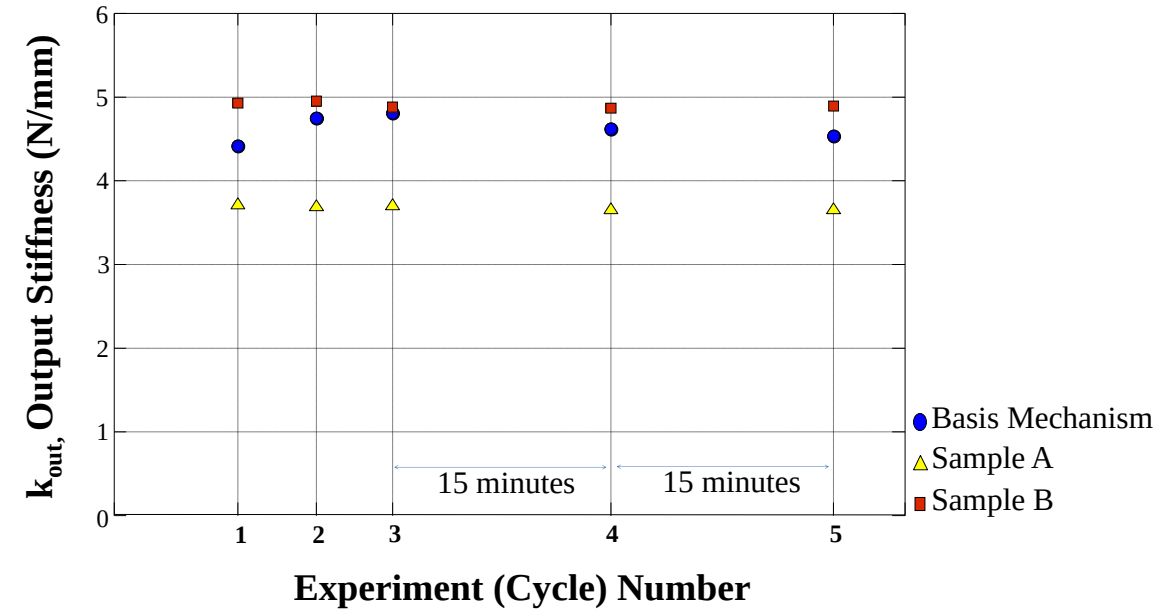


(a)

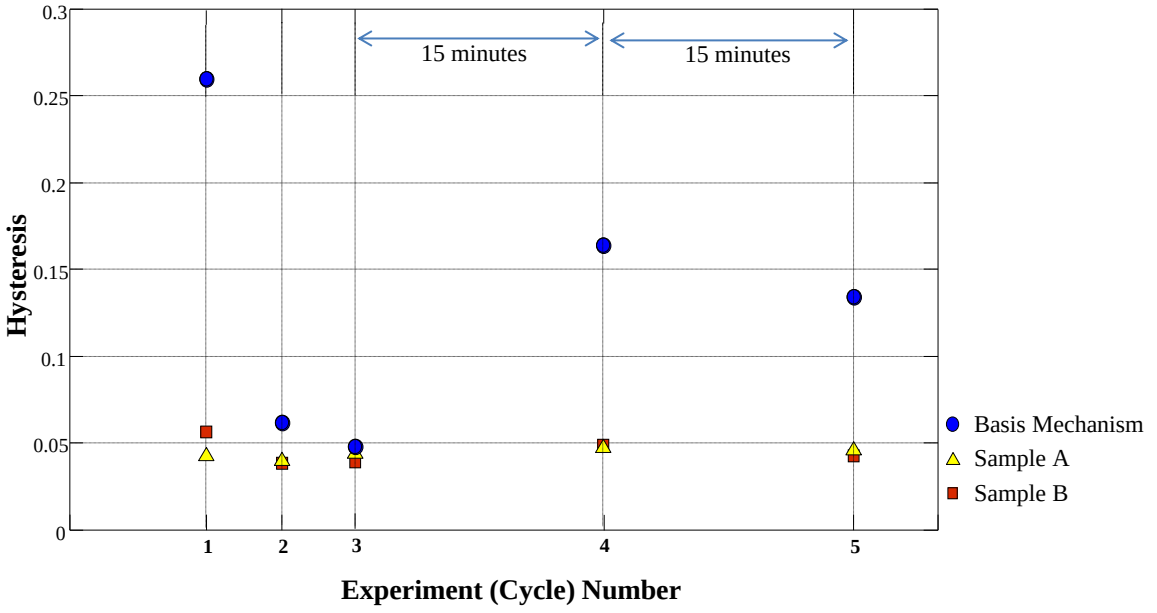


(b)

Figure 52: Performance of specimens after 5 loading-unloading cycles a) Output stiffness of the samples b) Hysteresis levels for each cycle

# CHAPTER VII

# CONCLUDING REMARKS

Pneumatic actuators make for suitable platforms to implement robotic rehabilitation in MRI for their inherent MRI compatibility and compliance. Compared to hydraulics, they are low-maintenance and they have a moderately higher bandwidth. However, they are required to be driven through transmission lines that affect the pressure dynamics and the use of conventional pressure sensors to obtain actuator pressures is restricted. Conventional pneumatic system models fail to represent the dynamics of the actuator in the presence of transmission lines. The mainstream approaches neglect the higher order dynamics on the transmission lines and, in return, achieve poor accuracy in the pressure estimation and control. This thesis is oriented to provide tools and methods that will increase the control bandwidth of pneumatic tele-operated systems. To solve the problem of characterizing the actuator dynamics, a pressure observation algorithm that utilizes force and displacement feedback was designed in this work. In addition, a non-linear model-based controller that accounts for the dynamics of the transmission lines was established for control accuracy at a high frequency. As the pressure observation relies on having a force feedback, an MRI compatible force sensor was designed and its topology was improved for better sensitivity and precision.

Several experiments were conducted to support the designed methods and the sensor. The improvement on the pressure estimation accuracy brought by the proposed observer was demonstrated by force and impedance controlling experiments. Similarly; contribution of the observer on the impedance control accuracy of a typical tele-operation setup was demonstrated. The line model-based controller, developed for

further improvement in the control performance, was also tested in the lab conditions. This thesis presents theoretical contributions with corresponding proof-of-the-concept experimental validations. The outcomes of this work can be transferred to next generation pneumatic tele-operation robots. This study also included a prototyping-related work on the design of an MRI-compatible force sensor. Provided with the prototype is a discussion on the hysteresis problems of compliant mechanisms. Based on the deformation analysis carried out in this study, the hysteresis problems of the designed sensing structure were mitigated.

Ultimately, this research aims to enable high-bandwidth haptic interaction in MRI via pneumatically driven systems. The typical motivation of rehabilitation robots is to provide a desired impedance while interacting with a patient. Providing the desired impedance is related to the z-width of the developed interface, which is closely related to the bandwidth of the controlled system. This study achieved a good progress towards increasing the bandwidth of pneumatic tele-operation. An obvious future work for this research is implementing the developed algortihms on well-designed, MRI-compatible haptic interfaces. Following that, suitable rehabilitation procedures for pneumatic, tele-operated systems should be identified. Pneumatic interfaces can apply various physical therapies on stroke patients as the brain activity of the patients is being monitored by MRI machines. The tools and methods developed in this work are expected to expand the range of physical activities implemented by tele-operated pneumatic actuators.

# APPENDIX A

# VALVE CALIBRATIONS

### A.0.2 The Valve Model

The function $\psi_i$ is defined as follows:

$$\psi(P_u, P_{d_i}) = \begin{cases} \frac{|A_{v_i}|}{A_{v_i}} C_{u_v} P_u \rho_0 \sqrt{\frac{T_0}{T}} & \text{if } \frac{P_d}{P_u} \geq b \\ \frac{|A_{v_i}|}{A_{v_i}} C_{u_v} P_u \rho_0 \sqrt{\frac{T_0}{T}} \sqrt{1 - (\frac{\frac{P_d}{P_u} - b}{1-b})^2} & \text{if otherwise} \end{cases} \tag{88}$$

where $T$ is the stagnation temperature of the gas, $\rho_0$ and $T_0$ are density and temperature of air at reference conditions respectively [28], $b$ is the critical ratio of the pressures that determines whether the flow is choked or unchoked, and $R$ is the ideal gas constant. $C_{u_v}$ is the sonic conductance of the valve that is characterized by a low order polynomial of the valve input, $u_v$; hence, the orifice area, $A_{v_i}$. As shown in (88), the direction of the flow is represented with the sign of the area where a positive value means the chamber of the actuator is being charged and negative means the chamber is discharged given as:

$$\psi(P_u, P_d) = \begin{cases} \psi(P_{reservoir}, P_{actuator}), & \text{if } A_v \geq 0 \\ \psi(P_{actuator}, P_{atm}), & \text{if otherwise} \end{cases} \tag{89}$$

where $P_{reservoir}$ is the reservoir pressure, $P_{actuator}$ is the chamber pressure and $P_{atm}$ is the ambient pressure. In this research, the dynamics of the spool of a valve is neglected as the valve's bandwidth is in general significantly higher than the bandwidth of operation.

The relation between the sonic conductance and the valve input has been empirically obtained through the calibration routines explained in [28]. The conductance of each orifice size in the EnfieldTech LH05 valve is illustrated in Figure 53. The

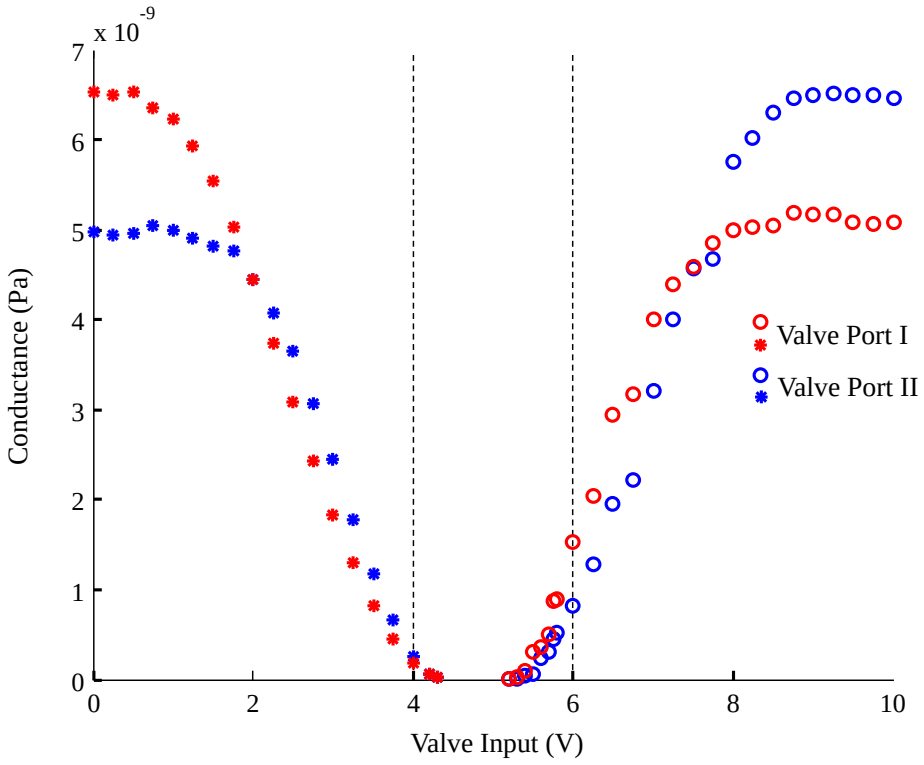


Figure 53: The valve calibration data for the EnfieldTech LH05 Valve

sign of the valve area $A_{v_i}$ was assigned to be in opposite for the two ports of the valve. The first port, Port I, was assigned a negative valve area for 0-5 v of valve input; whereas the other port, Port II, had a negative area for 5-10 V. EnfieldTech LH05 is a two-position valve, which means its spool is over-lapped. Therefore, only one side of the pneumatic system is open to the reservoir, while the other side is perfectly open to the ambient. On the other hand, the Festo MPYE-5-1/8 valve is underlapped. There is a limited operation range for the valve spool, on which both sides are partially open to the pressure source. The calibration tests revealed that the mutual inflation range of the valve does not present a significant deviation from assuming it as a two-way valve. In that range, the conductance of the valve orifice is less than 1.5% of the maximum capacity of the valve. Operating in the under-lapped range creates a finite difference in the steady-state pressures of the system. Therefore, the steady-state pressures that correspond to each valve input was measured along

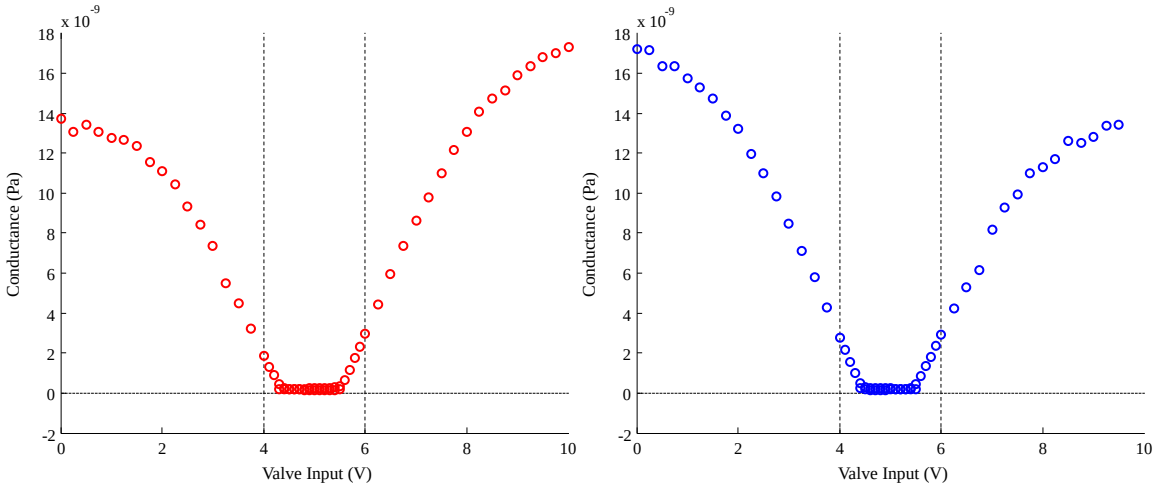


(a) (b)

Figure 54: The valve calibration data for the FESTO MPYE-5-1/8 Valve a) Valve port I b) Valve port II

with the conductance, and the measured steady-state pressures for each valve input were regarded as the upstream pressures for the valve ports. The figures 54 and 55 present the conductance and steady-state pressures of the Festo valve respectively.

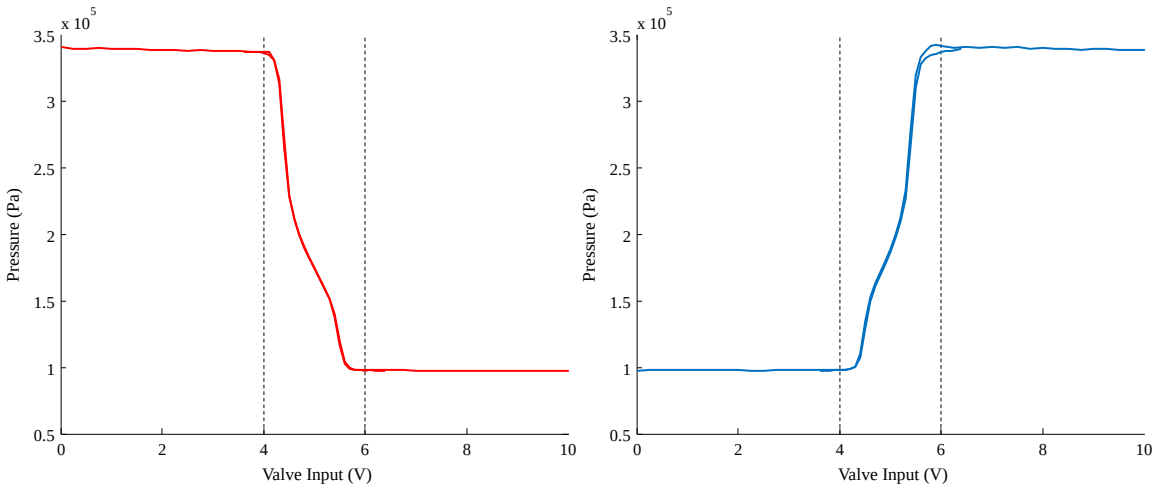


(a) (b)

Figure 55: The steady-state valve pressures for the FESTO MPYE-5-1/8 Valve a) Valve port I b) Valve port II

# APPENDIX B

# ROTAMETER MEASUREMENTS

Variable-crossection rotameters indeed measure the volumetric flowrate of a fluid flow and the scale on the device are, often, calibrated for standard conditions (14.7 psi pressure, there's no consensus on the standard temperature). If the local point where the rotameter is placed is not in standard conditions, the flowrate read on the device's scale at 'actual' condition has to be converted to an equivalent standard condition flowrate in order to compansate the variation in the density of the compressible fluid [2]. This conversion is done as follows:

$$ACFM(\frac{P_{actual}T_{standard}}{P_{standard}T_{actual}})^{\frac{1}{2}} = SCFM \tag{90}$$

where ACFM stands for actual cubic feet per minute, and SCFM is the standard cubic feet per minute. The standard condition of the rotameter comes with the datasheet of the tool.

# APPENDIX C

# ANALYSIS ON MRI SCANS

## C.1 The Method of Signal-to-Noise Ratio (SNR) Calculation

To have deeper information about the compatibility of force sensor, the SNR definition in National Electrical Manufacturers Association (NEMA) guidelines is used as follows [16]:

$$SD = \left[ \frac{\sum_1^n \sum_1^m (V(i,j+1) - V(i,j))^2}{2 \sum_1^n m - 1} \right]^{\frac{1}{2}} \tag{91}$$

$$Noise = \frac{SD}{\sqrt{2}} \tag{92}$$

$$SNR = \frac{S}{Noise} \tag{93}$$

where: $n$ is the number of rows in the image

$m$ is the number of columns in the image

$V(i,j)$ is the pixel value in the image of difference (a-b)

$S$ is the mean pixel value in the original image.

### C.1.1 MRI Compatibility Tests on the Force Sensor

In order to confirm the MRI-compatibility of the sensing unit, several imaging tests have been done. The sensing unit was brought to an MRI machine (Siemens Trio 3T) in the Center of Advanced Brain Imaging. Effect of the sensor on the image quality is analyzed by comparing the images of the PHANTOM device with and without the sensor in the imaging room. First, the sensor is placed in zone 2 and then the sensor is placed in the middle of the area of interest (Zone 1) as shown in Figure 56. This procedure was repeated for both delrin and ABS-plastic sensors. Figure 57 and 58 present the resultant images of the tests for the two configurations shown in

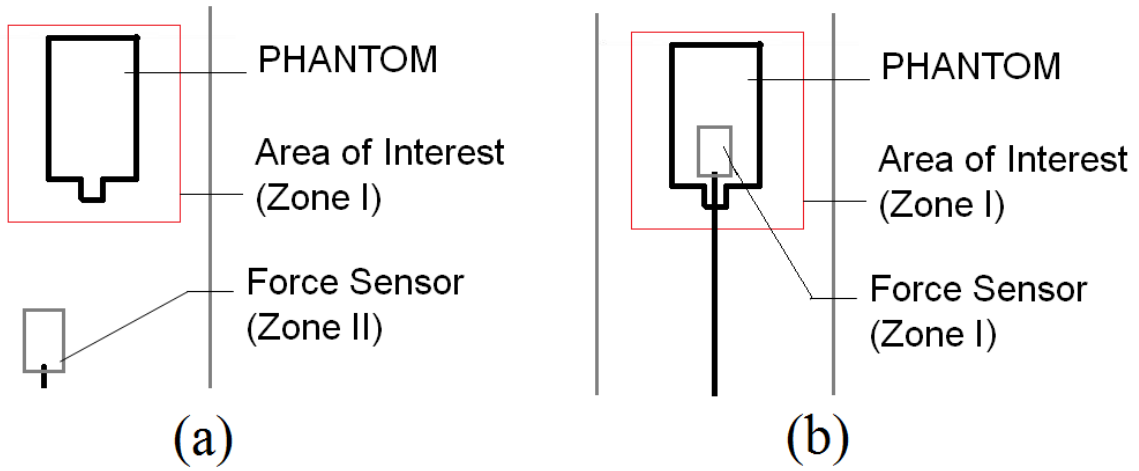


Figure 56: Configuration inside MRI chamber a) Force sensor is placed in Zone II b) Force sensor is placed in Zone I, right on top of the phantom device

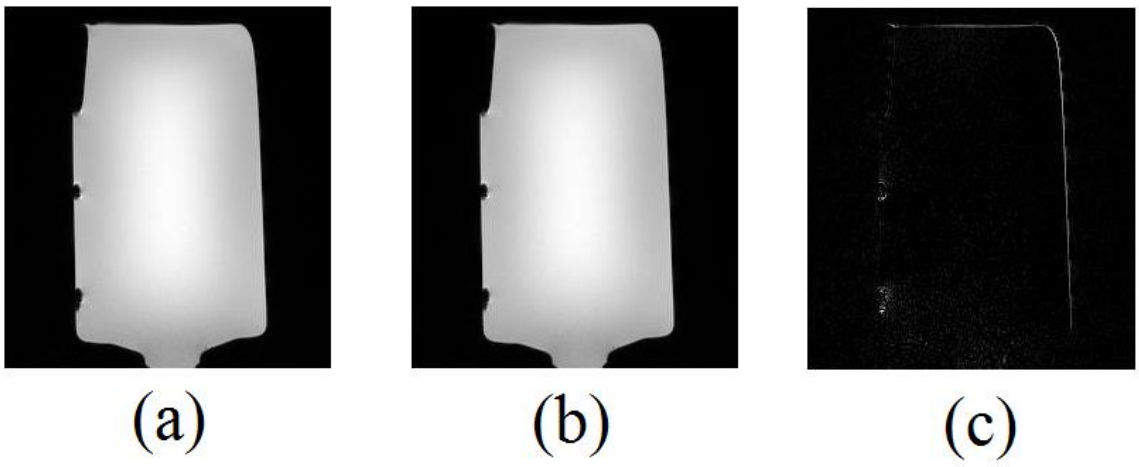


Figure 57: a) MR image when sensor is not in the room b) Image when the sensor is in zone II c) The subtraction a-b, the difference is 0.5%

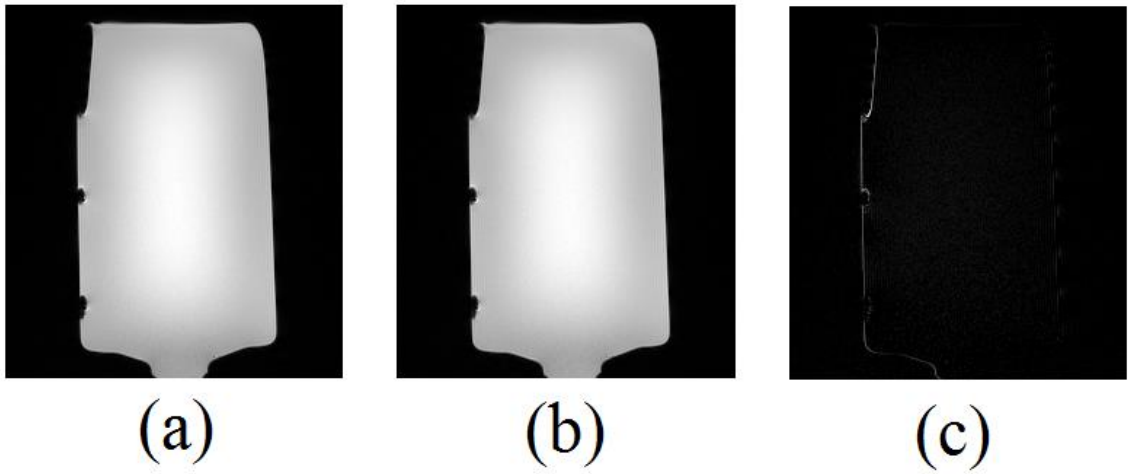


Figure 58: a) MR image when sensor is not in the room b) Image when the sensor is in zone I c) The subtraction a-b, the difference is 1.6%

Figure 56. The distortion due to the force sensor is analyzed by taking the difference between related images. As a preliminary analysis, the differences in the images are calculated as the ratio of total pixel value of difference in images with respect to total pixel value of the reference image. The sensor, made of delrin, caused only 1.6% of change in the image even when it is held in the area of interest (Zone I). Figures 57, 58 and the calculated SNR values confirm that the sensor can be safely used in both MRI studies and surgical operations. For the first case (sensor in zone II), the SNR is 105.57 whereas SNR becomes 56.36 for the second case. Same type of calculations and tests have also been applied to ABS-plastic sensor but the SNR values were 49.7 and 86.9 respectively which are lower compared to the delrin sample. These experiments showed that the sensor does not affect the image significantly even when it is in the middle of the imaged area hence it can be safely used for even Zone I applications.

### C.1.2 MRI Compatibility Tests on the Haptic Interface

A similar compatibility analysis was made on the prototype itself while the sensors are active. The haptic interface involves the developed force sensor at the tip of the piston, an optical encoder (US Digital E2, 180 CPI) and the MRI-compatible

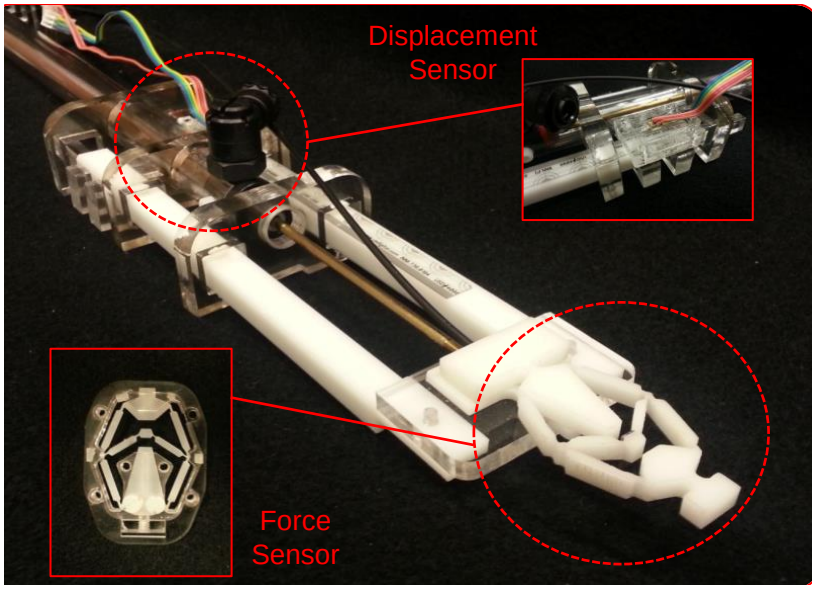


Figure 59: The haptic interface prototype that is comprised of a force sensor, an optical encoder and a MR-compatible cylinder

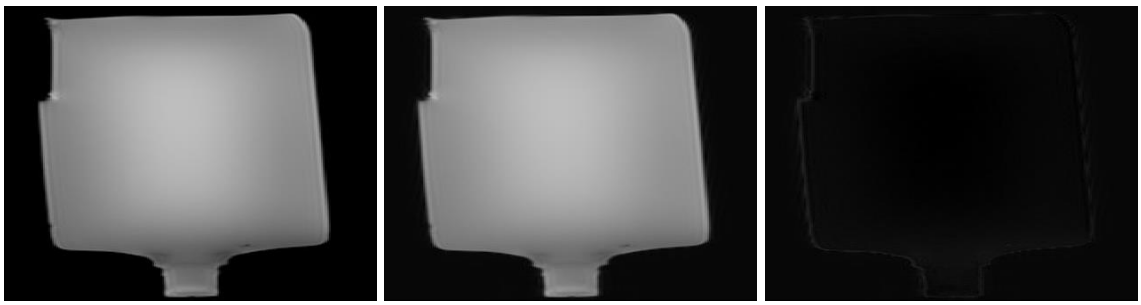


Figure 60: a) MR image when the device is not in the room b) Image when the device is in zone II and active c) The subtraction a-b, the difference is 2.6%

commerically available actuator (Airpel, MR series). Figure 59 presents the assembly of these listed components. The device was placed in Zone II and the distortion it brings was measured as explained. Figure 60 shows the preliminary visual results. The device created a small artifact of 2.6% in the image. The SNR of the output was 20.16, which indicates a good clarity in the scan.

# APPENDIX D

# OPTICAL SENSING PRINCIPLES WITH SINGLE FIBER CABLE

The sensing principle of the proposed MRI compatible force sensor is based on translation of a mirror that faces to a fiber optic cable as shown in Figure 38. A single fiber optic cable both emits light towards the mirror and collects the light rays reflected from the mirror. As the gap between the fiber optic cable tip and the mirror changes, the amount of light energy collected by the cable varies. The collected light energy is converted to voltage by a fiber optic circuitry [41].

The relation between the mirror-to-fiber distance and the output voltage of the optic circuitry has been realized by an experiment. A magenta mirror made of silicon is mounted on a single axis translation stage and aligned to a plastic fiber optic cable of 0.9 mm diameter. The light source is chosen to be a red laser of 850 nm wavelength. While the mirror was translated towards the fiber optic cable, intensity of the reflected light was measured using a photovoltaic circuitry, shown in 61. As Figure 62 presents, within a certain interval marked by the dashed lines (0.2-1.2 mm) the relation between the output voltage and mirror-to-fiber distance appears to be linear. That 1 mm wide interval determined the range of operation of the proposed compliant design in order to preserve the linearity between the input force and output voltage.

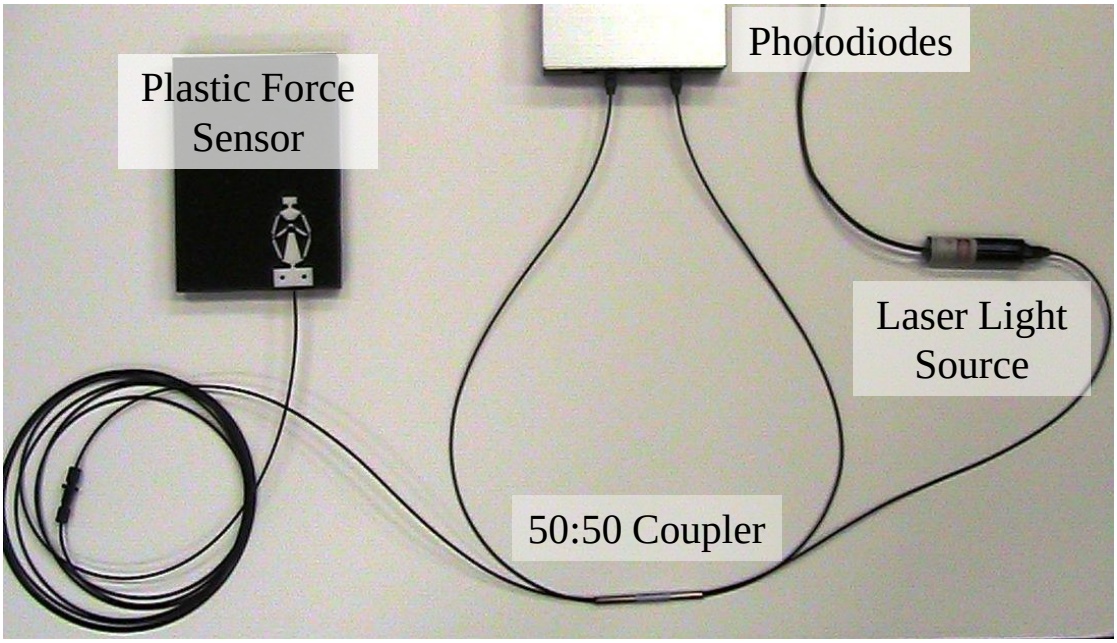


Figure 61: Fiber optic circuitry for the developed force sensor. The intensity of the light at output port with respect to the reference port is measured.

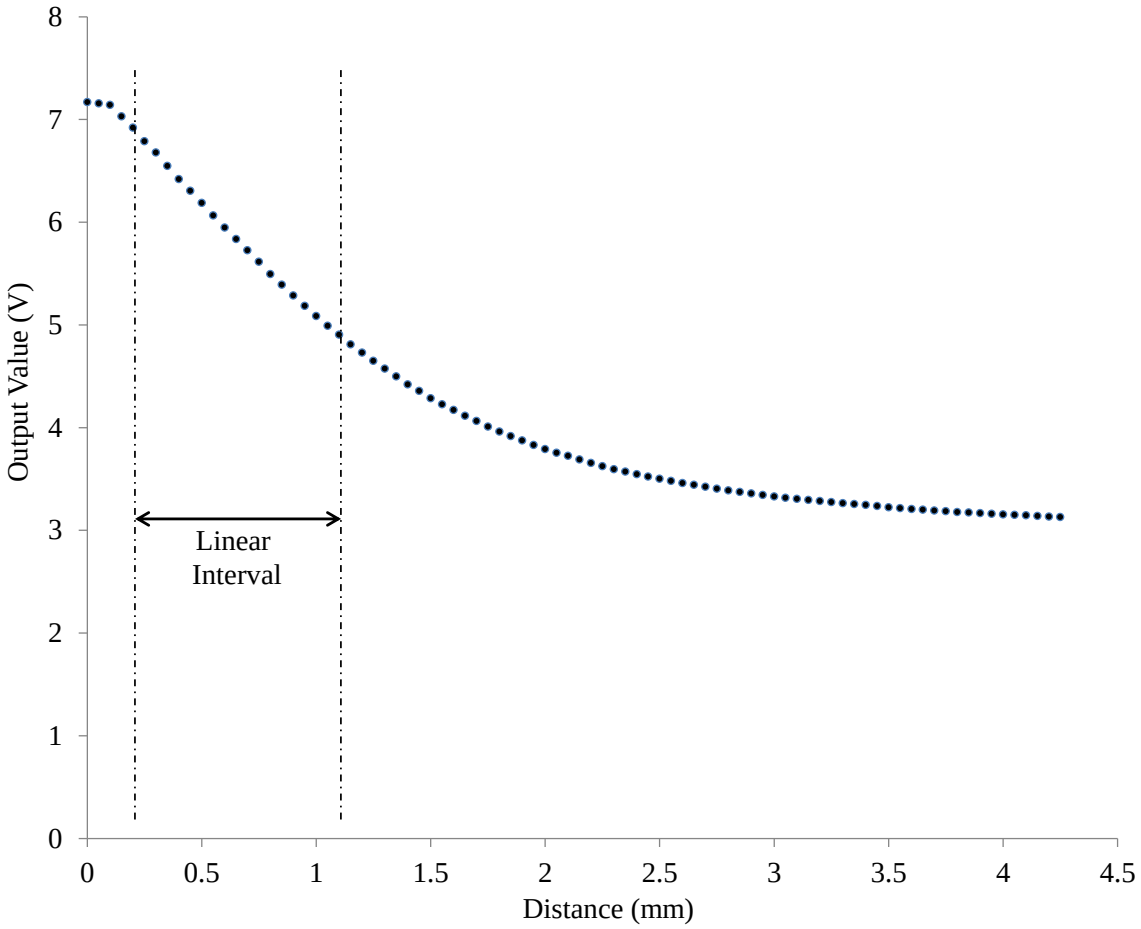


Figure 62: Light intensity vs. the distance between the mirror and the fiber tip. The intensity of light rays was measured in voltage through a photovoltaic circuitry. The output changes in a linear fashion for a 1 mm of displacement interval.

# APPENDIX E

# MECHANICAL PROPERTIES OF DELRIN

### E.0.3 Details on Manufactured Samples

The thickness values of the hinges on the manufactured samples are given in Table 7. These values are estimations based on rough measurements on the thickness of the members. Since the V-shaped cut profiles on the hinges are not exactly known, these values are prone to result in errors. The hinges are represented by the numbers assigned in Figure 48.

Another issue for the accuracy of the method described here is the assumed elastic modulus. 2.3 GPa was assumed using the first loading test performed on the basis mechanism and that value was applied to the model of the proposed design as well. To verify that assumption a tensile strength test on the material of the samples, delrin, is performed. Figure 63 shows the entire stress-strain curve of the tensile strength test and the portion of that curve which matches to the 2.3 GPa constant elastic modulus line.

The stress distribution over the beam members of the basis and proposed mechanisms has been realized utilizing the relevant methods given in Hibbeler's book and disregarding the stress concentration [26]. The stress concentration on the samples depends on the cut profile of the hinges as well as the surface quality of the cut; therefore there is not enough information for an accurate estimate on the concentration effects. A maximum stress of 40 MPa was calculated on the tested samples which is on the order of what is needed for a valid elastic modulus estimation of 2.3 GPa, considering a moderate concentration factor for the hinges which are classified as flat beams with opposing notches [52].

Table 7: Thickness Values of the Hinges on the Samples

| Hinge Number | Basis Mechanism (mm) | Sample A (Modarate Amplification Mechanism) (mm) | Sample B (High Amplification Mechanism) (mm) |
|---|---|---|---|
| 1 | 0.58 | 0.50 | 0.52 |
| 2 | 0.54 | 0.48 | 0.55 |
| 3 | 0.54 | 0.48 | 0.55 |
| 4 | 0.54 | 0.52 | 0.53 |
| 5 | 0.53 | 0.52 | 0.52 |
| 6 | 0.53 | 0.51 | 0.51 |
| 7 | 0.50 | 0.51 | 0.51 |
| 8 | 0.58 | 0.50 | 0.50 |
| 9 | - | 0.25 | 0.26 |
| 10 | - | 0.30 | 0.30 |
| 11 | - | 0.30 | 0.31 |
| 12 | - | 0.25 | 0.26 |

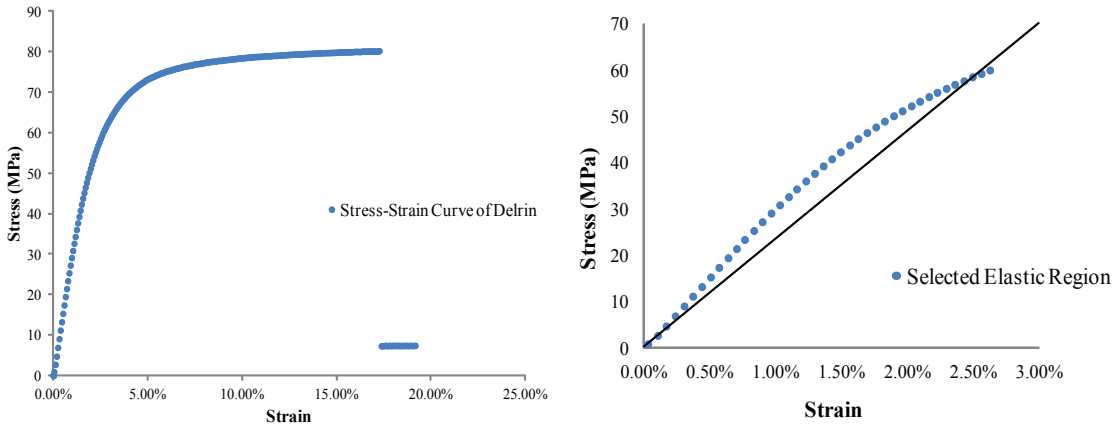


(a) (b)

Figure 63: Stress vs. strain data of delrin with with 2.3 GPa constant elastic modulus line. The elastic region of the stress vs. strain data is zoomed.

# REFERENCES


[1] Al-Ibrahim, A. M., *Transient air temperature and pressure measurements during the charging and discharging processes of an actuating pneumatic cylinder*. University of Wisconsin–Madison, 1991.

[2] Beater, P., *Pneumatic drives*. Springer, 2007.

[3] Bigras, P. and Khayati, K., "Nonlinear observer for pneumatic system with non-negligible connection port restriction," in *American Control Conference, 2002. Proceedings of the 2002*, vol. 4, pp. 3191–3195, IEEE, 2002.

[4] Bueche, F., "Mullins effect and rubber-filler interaction," *Journal of Applied Polymer Science*, vol. 5, pp. 271–281, 1961.

[5] Chapuis, D., Gassert, R., Sache, L., Burdet, E., and Bleuler, H., "Design of a simple mri/fmri compatible force/torque sensor," in *Proc. IEEE/RSJ Int. Conf. Intelligent Robots and Systems (IROS 2004)*, vol. 3, pp. 2593–2599, 2004.

[6] Chin, R., Hsiao-Wecksler, E. T., Loth, E., Kogler, G., Manwaring, S. D., Tyson, S. N., Shorter, K. A., and Gilmer, J. N., "A pneumatic power harvesting ankle-foot orthosis to prevent foot-drop," *Journal of neuroengineering and rehabilitation*, vol. 6, no. 1, p. 19, 2009.

[7] Chinzei, K., Kikinis, R., and Jolesz, F. A., "Mr compatibility of mechatronic devices: design criteria," in *Medical Image Computing and Computer-Assisted Intervention–MICCAI99*, pp. 1020–1030, Springer, 1999.

[8] Comber, D. B., Barth, E. J., and Webster, R. J., "Design and Control of an Magnetic Resonance Compatible Precision Pneumatic Active Cannula Robot," *Journal of Medical Devices*, vol. 8, p. 011003, Dec. 2013.

[9] Cramer, S. C., Nelles, G., Benson, R. R., Kaplan, J. D., Parker, R. A., Kwong, K. K., Kennedy, D. N., Finklestein, S. P., and Rosen, B. R., "A functional mri study of subjects recovered from hemiparetic stroke," *Stroke*, vol. 28, no. 12, pp. 2518–2527, 1997.

[10] Deepak, S. R., Dinesh, M., K, D., Sahu, and Ananthasuresh, G. K., "A comparative study of the formulations and benchmark problems for the topology optimization of compliant mechanisms," *Journal of Mechanisms and Robotics*, vol. 1, 2009.

[11] Dobkin, B. H., "Editorial commentfunctional mri: A potential physiologic indicator for stroke rehabilitation interventions," *Stroke*, vol. 34, no. 5, pp. e26–e28, 2003.

[12] Driver, T. and Shen, X., "Pressure Estimation-Based Robust Force Control of Pneumatic Actuators," *International Journal of Fluid Power*, vol. 14, pp. 37–45, Jan. 2013.

[13] Elmadbouly, E. and Abdulsadek Nour, M., "Modelling, simulation and sensitivity analysis of a straight pneumatic pipeline," *Energy conversion and management*, vol. 35, no. 1, pp. 61–77, 1994.

[14] Elmasry, A. and Liermann, M., "Passive pneumatic teleoperation system," in *ASME/BATH 2013 Symposium on Fluid Power and Motion Control*, pp. V001T01A040–V001T01A040, American Society of Mechanical Engineers, 2013.

[15] Fischer, G. S., Iordachita, I., Csoma, C., Tokuda, J., DiMaio, S. P., Tempany, C. M., Hata, N., and Fichtinger, G., "Mri-compatible pneumatic robot for transperineal prostate needle placement," vol. 13, no. 3, pp. 295–305, 2008.

[16] Fleischer, H. and Fleisher, J., *Manual of pneumatic systems optimization*. McGraw-Hill New York, NY, 1995.

[17] Funk, J. and Robe, T., "Transients in pneumatic transmission lines subjected to large pressure changes," *International Journal of Mechanical Sciences*, vol. 12, no. 3, pp. 245–257, 1970.

[18] Gassert, R., Chapuis, D., Bleuler, H., and Burdet, E., "Sensors for applications in magnetic resonance environments," vol. 13, no. 3, pp. 335–344, 2008.

[19] Gassert, R., Burdet, E., and Chinzei, K., "Opportunities and challenges in mr-compatible robotics," *Engineering in Medicine and Biology Magazine, IEEE*, vol. 27, no. 3, pp. 15–22, 2008.

[20] Gassert, R., Moser, R., Burdet, E., and Bleuler, H., "Mri/fmri-compatible robotic system with force feedback for interaction with human motion," *Mechatronics, IEEE/ASME Transactions on*, vol. 11, no. 2, pp. 216–224, 2006.

[21] Goodson, R. and Leonard, R., "A survey of modeling techniques for fluid line transients," *Journal of Basic Engineering*, vol. 94, no. 2, pp. 474–482, 1972.

[22] Gorce, J.-N., Hellgeth, J. W., and Ward, T. C., "Mechanical hysteresis of a polyether polyurethane thermoplastic elastomer," *Polymer Engineering & Science*, vol. 33, no. 18, pp. 1170–1176, 1993.

[23] Gulati, N. and Barth, E., "Non-linear pressure observer design for pneumatic actuators," *Proceedings, 2005 IEEE/ASME International Conference on Advanced Intelligent Mechatronics.*, vol. c, pp. 783–788, 2005.

[24] Gulati, N. and Barth, E., "A Globally Stable, Load-Independent Pressure Observer for the Servo Control of Pneumatic Actuators," *IEEE/ASME Transactions on Mechatronics*, vol. 14, pp. 295–306, June 2009.

[25] Guo, Y., Wei, L., Yu-qiao, W., Xue-feng, Y., and Ling, Y., "Kinematics analysis of bridge-type micro-displacement mechanism based on flexure hinge," in *Information and Automation (ICIA), 2010 IEEE International Conference on*, pp. 66 –70, june 2010.

[26] Hibbeler, R., "Bending," *Mechanics of materials*, pp. 254–361, 2008.

[27] Howell, L. L., *Compliant Mechanisms*. Wiley-Interscience, 2001.

[28] ISO6358:1989, "Pneumatic fluid power - components using compressible fluids - determination of flow-rate characteristics," 1989.

[29] Jolesz, F. A., Morrison, P. R., Koran, S. J., Kelley, R. J. ., Hushek, S. G., Newman, R. W., Fried, M. P., Melzer, A., Seibel, R. M. M., and Jalahej, H., "Compatible instrumentation for intraoperative mri: Expanding resource," *Journal of Medical Imaging*, vol. 8, pp. 8–11, February 1998.

[30] Jun Hyung Kim, S. H. K. and Kwak, Y. K., "Development of a piezoelectric actuator using a three-dimensional bridge-type hinge mechanism," *Review of Scientific Instruments*, vol. 74, pp. 2918–2924, May 2003.

[31] Kawahira, K., Noma, T., Iiyama, J., Etoh, S., Ogata, A., and Shimodozono, M., "Improvements in limb kinetic apraxia by repetition of a newly designed facilitation exercise in a patient with corticobasal degeneration," *International Journal of Rehabilitation Research*, vol. 32, pp. 178–83, 2009.

[32] Kawahira, K., Shimodozono, M., Etoh, S., Kamada, K., Noma, T., and Tanaka, N., "Effects of intensive repetition of a new facilitation technique on motor functional recovery of the hemiplegic upper limb and hand," *Brain Injury*, vol. 24, pp. 1202–13, 2010.

[33] Kawahira, K., Shimodozono, M., Ogata, A., and Tanaka, N., "Addition of intensive repetition of facilitation exercise to multidisciplinary rehabilitation promotes motor functional recovery of the hemiplegic lower limb," *Journal of Rehabilitation Medicine*, vol. 36, pp. 159–64, 2004.

[34] Kawakami, Y., Akao, J., Kawai, S., and Machiyama, T., "Some considerations on the dynamic characteristics of pneumatic cylinders," *The Journal of fluid control*, vol. 19, no. 2, pp. 22–36, 1988.

[35] Kawashima, K., Ishii, Y., Funaki, T., and Kagawa, T., "Determination of flow rate characteristics of pneumatic solenoid valves using an isothermal chamber," *Journal of fluids engineering*, vol. 126, no. 2, pp. 273–279, 2004.

[36] Khanicheh, A., Muto, A., Triantafyllou, C., Weinberg, B., Astrakas, L., Tzika, A., and Mavroidis, C., "Mr compatible erf driven hand rehabilitation device," in *Proc. 9th Int. Conf. Rehabilitation Robotics ICORR 2005*, pp. 7–12, 2005.

[37] Krebs, H., Dipietro, L., Levy-Tzedek, S., Fasoli, S. E., Rykman-Berland, A., Zipse, J., Fawcett, J., Stein, J., Poizner, H., Lo, A. C., and others, "A paradigm shift for rehabilitation robotics," *Engineering in Medicine and Biology Magazine, IEEE*, vol. 27, no. 4, pp. 61–70, 2008.

[38] Krichel, S. V. and Sawodny, O., "Non-linear friction modelling and simulation of long pneumatic transmission lines," *Mathematical and Computer Modelling of Dynamical Systems*, vol. 20, pp. 23–44, Jan. 2014.

[39] Krishnan, G. and Ananthasuresh, G. K., "Evaluation and design of displacement-amplifying compliant mechanisms for sensor applications," *Journal of Mechanical Design*, vol. 130, no. 10, p. 102304, 2008.

[40] Lacey, L., A, M., D., B., J., V., and J., U., "Design of mri-compatible hemiparesis rehabilitation device," *Journal of Medical Devices*, vol. 8, no. 2, 2014.

[41] Lazeroms, M., Villavicencio, G., Jongkind, W., and Honderd, G., "Optical fibre force sensor for minimal-invasive-surgery grasping instruments," in *Proc. 18th Annual Int. Conf. of the IEEE Bridging Disciplines for Biomedicine Engineering in Medicine and Biology Society*, vol. 1, pp. 234–235, 1996.

[42] Li, J., Kawashima, K., Fujita, T., and Kagawa, T., "Control design of a pneumatic cylinder with distributed model of pipelines," *Precision Engineering*, vol. 37, pp. 880–887, Oct. 2013.

[43] Lobontiu, N. and Garcia, E., "Analytical model of displacement amplification and stiffness optimization for a class of flexure-based compliant mechanisms," *Computers & Structures*, vol. 81, no. 32, pp. 2797 – 2810, 2003.

[44] Lobontiu, N., Paine, J. S. N., Garcia, E., and Goldfarb, M., "Corner-filleted flexure hinges," *Journal of Mechanical Design*, vol. 123, no. 3, pp. 346–352, 2001.

[45] Matthew B. Parkinson, Brian D. Jensen, K. K., "Design of compliant force and displacement amplification micro-mechanisms," in *ASME 2001 Design Engineering Technical Conferences*, 2001.

[46] Munson, B. R., Young, D. F., and Okiishi, T. H., *Fundamentals of fluid mechanics*. New York, 1990.

[47] Németh, H., *Nonlinear modelling and control for a mechatronic protection valve*. PhD thesis, Ph. D. thesis, Budapest University of Technology and Economics, 2004.

[48] Pandian, S. R., Takemura, F., Hayakawa, Y., and Kawamura, S., "Pressure observer-controller design for pneumatic cylinder actuators," *Mechatronics, IEEE/ASME Transactions on*, vol. 7, no. 4, pp. 490–499, 2002.

[49] Pedersen, C. B. W., Buhl, T., and Sigmund, O., "Topology synthesis of large-displacement compliant mechanisms," *International Journal for Numerical Methods in Engineering*, vol. 50, no. 12, pp. 2683–2705, 2001.

[50] Pedersen, C. B. W. and Seshia, A. A., "On the optimization of compliant force amplifier mechanisms for surface micromachined resonant accelerometers," *Journal of Micromechanics and Microengineering*, vol. 14, no. 10, pp. 1281–1293, 2004.

[51] Pegman, G., Luk, B., Liu, K., Collie, A., Cooke, D., and Chen, S., "Tele-operated climbing and mobile service robots for remote inspection and maintenance in nuclear industry," *Industrial Robot: An International Journal*, vol. 33, no. 3, pp. 194–204, 2006.

[52] Pilkey, Walter D.; Pilkey, D. F., *Peterson's Stress Concentration Factors*. John Wiley & Sons, third ed., 2008.

[53] Pratt, G. and Williamson, M., "Series elastic actuators," in *Intelligent Robots and Systems 95. 'Human Robot Interaction and Cooperative Robots', Proceedings. 1995 IEEE/RSJ International Conference on*, vol. 1, pp. 399–406 vol.1, Aug 1995.

[54] Puangmali, P., Dasgupta, P., Seneviratne, L. D., and Althoefer, K., "Miniaturized triaxial optical fiber force sensor for mri-guided minimally invasive surgery," in *Proc. IEEE Int Robotics and Automation (ICRA) Conf*, pp. 2592–2597, 2010.

[55] Richer, E. and Hurmuzlu, Y., "A high performance pneumatic force actuator system: part iinonlinear controller design," *Journal of dynamic systems, measurement, and control*, vol. 122, no. 3, pp. 426–434, 2000.

[56] Richer, E. and Hurmuzlu, Y., "A high performance pneumatic force actuator system: Part inonlinear mathematical model," *Journal of dynamic systems, measurement, and control*, vol. 122, no. 3, pp. 416–425, 2000.

[57] Sanville, F., "A new method of specifying the flow capacity of pneumatic fluid power valves," *Hydraulic Pneumatic Power*, vol. 17, no. 195, pp. 120–126, 1971.

[58] Saxena, A. and Ananthasuresh, G., "On an optimal property of compliant topologies," *Structural and Multidisciplinary Optimization*, vol. 19, pp. 36–49, 2000. 10.1007/s001580050084.

[59] Schenck, J. F., "The role of magnetic susceptibility in magnetic resonance imaging: Mri magnetic compatibility of the first and second kinds," *Medical physics*, vol. 23, no. 6, pp. 815–850, 1996.

[60] Schuder, C. and Binder, R., "The response of pneumatic transmission lines to step inputs," *Journal of Basic Engineering*, vol. 81, no. 12, pp. 578–584, 1959.

[61] Sergi, F., Krebs, H. I., Groissier, B., Rykman, A., Guglielmelli, E., Volpe, B. T., and Schaechter, J. D., "Predicting efficacy of robot-aided rehabilitation in chronic stroke patients using an mri-compatible robotic device," in *Engineering in Medicine and Biology Society, EMBC, 2011 Annual International Conference of the IEEE*, pp. 7470–7473, IEEE, 2011.

[62] Shen, X. and Goldfarb, M., "Simultaneous force and stiffness control of a pneumatic actuator," *Journal of dynamic systems, measurement, and control*, vol. 129, no. 4, pp. 425–434, 2007.

[63] Shorter, K., Xia, J., Hsiao-Wecksler, E., Durfee, W., and Kogler, G., "Technologies for powered ankle-foot orthotic systems: Possibilities and challenges," *Mechatronics, IEEE/ASME Transactions on*, vol. 18, pp. 337–347, Feb 2013.

[64] Sigmund, O., "On the design of compliant mechanisms using topology optimization*," *Mechanics of Structures and Machines*, vol. 25, no. 4, pp. 493–524, 1997.

[65] Skinner, C. K. and Wagner, F. D., *A study of the process of charging and discharging constant volume tanks with air*. PhD thesis, Dept. Mech. Eng. M.I.T., Cambridge, MA,, 1954.

[66] Slotine, J.-J. E., Li, W., and others, *Applied nonlinear control*, vol. 199. Prentice-Hall Englewood Cliffs, NJ, 1991.

[67] Song, B., Howell, A., and Hedrick, K., "Dynamic surface control design for a class of nonlinear systems," in *Decision and Control, 2001. Proceedings of the 40th IEEE Conference on*, vol. 3, pp. 2797–2802, IEEE, 2001.

[68] Song, S.-E., Cho, N. B., Fischer, G., Hata, N., Tempany, C., Fichtinger, G., and Iordachita, I., "Development of a pneumatic robot for mri-guided transperineal prostate biopsy and brachytherapy: New approaches," in *Proc. IEEE Int Robotics and Automation (ICRA) Conf*, pp. 2580–2585, 2010.

[69] Sorli, M., Gastaldi, L., Codina, E., and de las Heras, S., "Dynamic analysis of pneumatic actuators," *Simulation Practice and Theory*, vol. 7, no. 5, pp. 589–602, 1999.

[70] Stecki, J. S. D., "Fluid transmission lines-distributed parameter models (a review of the state of the art)," 1986.

[71] Su, H., Cole, G., and Fischer, G., "High-field mri-compatible needle placement robots for prostate interventions: Pneumatic and piezoelectric approaches," in *Advances in Robotics and Virtual Reality* (Gulrez, T. and Hassanien, A., eds.), vol. 26 of *Intelligent Systems Reference Library*, pp. 3–32, Springer Berlin Heidelberg, 2012.

[72] Tada, M. and Kanade, T., "Design of an mr-compatible three-axis force sensor," in *Proc. IEEE/RSJ Int. Conf. Intelligent Robots and Systems (IROS 2005)*, pp. 3505–3510, 2005.

[73] Tada, M., Sasaki, S., and Ogasawara, T., "Development of an optical 2-axis force sensor usable in mri environments," in *Proc. IEEE Sensors*, pp. 984–989, 2002.

[74] Taheri, B., Case, D., and Richer, E., "Force and stiffness backstepping-sliding mode controller for pneumatic cylinders," *Mechatronics, IEEE/ASME Transactions on*, vol. 19, no. 6, pp. 1799–1809, 2014.

[75] Takahashi, N., Tada, M., Ueda, J., Matsumoto, Y., and Ogasawara, T., "An optical 6-axis force sensor for brain function analysis using fmri," in *Proc. IEEE Sensors*, vol. 1, pp. 253–258, 2003.

[76] Tan, U.-X., Yang, B., Gullapalli, R., and Desai, J. P., "Design and development of a 3-axis mri-compatible force sensor," in *Proc. IEEE Int Robotics and Automation (ICRA) Conf*, pp. 2586–2591, 2010.

[77] Tan, U.-X., Yang, B., Gullapalli, R., and Desai, J. P., "Triaxial mri-compatible fiber-optic force sensor," vol. 27, no. 1, pp. 65–74, 2011.

[78] Todorov, E., Hu, C., Simpkins, A., and Movellan, J., "Identification and control of a pneumatic robot," in *Biomedical Robotics and Biomechatronics (BioRob), 2010 3rd IEEE RAS and EMBS International Conference on*, pp. 373–380, IEEE, 2010.

[79] Tsekos, N. V., Khanicheh, A., Christoforou, E., and Mavroidis, C., "Magnetic resonance-compatible robotic and mechatronics systems for image-guided interventions and rehabilitation: a review study," *Annu. Rev. Biomed. Eng.*, vol. 9, pp. 351–387, 2007.

[80] Tsz Ho Tse, Z., Elhawary, H., Zivanovic, A., Rea, M., Paley, M., Bydder, G., Davies, B. L., Young, I., and Lamperth, M. U., "A 3-dof mr-compatible device for magic angle related emphasis emphasistype="italic"¿in vivo experiments," vol. 13, no. 3, pp. 316–324, 2008.

[81] Turkseven, M. and Ueda, J., "Design of an mri compatible haptic interface," in *Intelligent Robots and Systems (IROS), 2011 IEEE/RSJ International Conference on*, pp. 2139–2144, Sept 2011.

[82] Turkseven, M. and Ueda, J., "An asymptotically stable pressure observer based on load and displacement sensing for pneumatic actuators with long transmission lines," *IEEE Transactions on Mechatronics*, 2015.

[83] Ueda, J., Comber, D. B., Slightam, J., Turkseven, M., Gervasi, V., III, R. J. W., and Barth., E. J., "Mri-compatible fluid-powered medical devices," *Dynamic Systems and Control Magazine*, vol. 1, no. 2, pp. 13–16, 2013.

[84] Wang, Z. and Hu, H., "Analysis and optimization of a compliant mechanism-based digital force/weight sensor," vol. 5, no. 6, pp. 1243–1250, 2005.

[85] Watton, J., "The dynamic performance of an electrohydraulic servovalve/motor system with transmission line effects," *Journal of dynamic systems, measurement, and control*, vol. 109, no. 1, pp. 14–18, 1987.

[86] Wongputorn, P., Hullender, D., Woods, R., and King, J., "Application of matlab functions for time domain simulation of systems with lines with fluid transients," *Journal of fluids engineering*, vol. 127, no. 1, pp. 177–182, 2005.

[87] Wu, J., Goldfarb, M., and Barth, E., "On the Observability of Pressure in a Pneumatic Servo Actuator," *Journal of Dynamic Systems, Measurement, and Control*, vol. 126, no. 4, p. 921, 2004.

[88] Xu, Q. and Li, Y., "Analytical modeling, optimization and testing of a compound bridge-type compliant displacement amplifier," *Mechanism and Machine Theory*, vol. 46, no. 2, pp. 183 – 200, 2011.

[89] Yang, B., Tan, U.-X., McMillan, A., Gullapalli, R., and Desai, J., "Design and control of a 1-dof mri-compatible pneumatically actuated robot with long transmission lines," *Mechatronics, IEEE/ASME Transactions on*, vol. 16, pp. 1040–1048, Dec 2011.

[90] Yang, B., Tan, U.-X., McMillan, A., Gullapalli, R., and Desai, J., "Design and control of a 1-dof mri-compatible pneumatically actuated robot with long transmission lines," *Mechatronics, IEEE/ASME Transactions on*, vol. 16, pp. 1040–1048, Dec 2011.

[91] Yin, L. and Ananthasuresh, G. K., "Design of distributed compliant mechanisms," *Mechanics Based Design of Structures and Machines*, vol. 31, no. 2, pp. 151–179, 2003.

[92] Yu, N., Hollnagel, C., Blickenstorfer, A., Kollias, S., and Riener, R., "fmri-compatible robotic interfaces with fluidic actuation," *Robotics: Science and Systems IV, Zurich, Switzerland, June*, pp. 25–28, 2008.

[93] Yu, N., Murr, W., Blickenstorfer, A., Kollias, S., and Riener, R., "An fmri compatible haptic interface with pneumatic actuation," in *Rehabilitation Robotics, 2007. ICORR 2007. IEEE 10th International Conference on*, pp. 714–720, IEEE, 2007.

[94] Zhu, Y. and Barth, E. J., "Impedance control of a pneumatic actuator for contact tasks," in *Robotics and Automation, 2005. ICRA 2005. Proceedings of the 2005 IEEE International Conference on*, pp. 987–992, IEEE, 2005.